TOWARD DESIGN AND INTEGRATION OF A NOVEL 6-DOF HAPTIC DEVICE

by

Zhouming Tang

B.A.Sc., University of Regina, 2007

a Thesis submitted in partial fulfillment
of the requirements for the degree of
Master of Applied Science
in the School
of
Engineering Science

SIMON FRASER UNIVERSITY
Fall 2010

APPROVAL

Name: Zhouming Tang

Degree: Master of Applied Science

Title of Thesis: Toward design and integration of a Novel 6-DOF Haptic Device

Examining Committee:

Dr. Marinko V. Sarunic, P. Eng,
Assistant Professor, School of Engineering Science
Chair

Dr. Shahram Payandeh, P. Eng,
Senior Supervisor, Professor, School of Engineering Science

Dr. Carlo Menon, P. Eng,
Supervisor, Assistant Professor, School of Engineering Science

---

Dr. Ted Kirkpatrick,
Internal Examiner, Associate Professor, School of Computing Science

Date Approved: 09/13/2010

Declaration of
Partial Copyright Licence

Abstract

Haptic user interface is an electro-mechanical device that interfaces the user via the sense of touch to the virtual or remote tele-operation environment. This thesis is aimed to develop a haptic user interface device that is able to provide assistance in medical surgery. A novel design hybrid 6-DOF manipulator arm has been utilized for such application. We proposed mathematical models of the manipulator arm. We designed and developed electronic interface and application software for the device. We conducted experimental studies to evaluate the performance of the proposed haptic user interface. Results demonstrated the performance of the kinematic mapping of the device and compared the computed haptic force feedback with the measured force/moment data located at the stylus of the device. In addition, we implemented gravity compensation and passivity controller methods to enhance the stability of the haptic rendering. Results indicated significant improvement in stability and also suggested future development.

To my Father Zhan Tang, my Mother Wanshan Zhang and my grandmother Peizhen Liu who unconditionally support me to follow my dreams and passions. To my girl friend Julaluck Kitpowsong who has been supporting me throughout the years of study in Canada.

Acknowledgments

I am grateful to my senior supervisor Dr. Shahram Payandeh for introducing me to the exciting research area of haptics. Dr. Payandeh's inspirations, guidance and patience has helped me to overcome the difficulties throughout this thesis work. This work would not be possible without his enthusiasm and knowledge of inter-disciplinary research.

Thanks to my supervisor Dr. Carlo Menon and to Dr. Ted Kirkpatrick for examining this thesis. Thanks to Dr. Marinko V. Sarunic for chairing my defense.

Thanks also to Mr. Dick Hendrik Van Der Wal who has made significant contribution on manufacturing the haptic device. In addition, Mr. Vanderwal has worked with me in partial redesign of the haptic device.

I thank all my colleagues in Experimental Robotics Lab who has been supporting me throughout this thesis work.

Contents

List of Tables

List of Figures

Chapter 1

Introduction

In this Chapter, problem statements and the motivations of this research project are presented by reviewing some existing robotic technologies relating to laparoscopic surgery. Section 1.2 describes the objectives of this research project and the outline of the thesis. Section 1.3 lists my contributions to this research project.

1.1 Problem Statements and Motivations

Minimally invasive surgery (MIS) is a modern surgical technique in which operations in the abdomen are performed through small incisions as compared to larger incisions needed in traditional surgical procedures. The procedures of MIS normally involves use of laparoscopic devices and remote-control manipulation of instruments with indirect observation of the surgical field through an endoscope or a similar device. Comparing with traditional surgery, MIS is more cost effective and offers great benefits to patients. These benefits include the reduction of trauma to the patients's body, less risk of infection, less blood loss, shorter hospitalization time and recovery period. Many medical procedures can be considered as minimally invasive, for example, subdermal implants, percutaneous surgery, laparoscopic surgery, arthroscopic surgery etc. Figure 1.1 shows surgeons performing laparoscopic surgery [1]. Despite the advantages to patient, MIS increase the skill level for surgeons. Comparing with traditional open surgery, surgeons performing MIS lose direct vision and the sense of touch and manipulation dexterity are largely reduced due to the use of long stem surgical instrument. As a result, surgeons are required to conduct considerable amount of training and experimentations prior to the actual MIS.

Figure 1.1: Minimally invasive laparosopic surgery [1]

Over the past two decades, robotic technology has played more and more important role in assistance of actual surgery as well as surgical training. In 1985, the PUMA 560 (a serial robot with six Degrees of Freedom (DOF) and all rotational joints), was used to place a needle for a brain biopsy using Computed Tomography (CT) guidance [2]. In 1988, the PROBOT, developed at Imperial College London, was used to perform prostatic surgery. The ROBODOC from Integrated Surgical Systems [3] was introduced in 1992 to mill out precise fittings in the femur for hip replacement. Further development of robotic systems was carried out by Intuitive Surgical [4] with the introduction of the da Vinci Surgical System and Computer Motion with the AESOP and the ZEUS robotic surgical system (Intuitive Surgical bought Computer Motion in 2003; ZEUS is no longer being actively marketed). The da Vinci Surgical System (Figure 1.2) consists of three components: a surgeons console, a patient-side robotic cart with 4 arms manipulated by the surgeon (one to control the camera and three to manipulate instruments), and a high-definition 3D vision system. Articulating surgical instruments are mounted on the robotic arms which are introduced into the body through cannulas. The device senses the surgeons hand movements and translates them electronically into scaled-down micro-movements to manipulate the tiny proprietary instruments. It also detects and filters out any tremors in the surgeon's hand movements, so that they are not duplicated robotically. In recent years, MAKO Surgical [5] has announced the release of its RIO Robotic Arm Interactive Orthopedic System (Figure 1.3). The device is designed to

Figure 1.2: The *daVinci*® surgical system from Intuitive Surgical Inc. [4]

Figure 1.3: The *RIO*® Robotic Arm Interactive Orthopedic System from MAKO Surgical Corp. [5]

assist surgeons during knee resurfacing operation, a minimally invasive type of surgery thought to be useful for younger, active patients with early osteoarthritis. Overall, the key features of robotic surgery include visual magnification, stabilization of vibration due to

shaky human hands, simulators with the use of specialized virtual reality training tools to improve the proficiency of surgeons. Robotic technology has also made telesurgery become possible. Surgical tasks are directly performed by a robotic system controlled by the surgeon at the remote site from the patient. Telesurgery has had strong military interest, with the intention of providing mobile medical care while keeping trained doctors safe from battle.

Surgical training simulators, one of the important robotic surgery features, is able to provide practises for novice surgeons or experienced surgeon who are not familiar with MIS to increase their skill level before performing the actual MIS. Surgical training simulator is comprised of virtual reality simulation environment displayed on computer screen and a haptic user interface. The patient's organs can be replicated through the data from CT and Magnetic Resonance Imaging (MRI). The virtual reality simulation environment provides the simulation of the patient's organs through advanced computer graphics technology. Figure 1.4.a shows the virtual surgical training environment developed by Chinese University of Hong Kong [6] while Figure 1.4.b shows the course of surgical training using the surgical training environment via a haptic user interface. The haptic user interface is an electro-

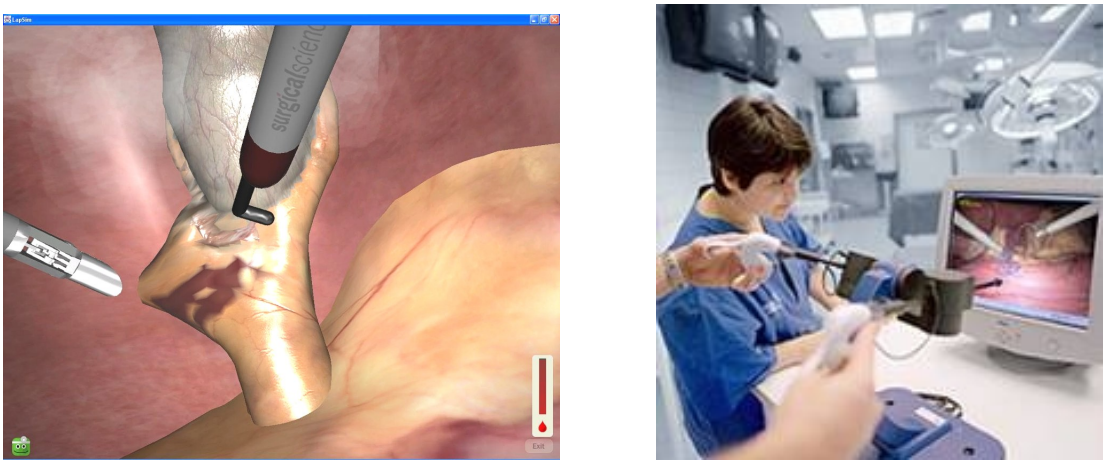

(a) (b)

Figure 1.4: Surgical training simulator, (a): virtual reality surgical training environment developed by Chinese University of Hong Kong; (b): surgical training in the virtual reality surgical training environment via a haptic user interface [6]

mechanical device that interfaces the user via the sense of touch while interacting in virtual reality simulation environment. The user can perform surgery tasks on the virtual tissues

and organs by manipulating the stylus of the haptic device, which is also displayed in the virtual reality simulation environment. Meanwhile, the haptic user interface provides realistic force-feedback to simulate the sense of actual surgery. Any imperfect or incorrect performance during the actual surgery can significantly affect the patient's hospitalization time and recovery period or even endanger the patient. Surgical training simulators can effectively prevent such undesired scenario by exposing the trainee to the potentially critical procedure in a safe and structured environment.

Over the past years, haptic device has drawn great interests from industrial companies as well as research institutes. Various haptic devices have been designed in the industry as well as research institutions. The PHANTOM Premium 1.5/6-DOF (Figure 1.5.a) and 3.0/6-DOF devices from SensAble Technologies Inc [7] and the Freedom 6S device (Figure 1.5.b) from MPB Technologies Inc. [8] are designed based on serial robot configuration, which allow users to explore application areas that require force feedback in 6-DOF and relatively large workspace. Virtuose 6D Desktop [9], which is designed and manufactured by Haption, is based on parallel type manipulator as shown in Figure 1.6.a. This includes three articulated branches whose end is fixed on the sphere of seizure. It also provides 6 degrees of kinematic freedom and returns forces and moment vectors along the end-point frame. The Omega.6 and Delta.6 devices (Figure 1.6.b) from Force Dimension [10] are designed based on combination of two 3-DOF parallel robot configuration. These devices are particularly suitable for applications that require high stiffness and accuracy. In addition to the commercial devices, other types of haptic devices have been investigated at various research institutions. S.S. Lee and J.M. Lee [11] present a general-purpose 6-DOF haptic device featuring a parallel combination of three serial manipulators and a 6-DOF force/torque (F/T) sensor in a holding bar. The performance of the device is evaluated by examining the force feedback at the handle giving step input and sinusoidal input. In addition, a force reflection resulting from a trajectory of motion command by the operator is presented to demonstrate that the device is able to serve as motion generator in the field of tele-operation. G. Carbone and M. Ceccarelli [12] propose a serial-parallel robot manipulator for medical applications. It is composed of a commercially available 3-DOF serial robot (SCARA robot Adept Cobra) and a prototype of 3-DOF parallel manipulator named "CaPaMan 2bi". The serial mechanism is responsible for positioning since it possesses larger workspace while the parallel mechanism is responsible for performing the actual surgery that requires high accuracy and stiff configuration. Researchers from Experimental Robotics Laboratory at

(a)

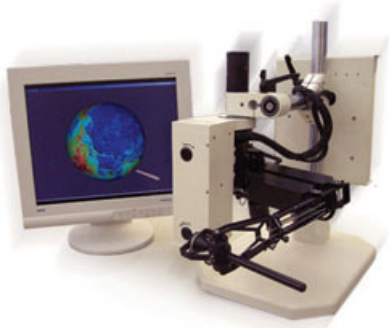

(b)

Figure 1.5: Haptic devices, (a): *PHANTOM*® Premium 1.5/6DOF haptic device from SensAble Technologies Inc. [7]; (b): Freedom 6S haptic device from MPB Technologies Inc. [8]

(a)

(b)

Figure 1.6: Haptic devices, (a): Virtuose 6D haptic device from Haption [9]; (b): Delta.6 haptic device from Force Dimension [10]

Simon Fraser University have devoted significant effort in designing and developing various types of haptic user interfaces. Figure 1.7.a and Figure 1.7.b exhibit two prototypes of haptic devices created by Li and Payandeh [13] - [15] at the Experimental Robotics Laboratory, Simon Fraser University. Hsu [16] studied the application of the laparoscopic tools-holding robot (Figure 1.7.a) with automatic tracking, tool gesture and motion recognition. Ma [17] designed and developed electronic interface and software framework for the spherical parallel

ball support type haptic device (Figure 1.7.b) to be used as surgical training simulator.

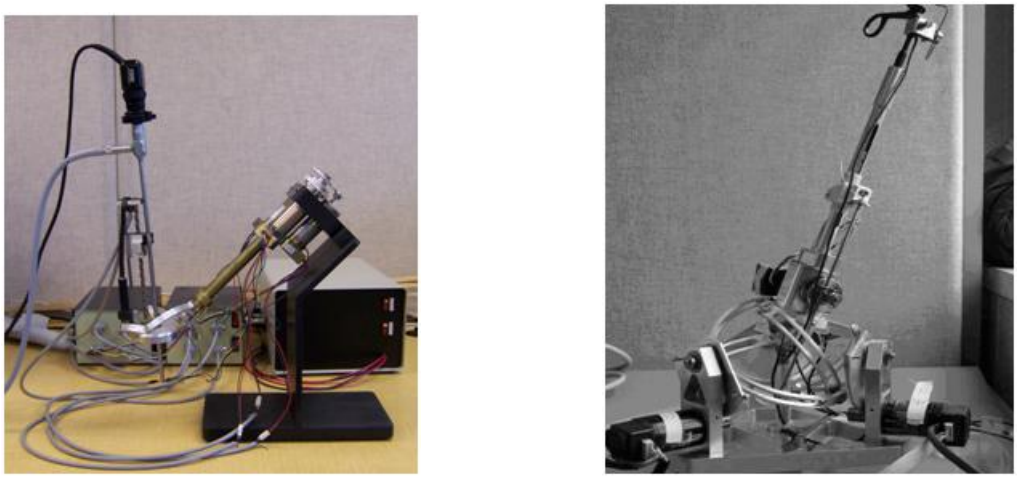

(a) (c)

Figure 1.7: Haptic devices, (a): laparoscopic tools-holding robot [16]; (b): spherical parallel ball support type haptic device [17]

In addition to the field of medical surgery, haptic user interfaces have played important role in advancing Computer Aided Design (CAD). Computer Aided Design (CAD) is a useful tool for facilitating various design processes. In CAD system, the properties (e.g. geometry, material) of mechanisms and the relationships between parts can be specified. The movements of mechanisms can be simulated and analyzed in CAD system. The results can be exported to a form that manufacturers can use to build the mechanism. For some applications where the designs need to be used by a human operator, it is important to determine if the design is suitable for human interaction. Since traditional CAD systems do not provide this feature, physical prototypes have to be built for such an evaluation. With the haptic user interface incorporated in CAD system, the designer can interact with the mechanism through a haptic device, and is able to feel the interaction forces between the virtual mechanism and the expected application environment. Haptic force feedback gives the designer an idea of the way the mechanism interacts with the intended environment in a much more direct and intuitive manner. [18] and [19] present an investigation of the effectiveness of haptic feedback for designing a class of interconnected multi-body systems such as passive mechanisms. A four-bar mechanism was used in the investigation. The results of the user study suggest that the usage of a haptic device in the design of this class

of mechanism can expedite the design process.

1.2 Objectives and Outline

Figure 1.8 exhibits the prototype of the proposed haptic device (US Patent NO: US 11/792,244) used in this thesis project. This device consists of a spherical parallel mechanism and a serial mechanism. Specifically, the spherical parallel structure consists of three symmetrical chains which connect the base with the mobile platform. Each chain is composed of three rotational joints. The spherical parallel design provides 3 rotational DOF to the very top pivot of this table top unit, which means the linkage that is connected to pivot moves with fixed distance with respect to the common stationary center point. The serial configuration consists of two serial connected linkages which connect the mobile platform with the end-effector. The serial configuration endues two additional DOF to this model. Furthermore, the 6th DOF is applied at the end-effecter so that the surgeon can have an additional rotational DOF at the incision point of the patient. The hybrid spherical parallel and serial structure design is aim to conjugate the advantages of parallel mechanism and serial mechanism which is to have large workspace, high stiffness and accuracy.

One of the main objectives of this research project is to integrate the proposed haptic device towards a surgical simulator. In order to achieve this goal, we firstly develop mathematical models of the haptic device including kinematics, Jacobians and static force. These mathematical models are the building blocks of the haptic interface because they establish analytical relationships of the following information: actuator joint angles and, the position and orientation of the stylus of the haptic device; the actuator joint velocities and the velocity of the stylus in Cartesian space; the actuator joint torques and the force/torque exerted at the stylus. Then, we develop an electronic interface which includes the following major functions: determine the starting configuration of haptic device; read six individual joint angles; supply accurate analog voltage to joint actuators based on the joint torques values; interpret the force and torque data from the F/T sensor. The electronic interface is created by using off-the-shelf commercial electronic products: PCI I/O cards, brushed DC motors each of which is attached with an optical encoder, servo amplifiers, power supplies, F/T sensor and the F/T sensor controller. Application software is another important component of the haptic interface. It is responsible for executing the following major tasks in real time: determine the position and orientation of the stylus; display and update the graphical haptic

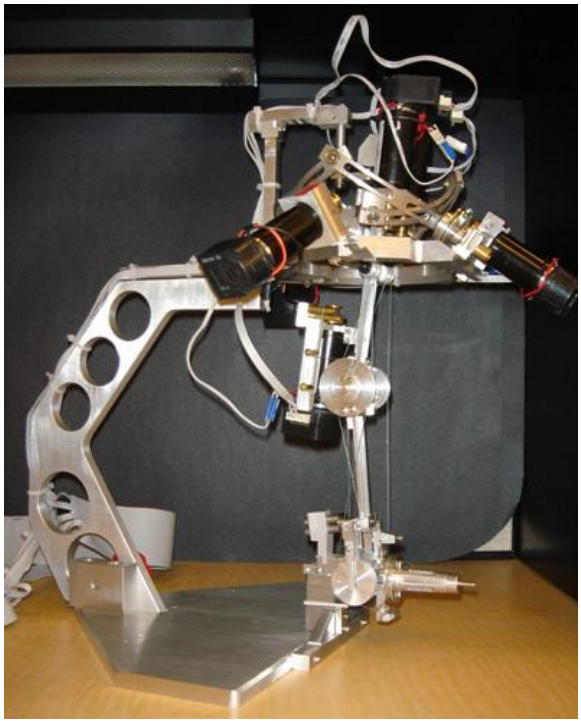

Figure 1.8: The prototype of the 6-DOF haptic device

device configuration, the position and orientation of the stylus in the virtual environment and the graphic user interface; determine the desired force and torque at the stylus based on the collision detection algorithm and mechanics-base interaction; calculate the actuator joint torques; collect the actual force and torque data from the F/T sensor.

Evaluation and enhancement of the proposed haptic interface is another main objectives of this thesis work. Kinematic and force correspondence experiments are designed and performed to evaluate the kinematic and force correspondence characteristics of the haptic user interface. The characteristics of 6 axes force and torque display are investigated through interaction with various virtual environments through the haptic interface. Feed-forward gravity compensation and passivity control methods are developed and implemented to enhance the performance of the haptic interface. Feed-forward gravity compensation method is aim to largely eliminate the gravity effect of the haptic device. Passivity control methods is aim to increase the stability of the haptic interface during the course of haptic interaction.

The main objective of this thesis work is achieved by developing the following specific

topics:

- Develop forward and inverse kinematic models for the proposed haptic device
- Develop Jacobian model for velocity and static force analysis of the haptic device
- Develop static force model for the haptic device
- Design and develop the electronic interface for the haptic device
- Develop application software for experimental studies
- Conduct kinematic and force correspondence experiments to verify the kinematic and force correspondence characteristics of the proposed haptic interface
- Perform experimental studies on the interaction with virtual environments to exam the force and torque display of the proposed haptic interface
- Research and develop the gravity compensation method and passivity control method to enhance the performance of the proposed haptic interface

This thesis documentation is divided into five chapters. The motivations and objectives are discussed in Chapter 1. Chapter 2 begins with an overview of the design of the proposed haptic device, followed by a thorough description of the forward and inverse kinematic models. Jacobian models and static force model of the haptic device are then presented. Chapter 3 starts with description of the electronic interface and application software of the proposed haptic interface, followed by the presentation of the calibration of the starting position of the haptic device and the study of actuator characteristic. Kinematic and force correspondence experiments are then presented. After that, experiments of interaction with virtual environments using the proposed haptic user interface are demonstrated. Chapter 4 presents the development of feed-forward gravity compensation method and passivity control method to enhance the performance of the proposed haptic user interface. Experiments of interaction with virtual environment using the proposed methods are then demonstrated. Chapter 5 concludes the research presented in this thesis.

1.3 Contributions

The major contributions of this thesis work are summarized below:

- **Analysis of the hybrid spherical parallel/serial 6-DOF haptic device and derivation of a close-form solution:** Mathematical models of forward and inverse kinematics, Jacobian and static force of the novel hybrid structure manipulator are established.

- **Development of electronic interface and application softwares of the haptic user interface:** the proposed electronic interface and application software is designed to integrate the haptic device towards a surgical simulator. They can be implemented on other types of 6-DOF haptic device for such application

- **Evaluation and enhancement of the performance of the proposed haptic interface:** Various experiments are designed and performed to evaluate kinematic and force correspondence characteristics and the 6 axes force and torque display characteristics of the proposed haptic interface. The verifications are performed by comparing the computed force and torque with the actual force and torque value collected from the F/T sensor. The feed-forward gravity compensation and passivity control methods are developed and implemented to enhance the performance of the haptic user interface.

Chapter 2

Analysis of the 6-DOF Haptic Device

2.1 Introduction

Haptic user interface is an electro-mechanical device that interfaces the user via the sense of touch to the virtual or remote tele-operation environment. This is accomplished through the haptic rendering by computing forces, vibrations and/or motions to the user. The haptic technology has been implemented in various applications such as scientific exploration, virtual prototyping, surgical training simulator and tele-operation. Specifically, in the application of surgical training simulator, it is expected to provide more realistic sensation of the measured or computed contact force between tissue and instrument.

The mechanical model of haptic devices, or manipulators in general case, can be classified in three types: serial, parallel and hybrid. A serial manipulator is a mechanism composed of an end-effector connected to a base link by means of a single serial chain, while a parallel manipulator is a mechanism composed of a moving platform connected to a fixed platform by at least two kinematic chains. A hybrid manipulator is a combination of parallel and serial manipulators, or it is an arrangement of two or more parallel manipulators connected in tandem. It also combines the main advantages of serial and parallel manipulators. They have large workspace, high stiffness, great load capacity and good accuracy [20], which is suitable for the surgical training simulator application.

Hybrid manipulators have drawn great attention for the past decade. Tanio [21] presented a hybrid (parallel-serial) robot manipulator which is composed of two serially connected parallel mechanisms where each mechanism has 3DOFs. Four closed-form solutions for both forward and inverse kinematics of this manipulator are presented. Geometrical properties are utilized to obtain forward kinematic solutions, while algebraic approach is implemented to obtain inverse kinematic solutions. A hybrid manipulator proposed by L. Romdhane [22] is composed of serial connection of parallel platforms. Eight closed-form solutions are obtained through the forward kinematic analysis. X.Z. Zheng et al. [23] proposed quaternion base forward kinematic solutions of two sequentially connected 3-UPU (U represents universal joint and P represents prismatic joint) parallel mechanisms. The first 3-UPU mechanism constitutes with middle platform and fixed base, while the second rotational 3-UPU mechanism is made up of middle platform and end platform. By applying unit quaternion transformation, 8 closed-form solutions are obtained. G. Yang et al. [24] introduces the design and analysis of a new modular hybrid parallel-serial manipulator. The proposed hybrid parallel-serial manipulator consists of a 3-DOF planar parallel platform and a 3-DOF serial robotic arm. The forward kinematic analysis of the planar parallel mechanism is carried out by utilizing the geometric properties while the product-of-exponentials formulation approach is adopted to perform the forward kinematic analysis of the serial mechanism which resulted in four real solutions. Based on their proposed modeling approach, the inverse kinematic analysis is accomplished based on algebraic method. M. Ceccarelli [25] presents a hybrid manipulator which consists of a spatial parallel manipulator with 3-DOF and a telescopic serial manipulator with 2-DOF. Three Euler parameters are introduced to perform the kinematic analysis of the spatial parallel manipulator, while an angle between the telescopic arm and the mobile platform and a distance variable at the prismatic joint are introduced to characterize the kinematic model of the telescopic serial manipulator.

In order to meet the requirements of the surgical training simulator application as well as the mechanical design of haptic device such as low friction effect and inertia of moving parts, high stiffness and precision and large workspace, a 6-DOF hybrid spherical parallel/serial haptic device has been designed. This chapter presents the mathematical models and analysis of the haptic device. Section 2.2 presents an overview of the design of the haptic device. Section 2.3 and Section 2.4 discuss the forward and inverse kinematic models. This derivation provides a closed-form solution that can be used for defining the starting position

of the device during the course of haptic interaction experimentations as well as tracking the position and orientation of the physical stylus in the virtual environment. Section 2.5 presents numerical examples for the forward and inverse kinematic models. The Jacobians related to static force analysis and velocity calculation are discussed in Section 2.6. Section 2.7 presents the static force model. The mathematical models established in this chapter contribute to the basis for developing the haptic user interface.

2.2 Kinematic Configuration of the Hybrid Parallel/Serial Manipulator

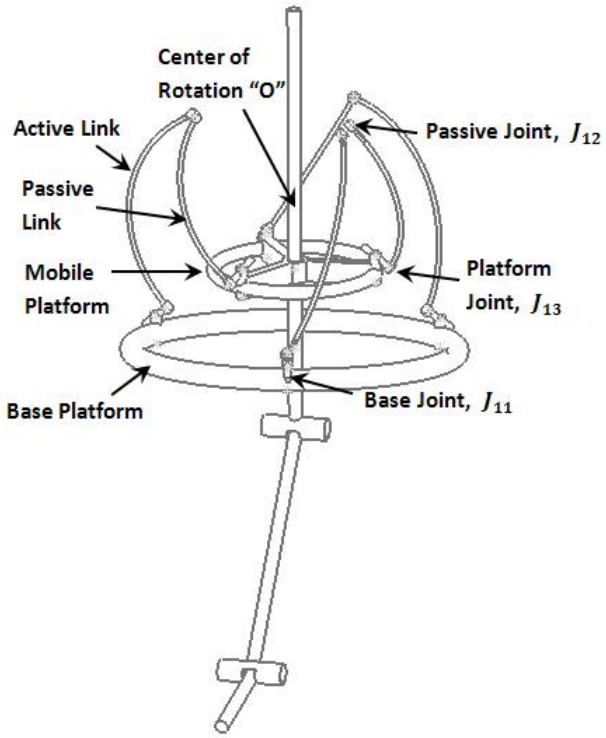

Figure 2.1: Kinematic model of the hybrid parallel/serial manipulator

The design of the haptic device is based on combination of the spherical parallel mechanism configuration and serial configuration (Figure 2.1 and Figure 2.2), which inherits the characteristic of hybrid manipulator. The spherical parallel mechanism is composed by three

identical kinematic chains each of which has 3 revolute joints. As shown in Figure 2.1, J_{11}-J_{13} represent 3 revolute joints of the first kinematic chain respectively. The spherical parallel platform also combines both active and passive components at the center of rotation. The active part controls the orientation of the mobile platform while the passive part supports the static weight of the robot and the resultant user interaction force on the mobile platform (the passive joint reduces the forces and moments on the moving joints of the mechanism). The passive spherical joint at the center of rotation can be designed to have any geometry as long as its configuration does not interfere with the active workspace of the platform. Specifically, the parallel spherical design provides 3 rotational DOF about the center of the sphere. As a result, the center of platform can move along the geodesic paths on a sphere having a fixed redial distance about the pivot point, which is also known as the center of rotation "O".

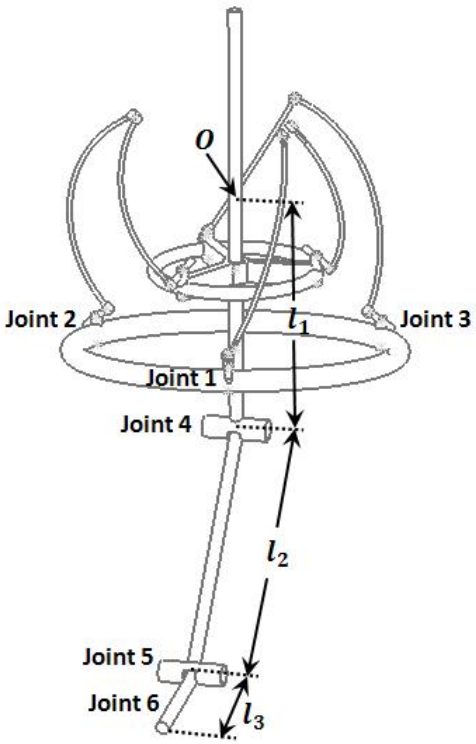

Figure 2.2: Joint and link configuration of hybrid parallel/serial manipulator

A rigid link namely l_1 as shown in Figure 2.2 is connected to the platform which is a base

of the serial manipulator. Another link l_2 is connected to l_1 through a revolute joint. The two intersecting joint axes at the end of l_2 can be the wrist of the manipulator. The overall structure of this class of robot can resemble a human arm where the three spherical rotation of the robot can be considered as the shoulder joint of the manipulator and the first joint of the serial link can be the elbow, the two intersection joint axes at the end of the serial like can be the wrist of the manipulator. The serial configuration contributes 3-DOF to the 6-DOF hybrid manipulator.

Figure 2.3 depicts the approximation of the reachable workspace of the haptic device. Table 2.1 illustrates the dimensions of the reachable workspace of the haptic device. We can observe from the table that the height of the reachable workspace ranges from 201 mm to 318 mm; the width and the depth of the reachable workspace ranges from 261 mm to 449 mm. Table 2.2 illustrates the dimensions of the workspace of four commercial haptic devices which are mentioned in Chapter 1.1. Comparing the workspace of the four commercial haptic devices, we can claim that the proposed haptic device has relatively large workspace.

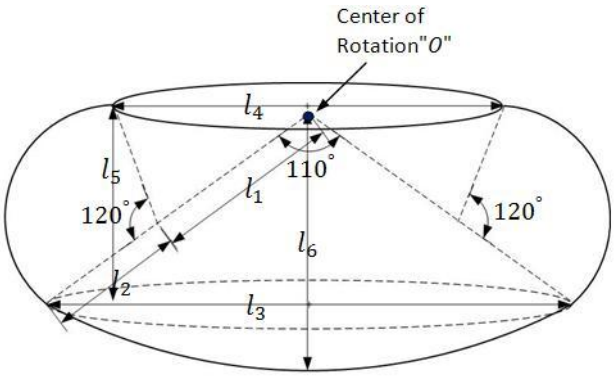

Figure 2.3: Approximation of the reachable workspace

Table 2.1: The reachable workspace dimensions of the proposed haptic device

l_1 (mm)	l_2 (mm)	l_3 (mm)	l_4 (mm)	l_5 (mm)	l_6 (mm)
146	128	449	261	201	318

Overall, the combination of the parallel spherical and serial configuration has following advantages: 1) location for the actuators (away from the moving platform); 2) larger

Table 2.2: The reachable workspace dimensions of commerical haptic devices

	Height (mm)	Width (mm)	Depth (mm)
PHANTOM Premium 1.5/6-DOF Device	267	381	191
Freedom 6S Device	170	220	330
Virtuose 6D Desktop Device	120	120	120
Delta.6 Device	400	400	400

workspace for the end-effector through the connecting link to the platform.

2.3 Forward Kinematic Modeling

In this section, we first review the forward kinematic solution for the spherical parallel configuration. After that, the forward kinematic analysis of the serial configuration and the entire hybrid configuration are introduced.

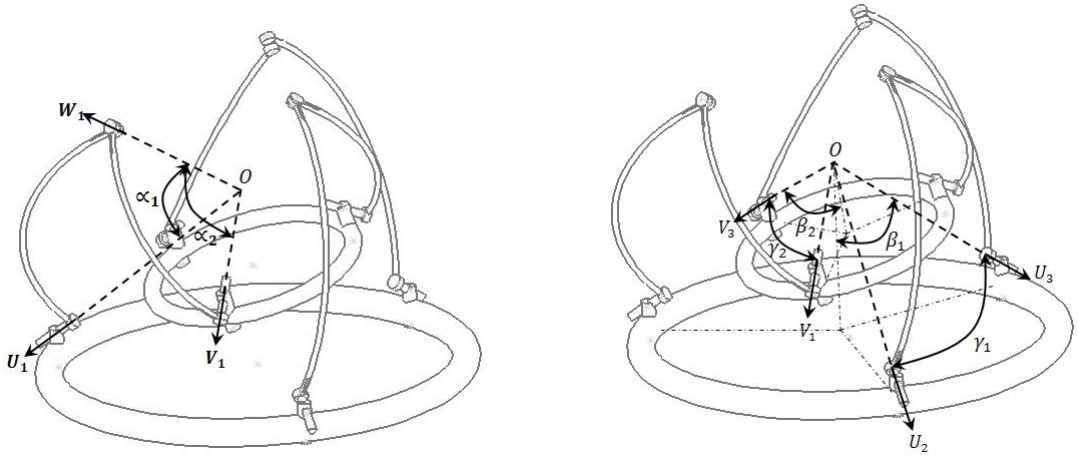

(a) (b)

Figure 2.4: Geometric parameters of spherical parallel mechanism: (a): α_1(angle between W_i and U_i axes),α_2(angle between W_i and V_i axes) (b): β_1 (angle between U_i and the normal axis of the base plane),β_2 (angle between V_i and the normal axis of the mobile platform plane),γ_1 (angle between the adjacent U_i axis), γ_2 (angle between the adjacent V_i axis)

The kinematic analysis of spherical 3-DOF parallel manipulators has been studied extensively in [26]. The first revolute joint of each kinematic chain is attached to the base having

U_i $(i = 1, 2, 3)$ as its axis. The third revolute joint of each kinematic chain is connected to the moving platform and is defined by V_i. The second revolute joint is defined by W_i. Referring to Figure 2.4.a, U_1 is the axis of rotation of J_{11}; V_1 is the axis of rotation of J_{13}; W_1 is the axis of rotation of J_{12}. The axes are orthogonal to each other at a single point "O" as shown in Figure 2.4, the center of rotation of the parallel spherical mechanism, where we have $U_i \cdot W_i = \cos(\alpha_1)$ and $W_i \cdot V_i = \cos(\alpha_2)$. Since α_1 and α_2 are 90°, one can write the following kinematic constraint equation:

$$W_i \cdot V_i = 0 \tag{2.1}$$

As depicted in Figure 2.4.b, γ_1 is the angle between the adjacent U_i $i = 1, 2, 3$, for example U_2 and U_3. γ_2 is the angle between the adjacent V_i $i = 1, 2, 3$, for example V_1 and V_3. From the kinematic definition we have: $U_1 \perp U_2 \perp U_3$ and $V_1 \perp V_2 \perp V_3$, hence $\gamma_1 = \gamma_2 = 90°$. Let β_1 be the angle between U_i and the normal axis of the base plane and β_2 be the angle between V_i and the normal axis of the mobile platform plane. Craver in [27] has introduced a canonical equation which establishes the relationship between these angles as:

$$\sin(\beta_i) = \frac{2\sqrt{3}}{3} \sin(\frac{\gamma_i}{2}) \tag{2.2}$$

We have selected $\beta_1 = \beta_2 = 55°$ in our design. In our kinematic model, a fixed world coordinate frame (WCF) is assigned with respect to U_i axes. Meanwhile, a mobile platform coordinate frame (PCF) is assigned with respect to V_i axes. Figure 2.5 depicts the frame assignment, where x_w, y_w and z_w are the X, Y and Z axes of the WCF respectively; x_p, y_p and z_p are the X, Y and Z axes of the PCF respectively.

Figure 2.5 also depicts the device at its reference or home configuration where we define zero joint variables. At the reference configuration, z_w and z_p coincide and make 180° angle with the axis of joint J_{22}, namely W_2, which is the passive joint axis of the second kinematic chain. With these settings, the axes of WCF are defined by the following unit vectors expressed in accordance with the reference configuration:

$$x_w = U_2 = [1, 0, 0]^T;\ y_w = U_3 = [0, 1, 0]^T;\ z_w = U_1 = [0, 0, 1]^T;$$

Similarly, as shown in Figure 2.5, the set of axes V_i^* represent the PCF at reference configuration with respect to the WCF:

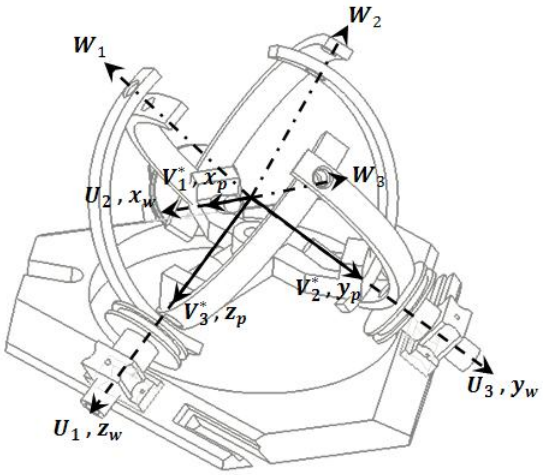

Figure 2.5: The configuration of reference frame $\{V_i^*\}$ $(i = 1, 2, 3)$

$$x_p^* = V_1^* = [1, 0, 0]^T;\ y_p^* = V_2^* = [0, 1, 0]^T;\ z_p^* = V_3^* = [0, 0, 1]^T;$$

The set of unit vectors V_i which represent PCF are functions of the orientation of the mobile platform [28]. Let this orientation be described by the Z-Y-X Euler rotation matrix R, then

$$V_i = \mathbf{R}V_i^* \tag{2.3}$$

$$\begin{aligned} \mathbf{R} &= \mathbf{R}_z(\phi_1)\mathbf{R}_y(\phi_2)\mathbf{R}_x(\phi_3) \\ &= \begin{bmatrix} c\phi_1 c\phi_2 & c\phi_1 s\phi_2 s\phi_3 - s\phi_1 c\phi_3 & c\phi_1 s\phi_2 c\phi_3 + s\phi_1 s\phi_3 \\ s\phi_1 c\phi_2 & s\phi_1 s\phi_2 s\phi_3 + c\phi_1 c\phi_3 & s\phi_1 s\phi_2 c\phi_3 - c\phi_1 s\phi_3 \\ -s\phi_2 & c\phi_2 s\phi_3 & c\phi_2 c\phi_3 \end{bmatrix} \end{aligned} \tag{2.4}$$

The set of V_i axes can be represented by the column vectors of $\mathbf{R}$ matrix as defined in equation (2.3):

$$V_1 = \begin{bmatrix} c\phi_1 c\phi_2 \\ s\phi_1 c\phi_2 \\ -s\phi_2 \end{bmatrix},\ V_2 = \begin{bmatrix} c\phi_1 s\phi_2 s\phi_3 - s\phi_1 c\phi_3 \\ s\phi_1 s\phi_2 s\phi_3 + c\phi_1 c\phi_3 \\ c\phi_2 s\phi_3 \end{bmatrix},\ V_3 = \begin{bmatrix} c\phi_1 s\phi_2 c\phi_3 + s\phi_1 s\phi_3 \\ s\phi_1 s\phi_2 c\phi_3 - c\phi_1 s\phi_3 \\ c\phi_2 c\phi_3 \end{bmatrix} \tag{2.5}$$

Where, $s\phi$ stands for $\sin\phi$ while $c\phi$ stands for $\cos\phi$. For the sake of consistency, the set of W_i axes are defined based on the reference configuration. In order to visualize how the set of W_i axes are defined based on WCF, a conceptual diagram for the case of W_1 axis is depicted in Figure 2.6. At reference configuration, W_1 axis makes 180° with y_w axis and 90° with x_w axis. When rotation takes place about z_w axis by θ_1, W_1 axis will rotate accordingly. $W_1^{'}$ axis denotes the W_1 axis after the rotation as shown in Figure 2.6.

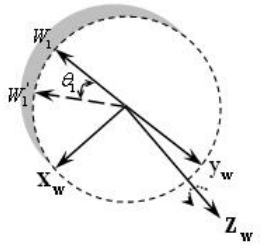

Figure 2.6: Conceptual diagram for the case of W_1 axis

If a column vector is utilized to represent W_1 axis, the first entry will be the projection of $W_1^{'}$ axis to x_w while the second entry will be the projection of $W_1^{'}$ axis to y_w axis. Since z_w is perpendicular with the plane of x_w W_1 y_w, the third entry will be zero. Similarly, W_2 and W_3 axes can be defined. Equation (2.6) presents the analytical expression of these three passive joint axes.

$$W_1 = \begin{bmatrix} s\theta_1, & -c\theta_1, & 0 \end{bmatrix}^T,\ W_2 = \begin{bmatrix} 0, & s\theta_2, & -c\theta_2 \end{bmatrix}^T,\ W_3 = \begin{bmatrix} -c\theta_3, & 0, & s\theta_3 \end{bmatrix}^T \quad (2.6)$$

Where, θ_1, θ_2 and θ_3 are the three actuator joint angles. When the PCF is at its reference orientation, these joint angles are 0°.

Substituting equation (2.5) and (2.6) into equation (2.1) with three actuator joint variables θ_1, θ_2 and θ_3 will lead to three equations with three unknowns, ϕ_1, ϕ_2 and ϕ_3, which are used in the definition of $\mathbf{R}$ to result in the eight possible orientations of PCF with respect to WCF. Among these eight solutions, four solutions are nontrivial which are denoted as $\mathbf{R}_1 - \mathbf{R}_4$ while the rest of four solutions are trivial (where all three kinematic chains can freely rotate) which are denoted as $\mathbf{R}_{TO1} - \mathbf{R}_{TO4}$. It has been shown that the first solution, $\mathbf{R}_1$, of the four nontrivial solutions is the only correct solution among the total of eight possible solutions giving the definition of constraints on workspace and singularities.

This solution agrees with the formulation, proposed by X. Kong and C. Gosselin [29], which represents a unique current forward kinematic solution of this class of parallel spherical manipulator.

The solution of the orientation of the mobile platform is utilized to determine the forward kinematics of the serial part of the robot. As depicted in Figure 2.7, the platform is connected with the first serial actuator joint (joint 4) by link l_1. The frame 4 is defined such that Z_4 axis is pointing along the rotational axis of joint 4 and X_4 axis is pointing towards joint 5 along the link l_2. Therefore, the orientation and position of the frame of reference for joint 4 is able to be determined by the transformation relationship between PCF to frame 4. To facilitate the remaining of the forward kinematic solution, an intermediate PCF $\{p^{'}\}$ is introduced which coincides with frame $\{p\}$. Referring to Figure 2.7, $Z_{p'}$ axis is chosen to be pointing towards the opposite direction of Z_4 axis while $X_{p'}$ axis is chosen so that it not only aligns with X_4 axis when θ_4 is equal to 0° but also makes 180° with X_4. $Y_{p'}$ axis is therefore perpendicular to the $Z_{p'}$ $X_{p'}$ plane. Section 2.5.2 presents the numerical example of the mapping from PCF $\{p\}$ to the intermediate PCF $\{p^{'}\}$.

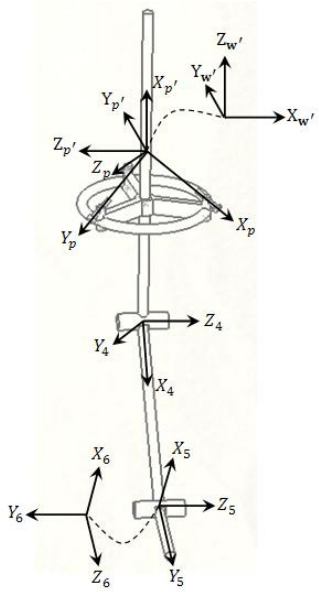

Figure 2.7: The serial mechanism configuration of the hybrid device

For the development of transformation between frame $\{p^{'}\}$ and frame 4 and also between frame 4 and frame 6, we have utilized the D-H notations and link coordinate frame assignment [30]. The transformation of the first serial joint (joint 4) with respect to the WCF can be formulated as follow,

$$ {}^{W}_{4}T = T_1 \, {}^{p}_{p'}T \, {}^{p'}_{4}T \tag{2.7} $$

where, T_1 is the homogeneous transformation from WCF to PCF corresponding to the first orientation solution $\mathbf{R}_1$. Since PCF coincides with WCF at "O", the position vector of T_1 is $[0, 0, 0]^T$. Hence, the eight possible forward orientation solutions of the spherical parallel mechanism $(\mathbf{R}_1, \ldots, \mathbf{R}_8)$ will result in eight possible ${}^{W}_{4}T$. These eight sets of results will lead to eight sets of forward kinematic solution each of which represent one possible orientation and position of the end-effector with respect to WCF. The following equation describes the forward kinematic solution based on T_1.

$$ {}^{W}_{6}T = T_1 \, {}^{p}_{p'}T \, {}^{p'}_{4}T \, {}^{4}_{5}T \, {}^{5}_{6}T \tag{2.8} $$

Due to the unique frame assignment of WCF, the numerical result of ${}^{W}_{6}T$ may cause confusions during the course of graphic simulation of the device. Therefore, we introduce a hypothetical world coordinate frame $\{W^{'}\}$ which coincides with PCF as shown in Figure 2.7, where $Z_{W'}$ is pointing in an upwards direction while $Y_{W'}$ is pointing towards the opposite direction of the initial Z_4. The mapping from the original WCF to the hypothetical WCF can be represented as ${}^{W}_{W'}T$ (see numerical example in section 2.5.2). Equation (2.9), which accommodates the mapping, is an analytical expression of the orientation and position of the end-effector with respect to the hypothetical WCF $\{W^{'}\}$.

$$ {}^{W^{'}}_{6}T = [{}^{W}_{W'}T]^{-1} \, T_1 \, {}^{p}_{p'}T \, {}^{p'}_{4}T \, {}^{4}_{5}T \, {}^{5}_{6}T \tag{2.9} $$

2.4 Inverse Kinematic Modeling

In this section we present an approach for solving inverse kinematic problem for the proposed class of hybrid manipulator. Our proposed approach in this paper consists of establishing three sets of dependent solutions. We first present a solution for the position and orientation of joint 4 reference frame with respect to WCF. Then we present a solution methodolgy for

the first three joints (θ_1,θ_2 and θ_3) given the solution for joint 4. Lastly, we solve for the two wrist joints (θ_5 and θ_6) giving ${}^{W}_{4}T$ and ${}^{W}_{6}T$.

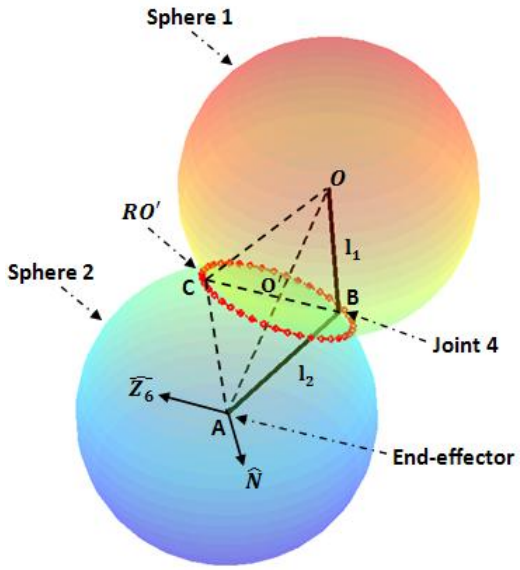

Figure 2.8: Conceptual visualization of the haptic device I

Figure 2.8 is a conceptual visualization of our solution approach for the fourth joint of the robot. In the figure, sphere 1 is centered at the center of rotation "O" of the spherical parallel mechanism and sphere 2 is centered at the origin of the end-effector or the spherical wrist "A". The radius of these two spheres is the length of the first and second links (l_1 and l_2) of the serial section of the mechanism as shown in Figure 2.8. The intersection circle between the two spheres $RO^{'}$ is centered at "$O^{'}$". The plane OBAC, which intersects with the circle $RO^{'}$ at point "B" and "C", is formed by centers of frames for joints 4, 5 and the center of rotation "O". The unit vector $\widehat{N}$ is the normal of this plane. Therefore, for a particular orientation of the plane OBAC, point "B" and "C" can be two possible positions for the origin of joint 4. However, due to the physical limits of joint 4, the link configuration which is associated with the position "C" can be unattainable. From the geometry of the figure we note also that $\vec{OO'}$ is perpendicular to the plane of circle $RO^{'}$. A rotation of mobile platform will cause plane OBAC rotate about the axis "AO" and as a result, the origin for the frame of joint 4 (e.g. point "B") will travel along the circumference of the circle $RO^{'}$.

$$\angle OBA = cos^{-1}(\frac{|OB|^2 + |BA|^2 - |OA|^2}{2|OB||BA|}) \tag{2.10}$$

$$\theta_4 = -(180^\circ - \angle OBA) \tag{2.11}$$

Given $|OA|$,$|OB|$ and $|AB|$, $\angle OBA$ can be obtained from equation (2.10) and θ_4 can be expressed from equation (2.11).

$${}^{W'}P_{x_4}^2 + {}^{W'}P_{y_4}^2 + {}^{W'}P_{z_4}^2 = l_1^2 \tag{2.12}$$

$$({}^{W'}P_{x_4} - {}^{W'}P_{x_6})^2 + \ ({}^{W'}P_{y_4} - {}^{W'}P_{y_6})^2 + \ ({}^{W'}P_{z_4} - {}^{W'}P_{z_6})^2 = l_2^2 \tag{2.13}$$

$$\widehat{N} = \frac{\vec{AO}}{|AO|} \times \widehat{Z}_6 \tag{2.14}$$

$$\widehat{N} \cdot \frac{\vec{OB}}{|OB|} = 0 \tag{2.15}$$

where,

$\vec{OB} = [{}^{W'}P_{x_4}, {}^{W'}P_{y_4}, {}^{W'}P_{z_4}]^T \ \vec{AO} = [- {}^{W'}P_{x_6}, - {}^{W'}P_{y_6}, - {}^{W'}P_{z_6}]^T$

Equation (2.14) defines the normal vector $\widehat{N}$ of the plane OBAC as the cross product between the unit vector of $\hat{AO}$ and $\widehat{Z}_6$ (the z direction of end-effector frame). Equation (2.12) and (2.13) define the sphere 1 and 2 respectively in terms of the position of joint 4, $([{}^{W'}P_{x_4}, {}^{W'}P_{y_4}, {}^{W'}P_{z_4}]^T)$. Combining these two equations ensures that the position of joint 4 is located on the intersection circle RO'. In addition, equation (2.15) adds a constraint on the orientation of plane OBAC knowing $\widehat{N}$ from equation (2.14). Therefore, the two possible positions of joint 4 ("B" and "C") can be determined by solving equation (2.12)-(2.15).

Refer to Figure 2.9, frame $\{A\}$ is assigned to coincide with the origin of the end-effector "A". In particular, the z axis of frame $\{A\}$, Z_A, aligns with $\hat{N}$ and the x axis of frame $\{A\}$, X_A, is pointing towards "O". Giving the position and orientation of the end-effector with respect to $\{W'\}$, the orientation matrix of frame $\{A\}$ can be defined as:

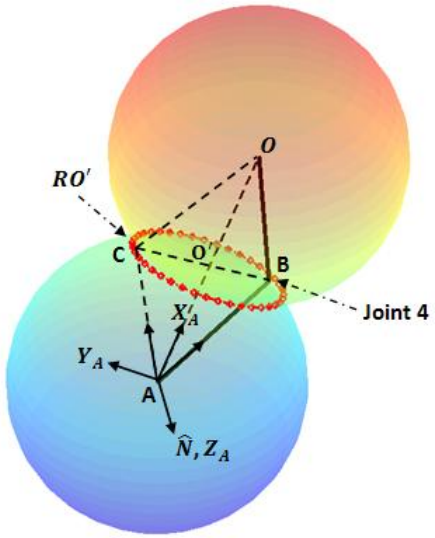

Figure 2.9: Conceptual visualization of the haptic device II

$$\begin{aligned} \widehat{Z}_A = &\quad \widehat{N} \\ \widehat{X}_A = &\quad [\tfrac{-^{W'}P_{x_6}}{|AO|}, \tfrac{-^{W'}P_{y_6}}{|AO|}, \tfrac{-^{W'}P_{z_6}}{|AO|}]^T \\ \widehat{Y}_A = &\quad \widehat{Z}_A \times \widehat{X}_A \end{aligned} \tag{2.16}$$

The position of point "B" and "C" uniquely define the unit vector $\hat{AB}$ and $\hat{AC}$ respectively as depicted in Figure 2.9. In addition, based on the geometric property, the projection of $\hat{AB}$ along the y axis of frame $\{A\}$ (Y_A) results in negative value while the projection of $\hat{AC}$ to Y_A results in positive value. This characteristics holds for all possible configurations of the device. Hence, based on the numerical values of these two projections, one is able to determine which one of the two possible solutions of the position of joint 4 corresponds to "B" or the valid position.

The two unit vectors pointing from point "A" to the two possible positions of joint 4 are formulated as shown in equation (2.17).

$$\begin{aligned} \hat{Sol}_1 = &\quad [\tfrac{^{W'}P_{x_{4_1}} - ^{W'}P_{x_6}}{|l_2|}, \tfrac{^{W'}P_{y_{4_1}} - ^{W'}P_{y_6}}{|l_2|}, \tfrac{^{W'}P_{z_{4_1}} - ^{W'}P_{z_6}}{|l_2|}]^T \\ \hat{Sol}_2 = &\quad [\tfrac{^{W'}P_{x_{4_2}} - ^{W'}P_{x_6}}{|l_2|}, \tfrac{^{W'}P_{y_{4_2}} - ^{W'}P_{y_6}}{|l_2|}, \tfrac{^{W'}P_{z_{4_2}} - ^{W'}P_{z_6}}{|l_2|}]^T \end{aligned} \tag{2.17}$$

Where, $\hat{Sol}_1$ represents the unit vector pointing from point "A" ($[{}^{W'}P_{x_6}, {}^{W'}P_{y_6}, {}^{W'}P_{z_6}]$) to the position of the joint 4 defined by the first solution ($[{}^{W'}P_{x_{4_1}}, {}^{W'}P_{y_{4_1}}, {}^{W'}P_{z_{4_1}}]$); ${}^{W'}P_{x_{4_i}}$ $(i = 1, 2)$ stands for the i^{th} solution of the x component of the position of joint 4 with respect to frame $\{W'\}$. Solving $\hat{Sol}_1$ and $\hat{Sol}_2$ and the projection of these two vectors to Y_A will lead to the result of validation.

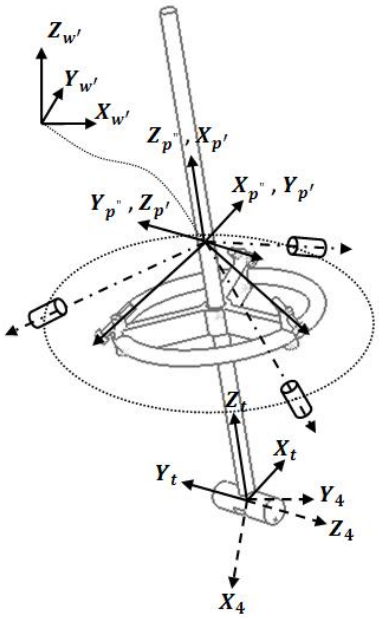

Figure 2.10: Frame assignment for solving the orientation of joint 4

In addition to the position of joint 4, the orientation of joint 4 with respect to $\{W'\}$ (${}^{W'}_{4}R$) is required in order to determine three spherical parallel joint angles. Refer to Figure 2.10, a tip frame $\{t\}$ with its z axis pointing upwards along the link l_1 and its x axis in parallel with $Y_{P'}$ is assigned to coincide with joint 4 reference frame. In addition, in order to facilitate the transformation between joint 4 reference frame and WCF, another hypothetical platform frame $\{P''\}$ having the same orientation as the tip frame is assigned at the center of rotation "O". The expression for ${}^{W'}_{t}R$ or ${}^{W'}_{P''}R$ (the orientation of $\{t\}$ frame or $\{P''\}$ frame with respect to the $\{W'\}$ frame) can be developed based on the position of joint 4, $\{{}^{W'}_{4}P\}$, and the vector $\widehat{N}$. Specifically, Z_t or $Z_{P''}$ can be determined based on the position of joint 4; Y_t or $Y_{P''}$ can be determined based on the vector $\widehat{N}$; X_t or $X_{P''}$ can be determined by taking the cross product of aforementioned two unit vectors. Equation (2.18) presents the

expression of the orientation of $\{t\}$ frame or $\{P^{''}\}$ frame with respect to the $\{W^{'}\}$ frame.

$$\begin{aligned} \widehat{Z}_{P''} = \quad \widehat{Z}_t = \quad & [\tfrac{-^{W^{'}}P_{x_4}}{|l_1|}, \tfrac{-^{W^{'}}P_{y_4}}{|l_1|}, \tfrac{-^{W^{'}}P_{z_4}}{|l_1|}]^T \\ \widehat{Y}_{P''} = \quad \widehat{Y}_t = \quad & -\widehat{N} \\ \widehat{X}_{P''} = \quad \widehat{X}_t = \quad & \widehat{Y}_{P''}(\widehat{Y}_t) \times \widehat{Z}_{P''}(\widehat{Z}_t) \end{aligned} \tag{2.18}$$

Having determined the orientation of $\{P^{''}\}$ frame with respect to $\{W^{'}\}$ frame, the orientation of joint 4 with respect to $\{W^{'}\}$ frame can be obtained by the following equation.

$${}^{W^{'}}_{4}R = {}^{W^{'}}_{P''}R \; {}^{P^{''}}_{P^{'}}R \; {}^{P^{'}}_{4}R \tag{2.19}$$

Where ${}^{P^{''}}_{P^{'}}R$ can be obtained by directly applying geometric mapping from $\{P^{''}\}$ frame to $\{P^{'}\}$ frame. Next, the matrix which is the mapping from WCF to PCF can be obtained.

$$T = {}^{W}_{W'}T \; {}^{W^{'}}_{P''}T \; {}^{P^{''}}_{P^{'}}T \; {}^{P^{'}}_{P}T \tag{2.20}$$

Equation (2.1) is utilized to obtain the solutions for $\theta_i (i = 1, 2, 3)$ [31]. The results are as follow:

$$\theta_1 = atan2(V_{1y}, V_{1x}); \theta_2 = atan2(V_{2z}, V_{2y}); \theta_3 = atan2(V_{3x}, V_{3z}) \tag{2.21}$$

Where, V_{ix} and V_{iy} are the x and y component of V_i as depicted in equation (2.5). Lastly, having ${}^{W^{'}}_{4}T$ and ${}^{W^{'}}_{6}T$, the values for θ_5 and θ_6 can be determined through equation (2.22). ${}^{4}_{6}T$ is defined as equation (2.23).

$$\theta_5 = atan2(-{}^{4}_{6}T(1,1), {}^{4}_{6}T(2,1)); \; \theta_6 = atan2(-{}^{4}_{6}T(3,1), -{}^{4}_{6}T(3,2)) \tag{2.22}$$

$${}^{4}_{6}T = [{}^{W^{'}}_{4}T]^{-1} \; {}^{W^{'}}_{6}T \tag{2.23}$$

Where, ${}^{4}_{6}T(1,1)$, the entry for the first row and the first column of ${}^{4}_{6}T$, represents the projection of X_6 to X_4.

/* **Initialize parameters** */

SET $|OB|$=l_1 and $|BA|$=l_2
READ ${}^{W'}_{6}T$
GET ${}^{W'}P_6$ from ${}^{W'}_{6}T$
DETERMINE $|OA|$ from ${}^{W'}P_6$
GET $\widehat{Z}_6$ from ${}^{W'}_{6}T$
COMPUTE $\widehat{N}$ by using equation (2.14)
READ ${}^{W}_{W'}T$ from equation (2.36)
READ ${}^{P"}_{P'}T$ from equation (2.44)
READ ${}^{P}_{P'}T$ from equation (2.33)
COMPUTE ${}^{P'}_{P}T$ by finding the inverse of ${}^{P}_{P'}T$

/* **Solve** θ_4 */

COMPUTE θ_4 by using equation (2.10) and (2.11)

/* **Solve the position of joint 4** ${}^{W'}P_4$ */

DETERMINE ${}^{W'}P_{4_1}$ and ${}^{W'}P_{4_2}$ by using equation (2.12),(2.13) and (2.15)
COMPUTE $\widehat{Y}_A$ by using equation (2.16)
COMPUTE $\hat{S}ol_1$ and $\hat{S}ol_2$ by using equation (2.17)
COMPUTE $PROJ_1$ and $PROJ_2$ by using equation (2.42)
if $PROJ_1 < 0$ **then**
  ${}^{W'}P_4$=${}^{W'}P_{4_1}$
else
  ${}^{W'}P_4$=${}^{W'}P_{4_2}$
end

/* **Solve the orientation of joint 4** ${}^{W'}_{4}R$ */

COMPUTE $\hat{X_{P"}}$, $\hat{Y_{P"}}$, $\hat{Z_{P"}}$ by using equation (2.18)
DEFINE ${}^{W'}_{P"}R$ as $[\hat{X_{P"}}, \hat{Y_{P"}}, \hat{Z_{P"}}]$
EXTRACT ${}^{P"}_{P'}R$ from ${}^{P"}_{P'}T$
COMPUTE ${}^{P'}_{4}T$ by using equation (2.34)
EXTRACT ${}^{P'}_{4}R$ from ${}^{P'}_{4}T$
COMPUTE ${}^{W'}_{4}R$ by using equation (2.19)

/* **Solve the orientation of PCF w.r.t. WCF** R */

FORM ${}^{W'}_{P"}T$ based on ${}^{W'}_{P"}R$
COMPUTE T by using equation (2.20)
EXTRACT R from T

/*Solve θ_1,θ_2 **and** θ_3*/

EXTRACT V_{1_x},V_{1_y},V_{2_y},V_{2_z},V_{3_x} and V_{3_z} from R
COMPUTE θ_1, θ_2 and θ_3 by using equation (2.21)

/* **Solve** θ_5 **and** θ_6 */

COMPUTE ${}^{W}_{4}T$ by using equation (2.7)
COMPUTE ${}^{W'}_{W}T$ by taking the inverse of ${}^{W}_{W'}T$
COMPUTE ${}^{W'}_{4}T$ by multiplying ${}^{W'}_{W}T$ with ${}^{W}_{4}T$
COMPUTE ${}^{4}_{6}T$ by using equation (2.23)
COMPUTE θ_5 and θ_6 by using equation (2.22)

Algorithm 1: Inverse Kinematic Solution

2.5 Case Studies of the Kinematic Models

This section presents numerical examples of the forward kinematic model, inverse kinematic model, force model and velocity calculations. The detail numerical example for forward kinematic solutions of the hybrid 6DOF haptic device will be discussed. A set of forward kinematic solution will then be utilized as an example to walk through the inverse kinematic model.

Before the numerical solutions, we firstly present detail dimensions of the device as shown in Figure 2.11 and Table 2.3. In addition, based on the mechanical constraints and joint frame assignments, we also specify the limit of all six actuated joints as shown in Table 2.4.

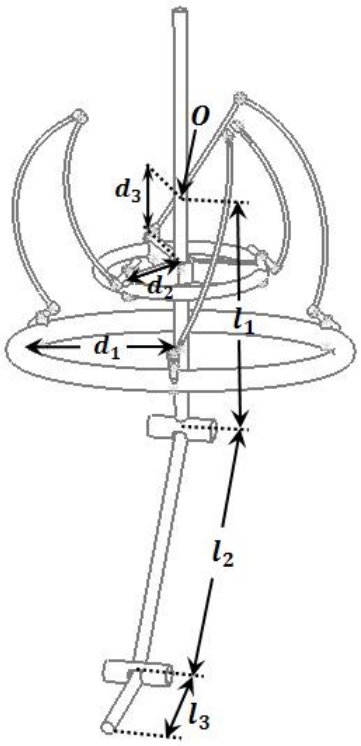

Figure 2.11: Simplified CAD model with dimensions

Table 2.3: The summary of device dimensions

d_1	d_2	d_3	l_1	l_2
55 mm	40 mm	28 mm	146 mm	128 mm

Table 2.4: The summary of the limit of six actuated joints

θ_1	θ_2	θ_3	θ_4	θ_5	θ_6
$(0°, 90°)$	$(0°, 90°)$	$(0°, 90°)$	$(-120°, 0°)$	$(-160°, 0°)$	$(0°, 360°)$

2.5.1 Forward Kinematic Solutions of the Spherical Parallel Configuration

By substituting equation (2.5) and equation (2.6) into equation (2.1), one is able to reach three equations with three unknowns ϕ_1, ϕ_2 and ϕ_3. Solving these three unknowns will lead to the solution of the orientation and position of PCF with respect to WCF.

$$s\theta_1 c\phi_1 c\phi_2 - c\theta_1 s\phi_1 c\phi_2 = 0 \tag{2.24}$$

$$s\theta_2(s\phi_1 s\phi_2 s\phi_3 + c\phi_1 c\phi_3) - c\theta_2 c\phi_2 s\phi_3 = 0 \tag{2.25}$$

$$-c\theta_3(c\phi_1 s\phi_2 c\phi_3 + s\phi_1 s\phi_3) + s\theta_3 c\phi_2 c\phi_3 = 0 \tag{2.26}$$

From(2.24), the forward kinematic problem admits two solutions defined by equations (2.27) and (2.28).

$$sin(\theta_1 - \phi_1) = 0 \tag{2.27}$$

$$cos(\phi_2) = 0 \tag{2.28}$$

Equation (2.27) offers two solutions for the angle ϕ_1:

$$\phi_1 = \theta_1 \quad and \quad \phi_1 = \theta_1 \pm \pi \tag{2.29}$$

According to [34], the above two solutions will lead to the same orientation of the mobile platform. Hence, only the first solution will be used in this paper. Substituting $\phi_1 = \theta_1$ into equation (2.25) and (2.26) will lead to two possible solutions of ϕ_2 in $(-\pi, \pi]$.

$$\phi_2 = tan^{-1}(-C_1/C_2) + K\pi \quad (K = 0, 1) \tag{2.30}$$

Where,

$$C_1 = c\theta_3 c\theta_1 s\theta_2 s\theta_1 - s\theta_3 c\theta_2$$

$$C_2 = s\theta_3 s\theta_2 s\theta_1 + c\theta_3 c\theta_2 c\theta_1$$

Once angle ϕ_2 has been determined, equation (2.25) or equation (2.26) can be rearranged to solve for ϕ_3 in $(-\pi, \pi]$.

$$\phi_3 = tan^{-1}((s\theta_2 c\theta_1)/(c\theta_2 c\phi_2 - s\theta_2 s\theta_1 s\phi_2)) + K\pi \quad (K = 0, 1) \tag{2.31}$$

There exists two solutions of ϕ_3 in $(-\pi, \pi]$ for each solution of ϕ_2. Therefore, there are in total four possible solutions associated with equation (2.27). Table 2.5 summaries these four solutions when θ_1, θ_2 and θ_3 are $30°, 20°$ and $25°$ respectively.

Table 2.5: The numerical results of the four nontrivial solutions given that $\theta_1, \theta_2, \theta_3$ are $30°, 20°, 25°$

Euler angles (rad)	Set 1	Set 2	Set 3	Set 4
ϕ_1	0.524	0.524	0.524	0.524
ϕ_2	0.314	0.314	3.456	3.456
ϕ_3	0.339	3.480	-0.339	2.803

Each set of solutions corresponds to one possible orientation of the platform with respect to WCF $(\mathbf{R}_1, \ldots, \mathbf{R}_4)$. The corresponding transformation matrices are listed as the following:

$$T_1 = \begin{bmatrix} 0.82 & -0.38 & 0.42 & 0 \\ 0.48 & 0.87 & -0.14 & 0 \\ -0.31 & 0.32 & 0.90 & 0 \\ 0 & 0 & 0 & 1 \end{bmatrix} \quad T_2 = \begin{bmatrix} 0.82 & 0.38 & -0.42 & 0 \\ 0.48 & -0.87 & 0.14 & 0 \\ -0.31 & -0.32 & -0.90 & 0 \\ 0 & 0 & 0 & 1 \end{bmatrix}$$

$$T_3 = \begin{bmatrix} -0.82 & -0.38 & -0.42 & 0 \\ -0.48 & 0.87 & 0.14 & 0 \\ 0.31 & 0.32 & -0.90 & 0 \\ 0 & 0 & 0 & 1 \end{bmatrix} \qquad T_4 = \begin{bmatrix} -0.82 & 0.38 & 0.42 & 0 \\ -0.48 & -0.87 & -0.14 & 0 \\ 0.31 & -0.32 & 0.90 & 0 \\ 0 & 0 & 0 & 1 \end{bmatrix}$$

For the case of spherical parallel robots, these four solutions are regarded as nontrivial solution because none of the kinematic chains is singular [34]. Nevertheless, in our case, a hybrid spherical parallel/serial robot, the mobile platform is directly connected with the 3DOF serial robot, which applies a constraint on the workspace of the mobile platform. As a result, only the first set of solution is valid. Figure 2.12 describes the graphic representation of these four solutions when θ_1, θ_2 and θ_3 are $30°, 20°$ and $25°$ respectively. One is able to observe that only the first set of solution (Figure 2.12.a) is attainable because the serial link l_1 crosses the circumference of the base platform.

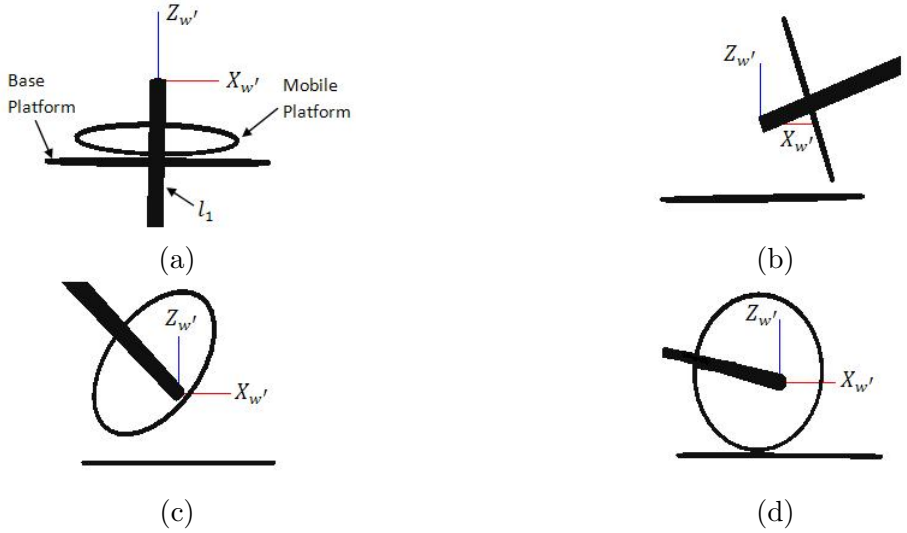

Figure 2.12: The four nontrivial solutions of the orientation of the platform with respect to the WCF for $\theta_1 = 30°$, $\theta_2 = 20°$ and $\theta_3 = 25°$: (a): $\phi_1 = 0.524$, $\phi_2 = 0.314$, $\phi_3 = 0.339$; (b): $\phi_1 = 0.524$, $\phi_2 = 0.314$, $\phi_3 = 3.480$; (c): $\phi_1 = 0.524$, $\phi_2 = 3.456$, $\phi_3 = -0.339$; (d): $\phi_1 = 0.524$, $\phi_2 = 3.456$, $\phi_3 = 2.803$

Equation (2.28) provides two solutions for the angle ϕ_2,

$$\phi_2 = \frac{\pi}{2} \quad and \quad \phi_2 = -\frac{\pi}{2} \tag{2.32}$$

Substitute these two solutions for the angle ϕ_2 into equation (2.25) and (2.26), two conditions are found for the arbitrary actuator joint angles of the spherical parallel configuration (θ_1, θ_2 *and* θ_3): $cos(\phi_1 - \phi_3) = 0$, $cos(\phi_1 + \phi_3) = 0$. The corresponding orientations of the PCF with respect to WCF can be described by four rotation matrices($\mathbf{R}_{TO1}$-$\mathbf{R}_{TO4}$) and the associated transformation matrices are listed as below:

$$T_{TO1} = \begin{bmatrix} 0 & -1 & 0 & 0 \\ 0 & 0 & 1 & 0 \\ -1 & 0 & 0 & 0 \\ 0 & 0 & 0 & 1 \end{bmatrix} \qquad T_{TO2} = \begin{bmatrix} 0 & 1 & 0 & 0 \\ 0 & 0 & -1 & 0 \\ -1 & 0 & 0 & 0 \\ 0 & 0 & 0 & 1 \end{bmatrix}$$

$$T_{TO3} = \begin{bmatrix} 0 & -1 & 0 & 0 \\ 0 & 0 & -1 & 0 \\ 1 & 0 & 0 & 0 \\ 0 & 0 & 0 & 1 \end{bmatrix} \qquad T_{TO4} = \begin{bmatrix} 0 & 1 & 0 & 0 \\ 0 & 0 & 1 & 0 \\ 1 & 0 & 0 & 0 \\ 0 & 0 & 0 & 1 \end{bmatrix}$$

When the platform is at one of these four orientations, all three kinematic chains are at singularity and can freely rotate about their actuator joint axes ($U_i \quad (i = 1, 2, 3)$). Thus, these four orientations are trivial solutions to the forward kinematic problem of the proposed class of spherical parallel configuration and exist for any set of actuator joint angles [29].

2.5.2 Forward Kinematic Solution of the Hybrid Haptic Device

As discussed in Chapter 2.3, the mobile platform serves as a link between spherical parallel mechanism and the serial mechanism. For the simplicity of mapping, an intermediate PCF $\{p^{'}\}$ is introduced and is described in Figure 2.7. The mapping form the original PCF $\{p\}$ to the intermediate PCF $\{p^{'}\}$ can be expressed as follow:

$$^{p}_{p'}T = \begin{bmatrix} X_{P'} \cdot X_P & Y_{P'} \cdot X_P & Z_{P'} \cdot X_P & 0 \\ X_{P'} \cdot Y_P & Y_{P'} \cdot Y_P & Z_{P'} \cdot Y_P & 0 \\ X_{P'} \cdot Z_P & Y_{P'} \cdot Z_P & Z_{P'} \cdot Z_P & 0 \\ 0 & 0 & 0 & 1 \end{bmatrix}$$

$$^{p}_{p'}T = \begin{bmatrix} -0.57 & -0.41 & -0.71 & 0 \\ -0.57 & -0.41 & 0.71 & 0 \\ -0.57 & 0.82 & 0 & 0 \\ 0 & 0 & 0 & 1 \end{bmatrix} \tag{2.33}$$

Equation (2.33) exhibits the numerical value of every entry of ${}^{p}_{p'}T$ which is determined based on the dimension and geometric properties of the device. Referring to Figure 2.7, the mapping from the intermediate PCF to joint 4; joint 4 to joint 5 and joint 5 to joint 6 utilizes the D-H parameters which are listed in Table 2.6.

Table 2.6: D-H parameters for serial mechanism

i	α_{i-1}	a_{i-1}	d_i	θ_i
P'	N/A	N/A	N/A	N/A
4	180°	-146 mm	0	$180° + \theta_4$
5	0°	128 mm	0	$-90° + \theta_5$
6	$-90°$	0	0	θ_6

The corresponding transformation matrices are described as follow:

$$ {}^{P'}_{4}T = \begin{bmatrix} -c_4 & s_4 & 0 & -146 \\ s_4 & c_4 & 0 & 0 \\ 0 & 0 & -1 & 0 \\ 0 & 0 & 0 & 1 \end{bmatrix} {}^{4}_{5}T = \begin{bmatrix} s_5 & c_5 & 0 & 128 \\ -c_5 & s_5 & 0 & 0 \\ 0 & 0 & 1 & 0 \\ 0 & 0 & 0 & 1 \end{bmatrix} {}^{5}_{6}T = \begin{bmatrix} c_6 & -s_6 & 0 & 0 \\ 0 & 0 & 1 & 0 \\ -s_6 & c_6 & 0 & 0 \\ 0 & 0 & 0 & 1 \end{bmatrix} \quad (2.34) $$

As discussed in section 2.3, the eight possible solutions of matrix R will lead to eight possible solutions of the orientation and position of the end-effector with respect to WCF or forward kinematic solution of the hybrid haptic device which can be formulated as equation (2.35).

$$ {}^{W}_{6}T = T_i \, {}^{p}_{p'}T \, {}^{p'}_{4}T \, {}^{4}_{5}T \, {}^{5}_{6}T \quad (i = 1, \ldots, 8) \quad (2.35) $$

The corresponding numerical results giving that (θ_1,θ_2,θ_3,θ_4,θ_5,θ_6) is ($30°, 20°, 25°, -60°, -50°, 120°$) are listed as follow:

$$ {}^{W}_{6}T_1 = \begin{bmatrix} -0.54 & 0.78 & -0.32 & 85.63 \\ 0.68 & 0.62 & 0.39 & 218.69 \\ 0.50 & -0.02 & -0.87 & 27.87 \\ 0 & 0 & 0 & 1 \end{bmatrix} \quad {}^{W}_{6}T_2 = \begin{bmatrix} 0.56 & 0.56 & -0.60 & 160.43 \\ 0.62 & 0.19 & 0.76 & 136.80 \\ 0.55 & -0.80 & -0.24 & -107.15 \\ 0 & 0 & 0 & 1 \end{bmatrix} $$

$$ {}^{W}_{6}T_3 = \begin{bmatrix} -0.67 & 0.74 & -0.07 & 69.07 \\ 0.62 & 0.61 & 0.50 & 212.23 \\ 0.41 & 0.28 & -0.86 & 78.24 \\ 0 & 0 & 0 & 1 \end{bmatrix} \quad {}^{W}_{6}T_4 = \begin{bmatrix} 0.95 & 0.23 & 0.19 & 165.88 \\ -0.13 & -0.22 & 0.97 & -29.75 \\ 0.27 & -0.94 & -0.19 & -165.93 \\ 0 & 0 & 0 & 1 \end{bmatrix} $$

$$ {}^{W}_{6}T_5 = \begin{bmatrix} 0.71 & -0.67 & -0.22 & -60.13 \\ -0.68 & -0.72 & 0 & -227.72 \\ -0.16 & 0.14 & -0.98 & -21.49 \\ 0 & 0 & 0 & 1 \end{bmatrix} \quad {}^{W}_{6}T_6 = \begin{bmatrix} 0.95 & 0.23 & 0.19 & 165.88 \\ -0.13 & -0.22 & 0.97 & -29.75 \\ 0.27 & -0.94 & -0.19 & -165.93 \\ 0 & 0 & 0 & 1 \end{bmatrix} $$

$$ {}^{W}_{6}T_7 = \begin{bmatrix} 0.65 & -0.59 & -0.49 & -60.74 \\ -0.72 & -0.68 & -0.12 & -227.14 \\ -0.27 & 0.42 & -0.87 & 25.52 \\ 0 & 0 & 0 & 1 \end{bmatrix} \quad {}^{W}_{6}T_8 = \begin{bmatrix} -0.36 & -0.21 & -0.91 & -113.72 \\ -0.78 & -0.46 & 0.41 & -172.95 \\ -0.52 & 0.86 & 0.01 & 114.41 \\ 0 & 0 & 0 & 1 \end{bmatrix} $$

Note that ${}^{W}_{6}T_1$ corresponds to the forward kinematic solution when the first solution of matrix $\mathbf{R}$ ($\mathbf{R}_1$) is taken into account. The same situation applies to the rest of the forward kinematic solutions.

For better interpretation of the forward kinematic solutions and the simplicity of inverse kinematic derivation, a hypothetical WCF is introduced as described in section 2.5.2. The numerical value of the mapping ${}^{W}_{W'}T$ is presented as follow:

$$ {}^{W}_{W'}T = \begin{bmatrix} 0.71 & 0.41 & -0.57 & 0 \\ 0 & -0.82 & -0.57 & 0 \\ -0.71 & 0.41 & -0.57 & 0 \\ 0 & 0 & 0 & 1 \end{bmatrix} \tag{2.36} $$

The corresponding eight possible sets of solutions which depict the orientation and position of the end-effector with respect to the hypothetical WCF are illustrated as follow:

$$ {}^{W'}_{6}T_1 = \begin{bmatrix} -0.73 & 0.56 & 0.38 & 40.49 \\ -0.56 & -0.19 & -0.80 & -131.14 \\ -0.38 & -0.80 & 0.46 & -192.93 \\ 0 & 0 & 0 & 1 \end{bmatrix} \quad {}^{W'}_{6}T_2 = \begin{bmatrix} 0.01 & 0.96 & -0.25 & 187.73 \\ -0.05 & -0.25 & -0.96 & -89.16 \\ -1.01 & 0.03 & 0.05 & -110.32 \\ 0 & 0 & 0 & 1 \end{bmatrix} $$

$$
{}^{W'}_{6}T_3 = \begin{bmatrix} -0.76 & 0.32 & 0.56 & -6.47 \\ -0.61 & -0.08 & -0.78 & -112.23 \\ -0.21 & -0.95 & 0.25 & -208.83 \\ 0 & 0 & 0 & 1 \end{bmatrix} \quad {}^{W'}_{6}T_4 = \begin{bmatrix} 0.48 & 0.83 & 0.26 & 232.83 \\ 0.60 & -0.11 & -0.78 & 24.16 \\ -0.64 & 0.54 & -0.56 & 17.44 \\ 0 & 0 & 0 & 1 \end{bmatrix}
$$

$$
{}^{W'}_{6}T_5 = \begin{bmatrix} 0.61 & -0.57 & 0.53 & -27.06 \\ 0.78 & 0.37 & -0.49 & 151.38 \\ 0.08 & 0.73 & 0.69 & 179.67 \\ 0 & 0 & 0 & 1 \end{bmatrix} \quad {}^{W'}_{6}T_6 = \begin{bmatrix} 0.48 & 0.83 & 0.26 & 232.83 \\ 0.60 & -0.11 & -0.78 & 24.16 \\ -0.64 & 0.54 & -0.56 & 17.44 \\ 0 & 0 & 0 & 1 \end{bmatrix}
$$

$$
{}^{W'}_{6}T_7 = \begin{bmatrix} 0.64 & -0.71 & 0.27 & -60.47 \\ 0.73 & 0.48 & -0.46 & 169.68 \\ 0.20 & 0.50 & 0.85 & 152.38 \\ 0 & 0 & 0 & 1 \end{bmatrix} \quad {}^{W'}_{6}T_8 = \begin{bmatrix} 0.11 & -0.75 & -0.65 & -160.03 \\ 0.28 & 0.64 & -0.70 & 140.30 \\ 0.96 & -0.11 & 0.29 & 99.99 \\ 0 & 0 & 0 & 1 \end{bmatrix}
$$

Figure 2.13 depicts the solution ${}^{W'}_{6}T_1$.

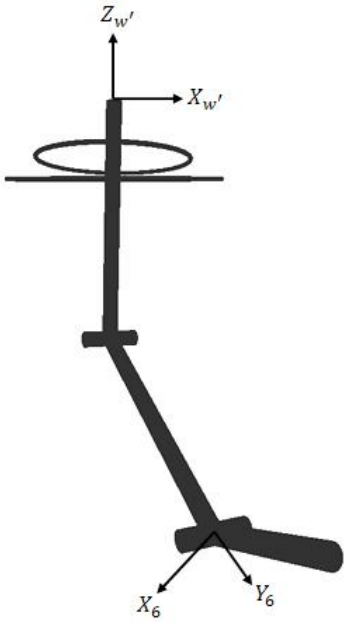

Figure 2.13: Graphical representation of solution ${}^{W'}_{6}T_1$

2.5.3 Case Study of Inverse Kinematic Model

In this section, the first set of forward kinematic solution, ${}^{W'}_{6}T_1$, is used for the inverse kinematic procedures and formulations.

Having the information of the position of the end-effector and the length of serial link 1 and 2, the value of joint 4 can be determined based on equation (2.10) and (2.11).

$$\theta_4 = -(180^\circ - \angle OBA) = -60.13^\circ \tag{2.37}$$

Where, $|OA| = \sqrt{40.49^2 + (-131.14)^2 + (-192.93)^2} = 237.30$; $|OB| = 146; |AB| = 128;$ $\angle OBA = 119.87^\circ$.

The position of joint 4 is determined geometrically by solving ${}^{W'}P_{X_4}$,${}^{W'}P_{Y_4}$ and ${}^{W'}P_{Z_4}$ from equation (2.12) to (2.15). In particular, any position of joint 4 satisfying equation (2.12) and (2.13) will be located at the circumference of the circle RO' as depicted in Figure 2.8. Whereas, as indicated by equation (2.15), the position of joint 4 should be also located on the plane of OBAC. Hence, the two intersections between the plane of OBAC and the circle RO', point B and C, should be two possible solutions.

By substituting the position information of the end-effector and the orientation information of Z_6 into to equation (2.14), the normal of the plane OBAC (vector $\widehat{N}$) is able to be determined.

$$\widehat{N} = [-0.11, -0.97, 0.15]^T \tag{2.38}$$

Two possible solutions of the position of joint 4 can be obtained by substituting equation (2.38) and the position of the end-effector into equation (2.12), (2.13) and (2.15).

$${}^{W'}P_{4_1} = [-121.23, 1.13, -81.35]^T;\ {}^{W'}P_{4_2} = [-2.23, -21.76, -144.35]^T \tag{2.39}$$

In order to determine the valid position of joint 4, the numerical value of frame $\{A\}$ is required to be solved. Substituting equation (2.38) and the position information of the end-effector into equation (2.16), the numerical result of frame $\{A\}$ can be obtained as shown in equation (2.40). Then, the two possible solutions of the position of joint 4 are fed into equation (2.17) to solve for $\hat{Sol}_1$ and $\hat{Sol}_2$. The result is presented in equation (2.41). Lastly, by taking the dot product of these two vectors with Y_A as shown in equation (2.42), one is

able to determine that $\hat{Sol}_1$ is in fact $\hat{AB}$, and ${}^{W'}P_{4_1}$ is the valid solution of the position of joint 4.

$$\widehat{X}_A = [-0.13, -0.57, -0.81]^T; \widehat{Y}_A = [-0.81, -0.40, 0.41]^T; \widehat{Z}_A = [-0.56, 0.71, -0.40]^T \quad (2.40)$$

$$\hat{Sol}_1 = [-0.54, -0.69, -0.46]^T; \hat{So1}_2 = [0.33, -0.26, -0.91]^T \quad (2.41)$$

$$PROJ_1 = \hat{Sol}_1 \cdot \widehat{Y}_A = 0.53; \quad PROJ_2 = \hat{Sol}_2 \cdot \widehat{Y}_A = -0.53 \quad (2.42)$$

With the position information of joint 4, the orientation of joint 4 with respect to $\{W'\}$ frame can be retrieved from equation (2.18) and (2.19). In particular, by substituting ${}^{W'}P_{4_2}$ into equation (2.18), the solution of ${}^{W'}_{P''}R$ can be determined. After that, substituting it to equation (2.19), the solution of ${}^{W'}_{4}R$ can be determined as shown in equation (2.43). The transformation from frame $\{P''\}$ to frame $\{P'\}$ is defined as shown in equation (2.44)

$${}^{W'}_{4}R = \begin{bmatrix} -0.86 & 0.47 & -0.11 \\ 0.02 & -0.18 & -0.97 \\ -0.50 & -0.86 & 0.15 \end{bmatrix} \quad (2.43)$$

$${}^{P''}_{P'}T = \begin{bmatrix} 0 & 1 & 0 & 0 \\ 0 & 0 & 1 & 0 \\ 1 & 0 & 0 & 0 \\ 0 & 0 & 0 & 1 \end{bmatrix} \quad (2.44)$$

Having solved the orientation of frame 4 with respect to $\{W'\}$, the solution for matrix $\mathbf{R}$ can be obtained through equation (2.20).

$$\mathbf{R} = \begin{bmatrix} 0.82 & -0.37 & 0.42 \\ 0.48 & 0.87 & -0.13 \\ -0.30 & 0.32 & 0.89 \end{bmatrix} \quad (2.45)$$

Having determined the orientation of the PCF with respect WCF, the three spherical joints angles can be solved through equation (2.21).

$$\begin{bmatrix} \theta_1 \\ \theta_2 \\ \theta_3 \end{bmatrix} = \begin{bmatrix} 30.15^\circ \\ 20.07^\circ \\ 25.25^\circ \end{bmatrix} \tag{2.46}$$

Having solved for the joint 1 to 4, the two wrist joints, joint 5 and 6, can be determined through equation (2.22).

$$\begin{bmatrix} \theta_5 \\ \theta_6 \end{bmatrix} = \begin{bmatrix} -50.36^\circ \\ 120^\circ \end{bmatrix} \tag{2.47}$$

This completes the solution of the inverse kinematics given the orientation and position of the end-effector as described by ${}^{W'}_{6}T_1$.

2.6 Jacobians

The Jacobian is a multidimensional form of the derivative and is a time-varying transformation [30]. In the field of robotics, Jacobian relates joint velocities to Cartesian velocities of the tip of the manipulator. Thus, for any given configuration of the manipulator, joint rates are related to the velocity of the tip in a linear fashion. Section 2.6.1 presents three Jacobian matrices that are applicable for the spherical parallel mechanism of the haptic device. The first Jacobian provides a mapping of an angle-set velocity vector to the angular velocity vector of the platform. The second Jacobian maps the actuator joint velocities to angular velocity of the platform. The first Jacobian is used in deriving the third Jacobian which maps the actuator joint velocities to angle-set velocity vector of the platform. The third Jacobian will also be used in force modeling. Section 2.6.2 is aim to obtain the linear velocity of the stylus of the haptic device based on the six individual actuator joint velocities.

2.6.1 Jacobians of Spherical Parallel Mechanism

Recall that the orientation of the platform coordinate frame $\{P\}$ with respect to the world coordinate frame $\{W\}$ is represented by $\mathbf{R}$ (equation 2.4) which is a Z-Y-X Euler rotation matrix. We can represent a skew-symmetric matrix S by the derivative of $\mathbf{R}$ [30] as shown in equation 2.48. If we define the angular velocity of the platform ω_p as $[\omega_{px}, \omega_{py}, \omega_{pz}]^T$, the skew-symmetric matrix S can also be expressed as equation 2.49. The velocity of the Z-Y-X Euler angle-set can be represented as shown in equation 2.50.

$$S = \dot{\mathbf{R}}\mathbf{R}^{-1} = \dot{\mathbf{R}}\mathbf{R}^{T} \tag{2.48}$$

$$S = \begin{bmatrix} 0 & -\omega_{pz} & \omega_{py} \\ \omega_{pz} & 0 & -\omega_{px} \\ -\omega_{py} & \omega_{px} & 0 \end{bmatrix} \tag{2.49}$$

$$\dot{\Theta}_{zyx} = \begin{bmatrix} \dot{\phi}_1 \\ \dot{\phi}_2 \\ \dot{\phi}_3 \end{bmatrix} \tag{2.50}$$

The relationship between the angular velocity of platform ω_p as the velocity of Z-Y-X Euler angle-set can be formed as shown in equation 2.51, where $E_{zyx}(\Theta_{zyx})$ is a Jacobian relating Z-Y-X Euler angle-set velocity vector to the angular velocity vector.

$$\omega_p = E_{zyx}(\Theta_{zyx})\dot{\Theta}_{zyx} \tag{2.51}$$

In order to solve $E_{zyx}(\Theta_{zyx})$ matrix, we first establish the following equation by combining equation 2.48 and equation 2.49.

$$\dot{\mathbf{R}}\mathbf{R}^{\mathbf{T}} = \begin{bmatrix} 0 & -\omega_{pz} & \omega_{py} \\ \omega_{pz} & 0 & -\omega_{px} \\ -\omega_{py} & \omega_{px} & 0 \end{bmatrix} \tag{2.52}$$

where, $\mathbf{R}$ can be represented as

$$\mathbf{R} = \begin{bmatrix} r_{11} & r_{12} & r_{13} \\ r_{21} & r_{22} & r_{23} \\ r_{31} & r_{32} & r_{33} \end{bmatrix} .$$

We can represent the angular velocity of the platform $\omega_{px}, \omega_{py}, \omega_{pz}$ as equation 2.53 - equation 2.55.

$$\omega_{px} = \dot{r}_{31}r_{21} + \dot{r}_{32}r_{22} + \dot{r}_{33}r_{23} \ , \tag{2.53}$$

$$\omega_{py} = \dot{r}_{11}r_{31} + \dot{r}_{12}r_{32} + \dot{r}_{13}r_{33} \ , \tag{2.54}$$

$$\omega_{pz} = \dot{r}_{21} r_{11} + \dot{r}_{22} r_{12} + \dot{r}_{23} r_{13} \ . \tag{2.55}$$

Recall that the $\mathbf{R}$ matrix is,

$$\mathbf{R} = \begin{bmatrix} c\phi_1 c\phi_2 & c\phi_1 s\phi_2 s\phi_3 - s\phi_1 c\phi_3 & c\phi_1 s\phi_2 c\phi_3 + s\phi_1 s\phi_3 \\ s\phi_1 c\phi_2 & s\phi_1 s\phi_2 s\phi_3 + c\phi_1 c\phi_3 & s\phi_1 s\phi_2 c\phi_3 - c\phi_1 s\phi_3 \\ -s\phi_2 & c\phi_2 s\phi_3 & c\phi_2 c\phi_3 \end{bmatrix} .$$

Therefore, $E_{zyx}(\Theta_{zyx})$ matrix can be represented as equation 2.56 and ω_p can be represented as time derivative of Z-Y-X Euler angle-set as equation 2.57.

$$E_{zyx}(\Theta_{zyx}) = \begin{bmatrix} 0 & -s\phi_1 & c\phi_1 c\phi_2 \\ 0 & c\phi_1 & s\phi_1 c\phi_2 \\ 1 & 0 & -s\phi_2 \end{bmatrix} \tag{2.56}$$

$$\omega_p = \begin{bmatrix} 0 & -s\phi_1 & c\phi_1 c\phi_2 \\ 0 & c\phi_1 & s\phi_1 c\phi_2 \\ 1 & 0 & -s\phi_2 \end{bmatrix} \begin{bmatrix} \dot{\phi}_1 \\ \dot{\phi}_2 \\ \dot{\phi}_3 \end{bmatrix} \tag{2.57}$$

Therefore, the angular velocity vector of the platform frame $\{P\}$ with respect to the world coordinate frame $\{W\}$ can be computed given the instantaneous set of Z-Y-X Euler angle-set $\dot{\phi}_1, \dot{\phi}_2$ and $\dot{\phi}_3$.

Next, we derive the Jacobian which maps the actuator joint velocities $(\dot{\theta}_1, \dot{\theta}_2, \dot{\theta}_3)$ to angular velocity of the platform (ω_p). The following equation can form such relationship :

$$\dot{\theta} = J\omega_p, \tag{2.58}$$

where $\dot{\theta}$ is the vector of the actuated joint rates of the spherical parallel mechanism and is expressed as $[\dot{\theta}_1, \dot{\theta}_2, \dot{\theta}_3]^T$. From [33], the general velocity equation for spherical parallel manipulators can be expressed as:

$$A\omega_p = B\dot{\theta} \tag{2.59}$$

where,

$$A = \begin{bmatrix} (W_1 \times V_1)^T \\ (W_2 \times V_2)^T \\ (W_3 \times V_3)^T \end{bmatrix}$$

$$B = diag(U_i \times W_i \cdot V_i), \quad i = (1, 2, 3)$$

Recall that, U_i, W_i and V_i $(i = 1, 2, 3)$ are the actuator joint axis, passive joint axis and platform joint axis of the three kinematic chain of the spherical parallel mechanism. Based on equation (2.58) and (2.59), we can claim that the Jacobian J that maps the actuator joint velocities to angular velocity of the platform is $B^{-1}A$.

For the control purposes, we use equation 2.51 to express the angular velocity vector by using the time derivatives of the Z-Y-X Euler angle-set. Substituting equation (2.51) and (2.56) into (2.59), the velocities of the three actuator joints of the spherical parallel mechanism can then be expressed as a function of time derivatives of the three Euler angles as shown in equation 2.60.

$$\dot{\theta} = JE_{zyx}(\Theta_{zyx})\ \dot{\Theta}_{zxy} = (B^{-1}A)E_{zyx}(\Theta_{zyx})\ \dot{\Theta}_{zxy} \tag{2.60}$$

The term $(B^{-1}A)E_{zyx}(\Theta_{zyx})$ is regarded as the extended Jacobian matrix, which maps the actuator joint velocities to Z-Y-X Euler angle-set velocity vector of the platform.

2.6.2 Velocity of the Stylus of the Haptic Device

Based on equation 2.58, we can express the angular velocity of the platform in terms of three spherical actuated joint angles as $\omega_p = J^{-1}\dot{\theta}$. Next, we express the angular velocity of the platform with respect to the platform frame as shown in equation 2.61. It is the start of the velocity "propagation" from the platform coordinate frame PCF to the stylus coordinate frame. Equation 2.62 and 2.63 describes the angular and linear velocity propagation where i is $\{p\}$,$\{4\}$,$\{5\}$ and $\{6\}$ respectively. Equation 2.64 depicts the linear velocity of the stylus coordinate frame with respect to the world coordinate frame WCF.

$${}^{p}\omega_p = {}^{p}_{w}R\ \omega_p \tag{2.61}$$

$${}^{i+1}\omega_{i+1} = {}^{i+1}_{i}R\ {}^{i}\omega_i + \dot{\theta}_{i+1}\ {}^{i+1}\widehat{Z}_{i+1} \qquad (i = p, 4, 5, 6) \tag{2.62}$$

$${}^{i+1}v_{i+1} = {}^{i+1}_{i}R\ ({}^{i}v_i + {}^{i}\omega_i \times {}^{i}P_{i+1}) \tag{2.63}$$

$$^{w}v_6 = \mathbf{R}\ {}^{p}_{4}R\ {}^{4}_{5}R\ {}^{5}_{6}R\ {}^{6}v_6 \tag{2.64}$$

2.7 Force Modeling

In this thesis work, we propose a two-step approach to solve for actuator joint torques given the desired force and moment at the stylus of the haptic device. Firstly, we determine the joint torques of serial mechanism and the resultant moment vector exerted at the platform. Specifically, an inward iteration method introduced in [30] is utilized to determine the actuator joint torques of joint 6 (τ_6) to joint 4 (τ_4) and the moment vector at the platform (M_p) giving the desired force and moment vector acting at the stylus. Please note that the gravity force acting on the serial mechanism is excluded in this analysis.

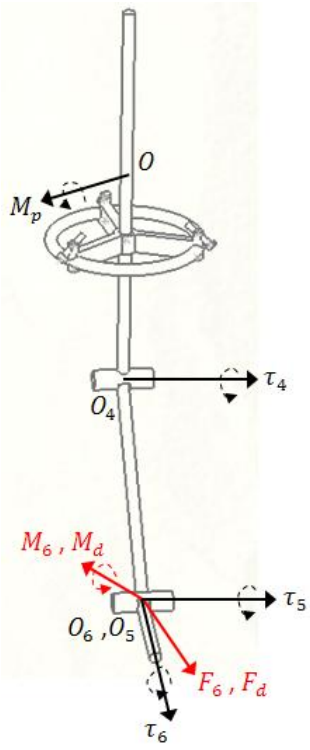

Figure 2.14: Force and moment mapping description from the stylus to joint 6, joint 5, joint 4 and the platform

Figure 2.14 depicts the desired force and moment vector ($M_6/M_d, F_6/F_d$) at the stylus;

the actuator torque vectors of joint 6 (τ_6), joint 5 (τ_5) and joint 4 (τ_4); the moment exerted at the platform (M_p). We represent the force and moment acting on the end-effector as equation (2.65).

$$f_6 = [f_{x_6}, f_{y_6}, f_{z_6}]^T; \quad M_6 = [M_{x_6}, M_{y_6}, M_{z_6}]^T \tag{2.65}$$

The following equations analytically describe the static force "propagation" from the stylus to the platform:

$${}^i f_i = {}^i_{i+1}R \ {}^{i+1}f_{i+1} \ , \quad (i = 5, 4, P), \tag{2.66}$$

$${}^i M_i = {}^i_{i+1}R \ {}^{i+1}M_{i+1} + {}^i P_{i+1} \times {}^i f_i \ , \quad (i = 5, 4, P), \tag{2.67}$$

$$\tau_i = {}^i M_i^T \ {}^i\hat{Z}_i \ , \quad (i = 6, 5, 4), \tag{2.68}$$

Substituting equation (2.65) and the transformation matrices discussed in kinematic modeling section into equation (2.66) and (2.67), one is able to obtain the analytical expression of the moment acting on joint 5, 4 and the platform in terms of the force and moment exerted at the stylus. Since the Z axis is the axis of rotation for joint 6, 5 and 4, the torques of joint 6, 5 and 4 are represented as equation (2.68). Whereas, since the platform has 3DOF, its torque vector is same as the moment vector which is represented as equation (2.67). The analytical expressions of the torque of joint 6, 5, 4 and the moment exerted at the platform are shown in equation 2.69 - 2.72. M_{px}, M_{py} and M_{pz} are the moment along X, Y and Z axis of the platform frame $\{P\}$ respectively.

$$\tau_6 = M_{z6} \ , \tag{2.69}$$

$$\tau_5 = -s\theta_6 \ M_{x_6} - c\theta_6 \ M_{y_6} \ , \tag{2.70}$$

$$\tau_4 = -s\theta_6 \ M_{x_6} - c\theta_6 \ M_{y_6} + 120 f_{z_6} \tag{2.71}$$

$$M_p = \tau_p = [M_{px}, M_{py}, M_{pz}]^T \tag{2.72}$$

Having determined the joint torques of serial mechanism and the resultant moment vector exerted at the platform, the actuator torques of the spherical parallel mechanism can be determined based on the moment exerted at the platform. Figure 2.15 depicts the moment vector M_p exerted at the platform; the actuator torque vectors of joint 1, joint 2 and joint 3.

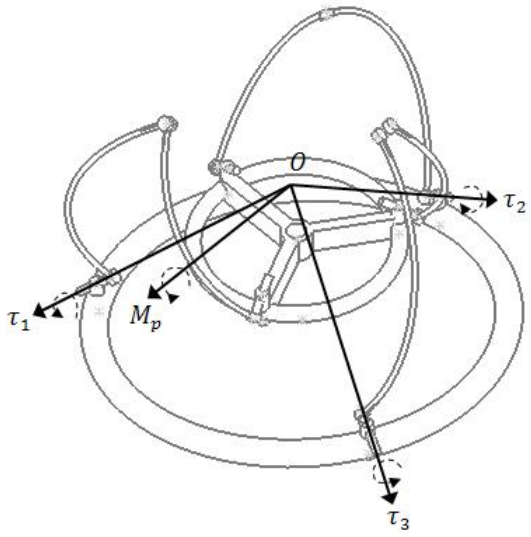

Figure 2.15: Force mapping from the platform to joint 1, joint 2 and joint 3

The quasi-static model [33] is applied to establish the relationship between the moment exerted at the platform and the actuator joint torques of the spherical parallel mechanism given that the velocities caused by the user are relatively small. In mechanics of a rotation system, the power can be formulated as $power = torque \cdot angular\ velocity$. If we regard the spherical parallel mechanism as a rotation system, the dot product of actuator joint torque vector and actuator joint velocity vector can be regarded as input power of the system while the dot product of the moment exerted at the platform and the velocity of Z-Y-X Euler angle-set can be regarded as output power of the system. Equation (2.73) is obtained by equaling the input and output powers of the rotation system.

$$M_p{}^T \dot{\Theta}_{zyx} = \tau^T \dot{\theta} \tag{2.73}$$

Where τ is the torque vector of actuator joints of the spherical parallel mechanism and is expressed as $[\tau_1, \tau_2, \tau_3]^T$. The extended Jacobian expression $(B^{-1}A)E_{zyx}(\Theta_{zyx})$ is utilized

to establish the relationship between τ and M_p based on B, A and $E_{zyx}(\Theta_{zyx})$ matrices. Substituting equation (2.60) to (2.73) and simplify, one is able to obtain:

$$\tau = B^T(AE_{zyx}(\Theta_{zyx}))^{-T}M_p \tag{2.74}$$

Note that the term of $\dot{\Theta}_{zyx}$ was canceled out during the algebraic manipulation. In other words, this equation should be able to satisfy any arbitrary small velocities of the platform. Overall, this equation relates the torque exerted at the mobile platform to the three actuated joint torque of the spherical parallel mechanism.

Chapter 3

Experimental Studies

3.1 Introduction

Haptic interfaces are aim to provide users intuitive and realistic force information while interacting with the virtual or remote tele-operation environment. The computed interactive force between the user and a virtual object is rendered to the user via the haptic device.

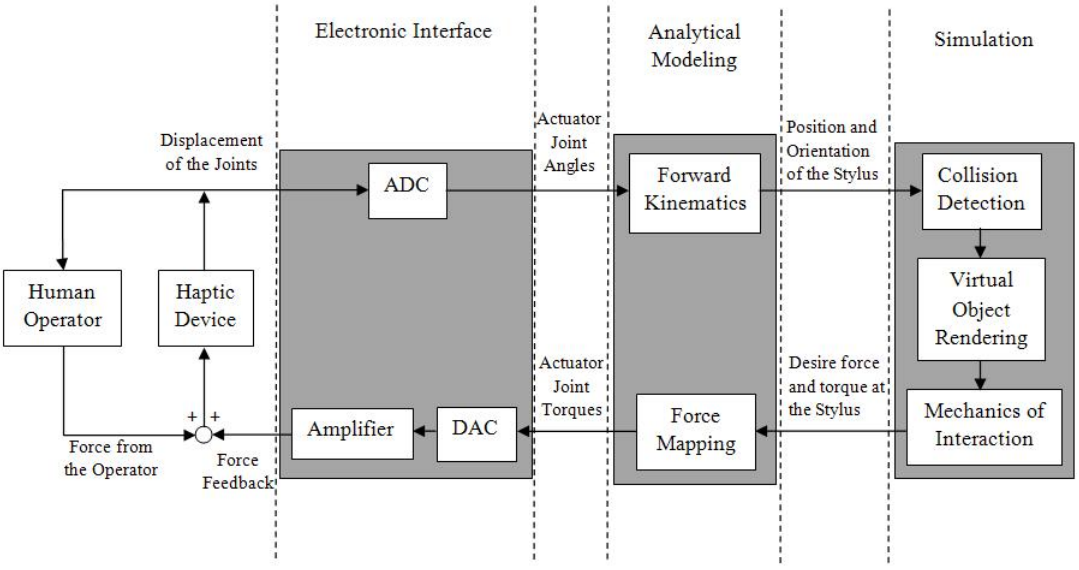

Figure 3.1: Block diagram of a typical haptic rendering loop with force display

Figure 3.1 shows a block diagram of a typical haptic rendering loop with force display.

It can be divided into five sections: human operator, haptic device, electronic interface, analytical modeling and simulation. The electronic interface relates the continuous physical device to the discrete virtual world. In particular, it converts the continuous rotation of each actuator joints into discrete joint angles. It also converts the values of actuator joint torques to analog voltage/current. Due to the elaborate sensory perception of the human hand, which registers even very small oscillations, many research studies have shown that update rates of up to 1 kHz or above are desired for haptic rendering of any physical effects. The analytical model determines the position and orientation of the stylus of the haptic device based on the value of actuator joint angles. It also computes the actuator joint torques based on the desired force/torque at the stylus of the haptic device. The simulation section consists of three processes: collision detection, virtual object rendering and mechanics of interaction. It takes the position and orientation of the stylus of the haptic device as input, determines the desired force and torque needs to be rendered at the stylus based on the collision detection and mechanics of interaction.

In previous chapter, the analytical models of the haptic device have been established. In this chapter, we investigate the electronic interface and the simulation sections. In addition, experimental studies of the proposed haptic user interface are presented. The chapter is organized as follows. In Section 3.2, we introduce the hardware setup of the electronic interface. In Section 3.3, the software framework of the haptic interface are described. After that, we discuss the calibration issues in Section 3.4. Experimental studies examining the kinematic correspondence and force correspondence are presented in Section 3.5 and Section 3.6 respectively. In Section 3.7, we present the preliminary results when users interacts with virtual environments through the proposed haptic interface.

3.2 Electronic Interface

In this section, the electronic interface of the haptic user interface are investigated. We first provide an overview of the system architecture of the electronic interface. Then, thorough description on the establishment of the electronic interface is presented.

3.2.1 Overview of the System Architecture

The system consists of four major components: the PC running under Windows XP, data acquisition system (DAS), the 6DOF haptic device and the ATI NANO 25 F/T sensor and

the associated control system. The system block diagram of the experimental hardware setup is shown in Figure 3.2.

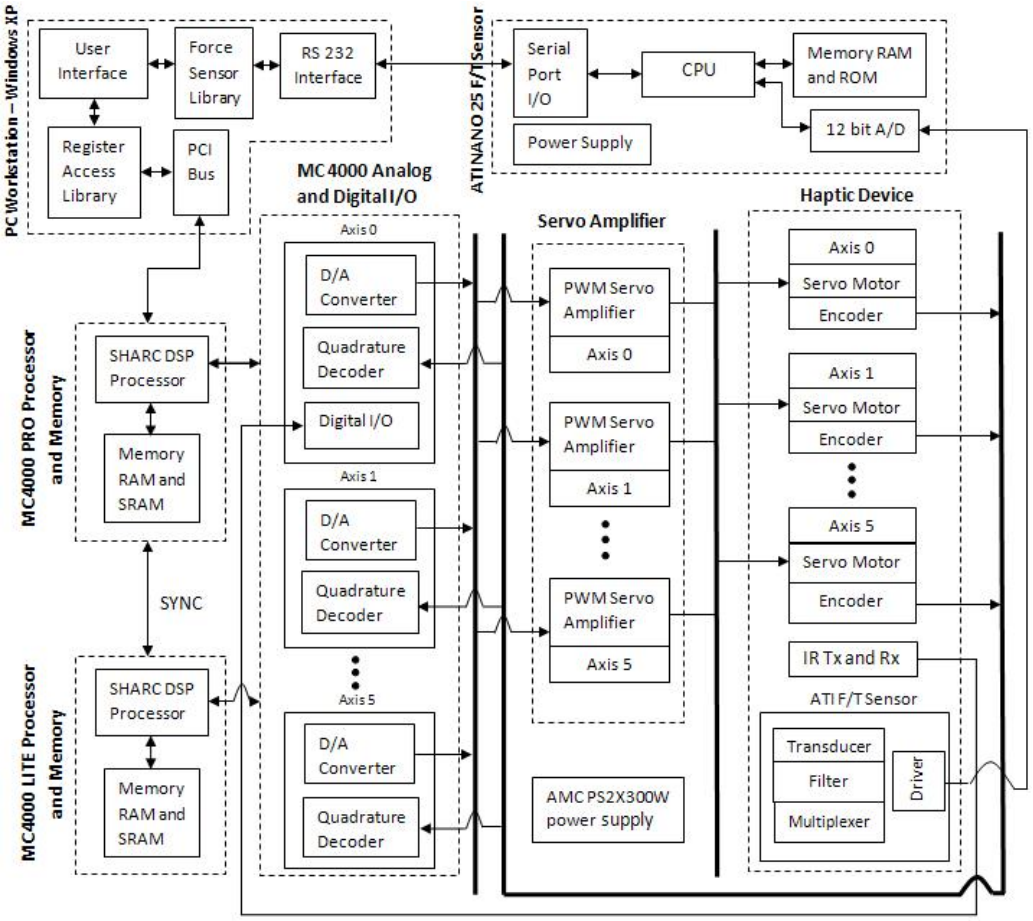

Figure 3.2: System block diagram

The application software is running in the Microsoft Visual Studio C++ environment and is responsible for accessing the values of the six actuator joint angles, determining the position and orientation of the end-effector through the kinematic model, determining the torque value at each joint based on the force model, rendering the device configuration and the virtual environment through OpenGL and collect the F/T data from the ATI NANO 25 F/T sensor. It is the driver for communicating with the DAS.

The DAS consists of two Precisioin MicroDynamics (PMDi) MC4000 PCI-Bus motion control DSP boards, six Maxon RE 25 Brushed DC motors and six Advanced Motion Control

(AMC) 12A8 Pulse Width Modulated (PWM) servo amplifiers which are powered by two AMC PS2X300W power supplies. Six independent axes/groups of analog and digital I/O (e.g. quadrature decoder, digital to analog converter) from the two PMDi MC4000 DSP boards are utilized to interface with the six actuator joints of the haptic device. The AMC PWM servo amplifier supplies pulse width modulated signal to the corresponding actuator based on the reference signal provided by the Digital to Analog Converter (DAC) of the DSP board.

The 6-DOF haptic device is electronically interfaced by six Maxon RE 25 DC motors each of which is directly coupled with Agilent Technologies HEDS-5540 optical encoder. The DC motor is capable of providing 240 mNm peak torque and a velocity of 25.6 rad/sec for a nominal power consumption of 20 W. The encoder is operated at the resolution of 500 Counts Per Revolution (CPR). The three DC motors and the associated encoders for the three spherical joints are located on the base platform. The set of DC motor and encoder for the elbow joint (joint 4) is mounted at the end of the serial link l_1 while, in order to reduce the moving inertia, the rest two sets for the two wrist joints (joint 5 and 6) are located on the mobile platform which is supported by the three passive links and the spherical passive joint. The data sheets of the AMC PWM servo amplifier, AMC PSX300W power supplies, Maxon RE 25 Brushed DC motor and the HEDS-5540 optical encoder are attached in the Appendix A.

3.2.2 Data Acquisition System

The core of the DAS is the two PMDi MC4000 PCI-Bus motion control DSP boards (MC4000 PRO board and MC4000 LITE board). The majority of the facilities of these two boards are identical. The differences will be highlighted throughout this section. We first introduce the crucial components or facilities and the initial configuration of the DSP board. Figure 3.3 describes the layout of the DSP board. The SHARC DSP processor (entry #3 in Figure 3.3) is running at 40 MHz while the internal Programmable Interval Timer (PIT) is set at 1 KHz to be better suited for force reflection. The board select jumper J5 (entry #10 in Figure 3.3) allows the user to set the board number when more than one board is presented in the PC at one time. In our case, the MC4000 PRO is configured as board #0 while the MC4000 LITE is configured as board #1. The SYNC signal (entry #1 in Figure 3.3) is used to synchronize the activities between MC4000 PRO board and MC4000 LITE board (e.g. the DAC outputs and encoder inputs). The Altera FPGA (entry

#11 in Figure 3.3) handles the data from the encoders. The connectors J17 and J20 (entry #9 in Figure 3.3) are 60-pin connectors, each of which provide access to the signals for two axes/groups of analog and digital I/O. The axes are separated physically, each of which has 30 pins of the 60 pin allotted to it. For the complete description of the PMDi MC4000 PCI-Bus motion control DSP board please consult the manufacturer specification.

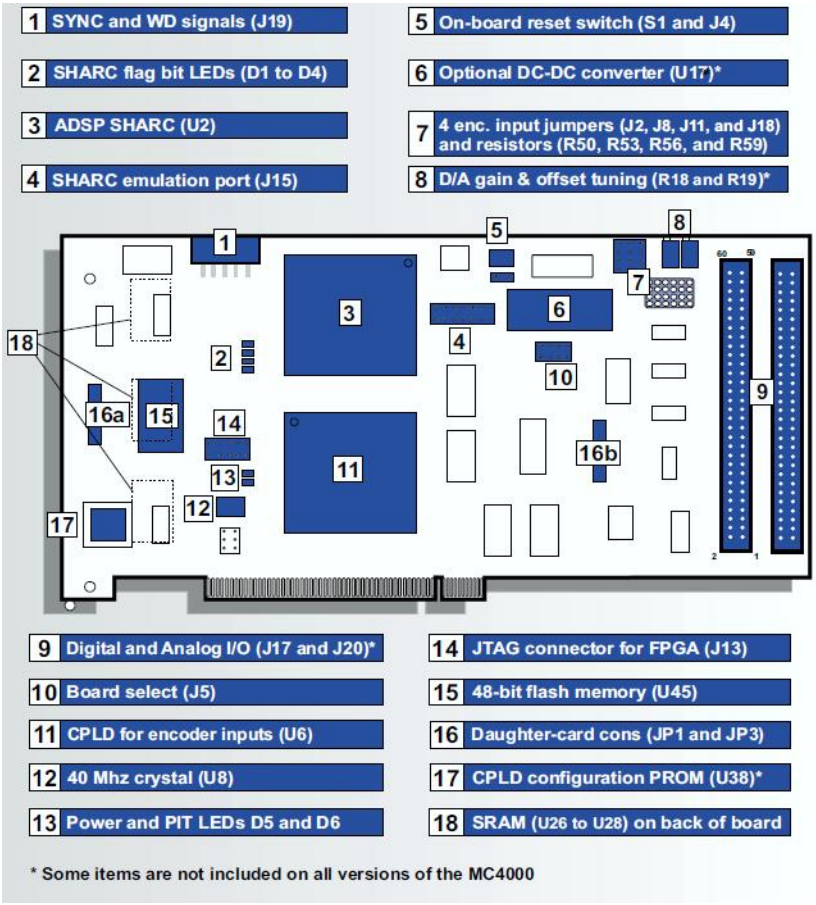

Figure 3.3: The PMDi MC4000 PCI-Bus motion control DSP board layout provided by the manufacturer

As mentioned in section 3.2.1, six axes/groups of analog and digital I/O from the two PMDi MC4000 DSP boards are utilized to interface with the six actuator joints of the haptic device. The first four actuator joints (joint 1 to 4) are associated with the four axes/groups of I/O of MC4000 PRO board, while the last two actuator joints (joint 5 and 6) are associated with the first two axes/groups of I/O of MC4000 LITE board. Figure

3.4 depicts the pin layout of the first axis of I/O of the MC4000 PRO board. The rest of three axes are identical with the first axis. The pin layout of I/O axes of the MC4000 LITE board is the same as that of the MC4000 PRO board except that there is no connection for pin 22-25 and pin 29-30. The absence of the I/O will not cause any issue for the electronic interface because they are irrelevant to the proposed application.

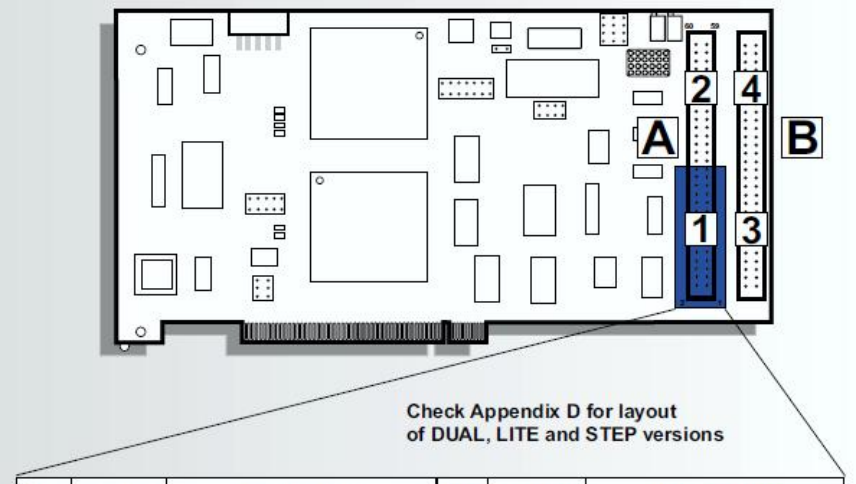

Pin	Function	Description	Pin	Function	Description
30	AD-	Analog Input -ve Differential Line	29	AD+	Analog Input +ve Differential Line
28	DAC	Analog Output	27	AGND	Analog Ground
26	AGND	Analog Ground	25	HSD3	Position Capture In
24	HSD2	Position Compare Out	23	HSD1	Stepper Motor - Direction1
22	HSD0	Stepper Motor - Pulse1	21	GND	Digital Ground
20	DOUT1	Amp Enable 2	19	DOUT0	Amp Enable1
18	+5V	+5V from PC	17	GND	Digital Ground
16	DIN5	LIM2-	15	DIN4	LIM2+
14	DIN3	HOME2	13	DIN2	LIM1-
12	DIN1	LIM1+	11	DIN0	HOME1
10	GND	Digital Ground	9	+12V	+12V Power for Encoders
8	Z*	Encoder Index Pulse Complement	7	Z	Encoder Index Pulse
6	B*	Encoder Channel B Complement	5	B	Encoder Channel B
4	A*	Encoder Channel A Complement	3	A	Encoder Channel A
2	GND	Encoder Ground	1	+5V	+5V Power for Encoders

Figure 3.4: The pin layout of the first axis/group of I/O of the MC4000 PRO board provided by the manufacturer

The six axes/groups of I/O are connected with three PMDi optical breakout boards for the purpose of easy pin access and better protection of the DSP board. Each breakout board accommodates two groups of axes from a single 60-pin connector (e.g. J17 in figure 3.3) and allows access to all 30 signals from each individual axis by separating the two axes into logical banks of terminal strips that are clearly labeled. The breakout board also provides

isolation of digital signals on each axis/groups of I/O from the peripheral devices attached to the breakout board (e.g. motors and amplifiers). Figure 3.5 describes the layout of the breakout board for one axis of I/O. Looking at the terminal block (J6), every I/O signal and the associated pin number of one axis is clearly labeled.

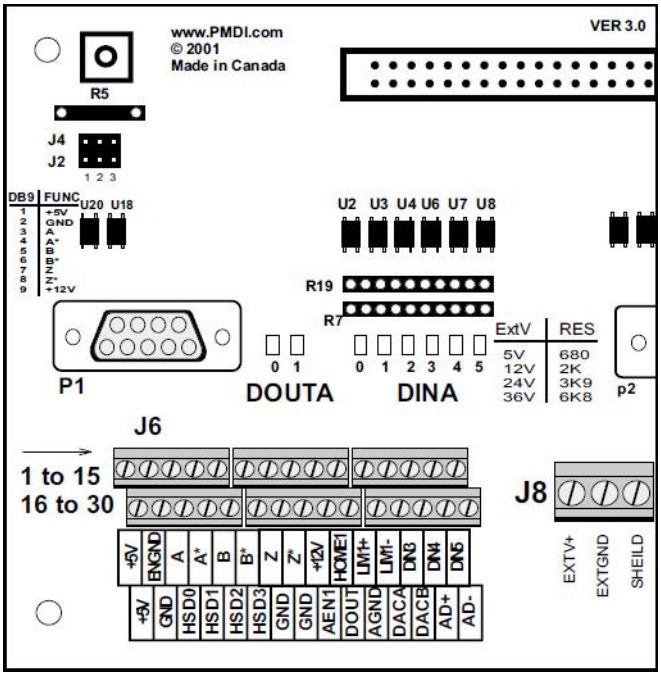

Figure 3.5: The layout of the PMDi breakout board for one axis of I/O provided by the manufacturer

Pin 1, 2, 3 and 5 ("+5V", "ENGND", "A" and "B") are the quadrature encoder inputs which are to be connected with the HEDS-5540 optical encoder. Specifically, pin 1 and 2 are responsible for providing +5V power and ground for the encoder. Pin 3 and 5 are responsible for receiving signals from channel A and B of the encoder. Channels A and B correspond to two different photo sensors, which are oriented a quarter-pitch off each other. The quarter pitch offset allows us to monitor the direction of the movement (either clockwise or counter clockwise). For example, if the pulse from channel A leads channel B as described in figure 3.6, the motor moves counter clockwise, as seen from the encoder end. The MC4000 DSP board quadrature encoder inputs decrement or increment the counter whenever an edge is detected from either channel A or channel B signals depending on the direction of motion. Thus, for every count of the encoder, the decoder will increment 4

times as shown in figure 3.6. Since the encoder has 500 CPR, the decoder will have 2000 CPR.

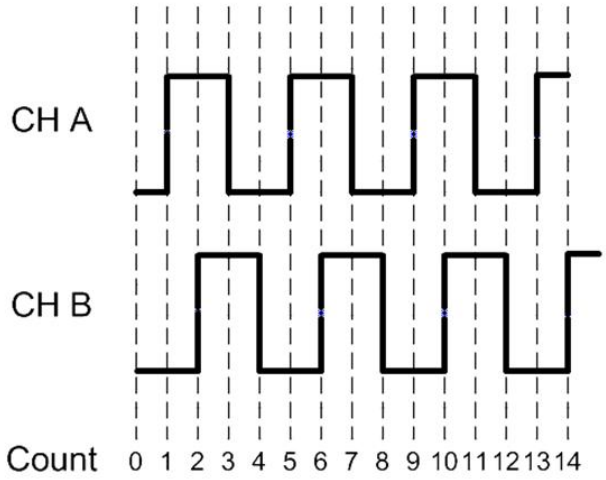

Figure 3.6: PMDi MC4000 DSP board decoder signals

Pin 27 and 26 ("DAC" and "AGND") are DAC output and analog ground respectively. These two pins are responsible for providing two reference voltages ("+REF IN" and "-REF IN") to the AMC PWM servo amplifier which provides the pulse width modulated signal with high switching frequency to drive the Maxon Brushed DC motor. Figure 3.7 shows the connection between the breakout board, servo amplifier and DC motor for one axis. The range of DAC output is -10V - +10V. The servo amplifier is configured to use in current mode, hence desired torque output can be controlled via two reference voltages. The servo amplifier receives a differential analog input pair which is the difference voltage level between the DAC output and the analog ground. The sign of the differential voltage determines the motor turning direction. The amplitude of the differential voltage determines the motor torque. The calibration of this mapping between reference voltage and desired torque is presented in the section 3.4.2. Pin 16 and 17 ("+5V" and "GND") are the 5V from PC and digital ground. These two pins are connected with "EXTV+" and "EXTGND" of the breakout board to provide isolation of digital signal on each axis from the peripheral devices attached to the breakout board. The description of the aforementioned I/O pins and the connections as shown in figure 3.7 applies to all six axes. The following description of connection of pin 11 and 23 only applies to the first axis.

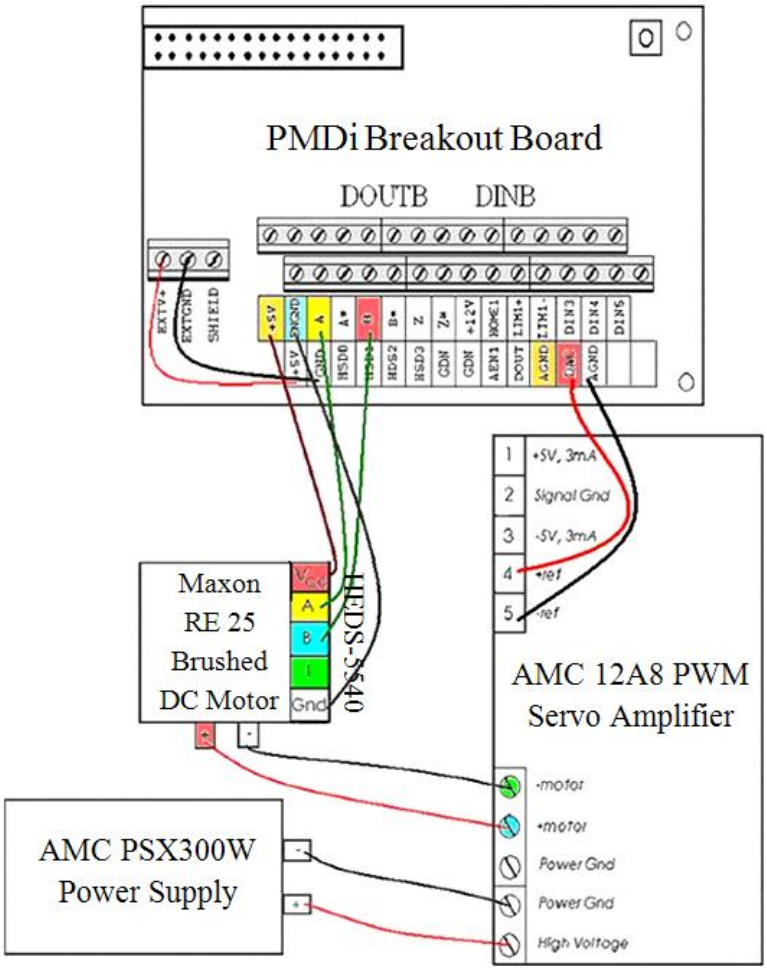

Figure 3.7: The wiring diagram between the breakout board, servo amplifier, DC motor and encoder of one axis

Pin 11 and 23 ("LIM1+" and "GND") are digital input and digital ground. These two pins are responsible for receiving the signal from the output of the physical home orientation recognition system as shown in figure 3.25. It will be discussed in section 3.4.1.

3.3 Application Software Design

In this section, the application software design of the haptic user interface is investigated. We first present an overview of the application software architecture. Then, the key components are described in greater detail.

3.3.1 Overview of Application Software Architecture

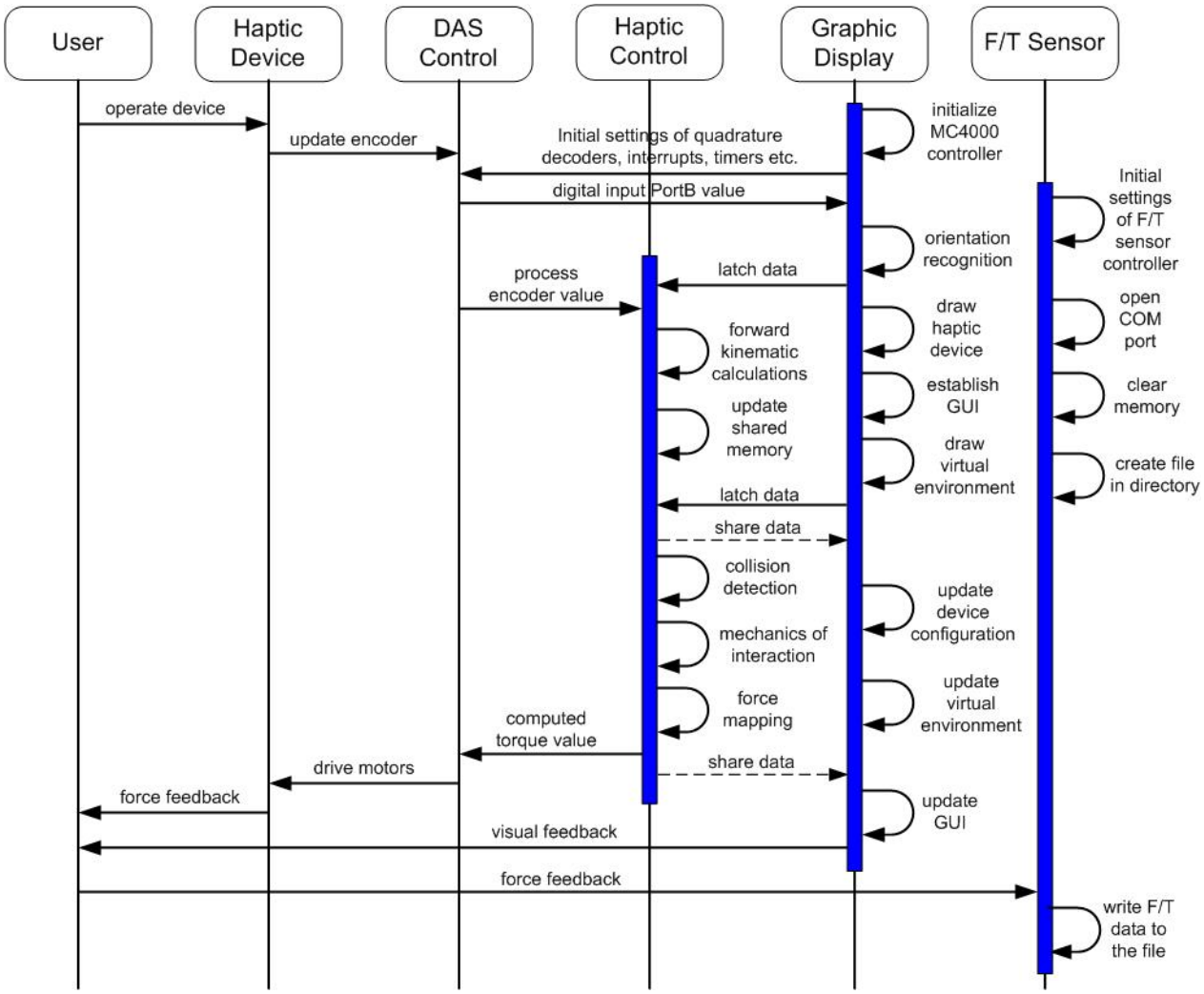

Figure 3.8: Software sequence diagram of the haptic user interface

The application software is established in Microsoft Visual C++ 6.0 environment through

Windows XP operating system. Figure 3.8 shows an overall software sequence diagram of the haptic user interface and the allocation and distribution of the tasks. As shown, the user and the haptic device represent the human operator manipulating the physical 6-DOF haptic device while observing the virtual environment and the Graphic User Interface (GUI) on the PC monitor. The DAS Control task represents the firmware of the two MC4000 DSP cards. The host PC's processor accesses the MC4000 boards resources through PCI bus. From the PCI bus, the MC4000 registers are mapped into 32-bit memory. At boot time the host PC's processor handles the allocation of board resources assigning the base address. Table 3.1 illustrates the DSP and PCI address and description of MC4000 card registers which are used in the application software. The information provided from table 3.1 is the same for both MC4000 PRO card and MC4000 LITE card. Table 3.2 summarizes the board communication and register functions that are used in the application software. These functions are provided by the manufacturer. With proper initialization of the two MC4000 boards, the DAS Control task is able to provide encoder value, interpret digital input data and convert the digital joint torque value to analog reference voltage to the servo amplifier under the command of register functions as shown in table 3.2.

Table 3.1: MC4000 card register map (registers that are used in the application software)

DSP	PCI	Register Name	Description
0x00	0x00	MC_PIT	Programmable interval timer
0x01	0x02	MC_WD	Watchdog timer
0x02	0x04	MC_GATE	Timer gate
0x03	0x06	$MC\_SYNCCTRL$	SYNC control
0x04 - 0x0B	0x08 - 0x0F	MC_DAC0-7	Digital to analog converter
0x15	0x22	MC_DIGINB	Port B (Digital in)
0x20	0x34	$MC\_INTFLGHOST$	Host interrupt flags
0x21	0x35	$MC\_INTENAHOST$	Host interrupt enable
0x30 - 0x37	0x40 - 0x4E	$MC\_QDCOUNT0-7$	Decoder0 - 7 count
0x38 - 0x3F	0x50 - 0x5E	$MC\_QDMODE0-7$	Decoder0 - 7 mode

Multi-threaded approach is employed in the application software design. It consists of three threads, one main thread (Graphic Display thread) and two child threads (Haptic Control thread and F/T sensor thread) as shown in figure 3.8. The Graphic Display thread is responsible for initializing the two MC4000 DSP boards and graphics rendering (e.g. the GUI, the graphic display of the haptic device configuration and the virtual environment).

Table 3.2: The summary of the board communication and register functions that are used in the application software

Header File	Board Communication and Register Functions	Description
mcprim.h	mcOpen()	Initialize and allocate board data structure
	mcClose()	Free board data structures
	mcReadReg()	Read from one MC4000 register
	mcWriteReg()	Write to one MC4000 register
mcinitnt.h	mcIntStart()	Start interrupt handling
	mcIntStop()	Stop interrupt handling
	mcIntWait()	Wait until next interrupt occurs
mcreg.h	mcDACwrite()	Write one DAC channel
	mcDIOreadPortB()	Read digital input port B
	mcEncPhase()	Set phase inversion of one encoder input
	mcEncSoftPreloadN()	Force a preload of the encoder counter of multiple sequential encoder inputs
	mcEncWriteN()	Write encoder preload registers of multiple sequential encoder inputs
	mcIruptClear()	Clear host interrupt flags
	mcIruptEnable()	Enable host interrupt mask bit
	mcIruptReadFlags()	Read host interrupt flags
	mcPITload()	Load the programmable interval timer
	mcSYNCconfig()	Configure the source of the on-board and external SYNC signals

The Haptic Control thread is in charge of background computations such as forward kinematic calculations, force mapping, collision detection, and mechanics-base interaction. The F/T sensor thread is in charge of initiating the communication port, initializing the F/T sensor controller and collecting the F/T sensor data. The operating frequencies of the Graphic Display thread is set to be 50 Hz. The Haptic Control thread is running at 1 KHz to provide more realistic force feedback. The F/T sensor thread is running at 40 Hz in correspond to the operating frequency of the F/T sensor controller.

3.3.2 Graphic Display Thread

The Graphic Display thread starts with initialization task of the MC4000 PRO and MC4000 LITE DSP boards. Figure 3.9 describes the flowchart of initialization task. The task begins with allocating and initializing the data structure for communication with the two MC4000 boards to facilitate the implementation of the board communication and register functions. The MC4000 PRO board is identified as board #0 while MC4000 LITE board is identified as board #1.

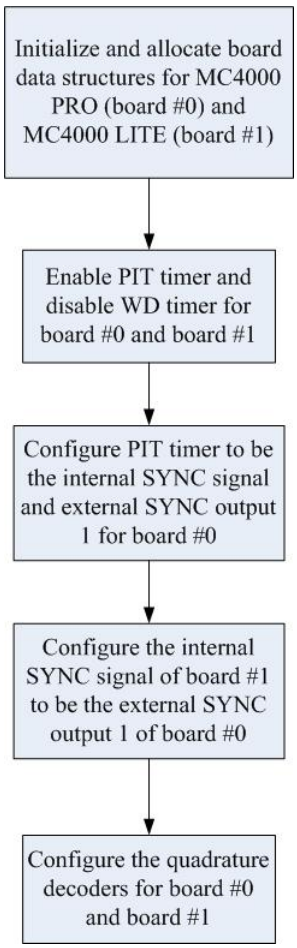

Figure 3.9: The flowchart of initialization of MC4000 PRO and MC4000 LITE board

There are two timers available on the MC4000 board: the Programmable Interval Timer (PIT) and the Watch Dog (WD) timer. The PIT is enabled for both boards because it

is capable of generating a SYNC pulse to latch the encoders, DACs and ADCs at regular intervals. The WD timer is disabled for both boards because it interferes the operation of DACs (WD timer counts at 1/8 of the PIT clock rate and forces the DAC outputs to zero every time when timeout of the WD timer occurs). In order to synchronize board #0 and board #1, SYNC signals of both boards need to be configured. There are three SYNC signals on each boards: internal SYNC (for the DACs, ADCs and quadrature encoders on the board), external SYNC output 1 and external SYNC output 2. The internal SYNC of board #0 is configured to be the PIT timer to latch the encoders and DACs. The external SYNC output 1 of board #0 and the internal SYNC of the board #1 are configured to be the PIT timer of board #0 to synchronize the board #1 with board #0. Having completed the configuration of the timer of the two MC4000 boards, the quadrature encoders inputs can be configured. Figure 3.10 exhibits the block diagram of the encoder read and write interface. The encoder latch latches the encoder count on the SYNC pulse and remains unchanged until a new SYNC pulse is generated. To ensure the encoder count starts from 0, we write 0 to the encoder preload register and enable the software preload for every axis.

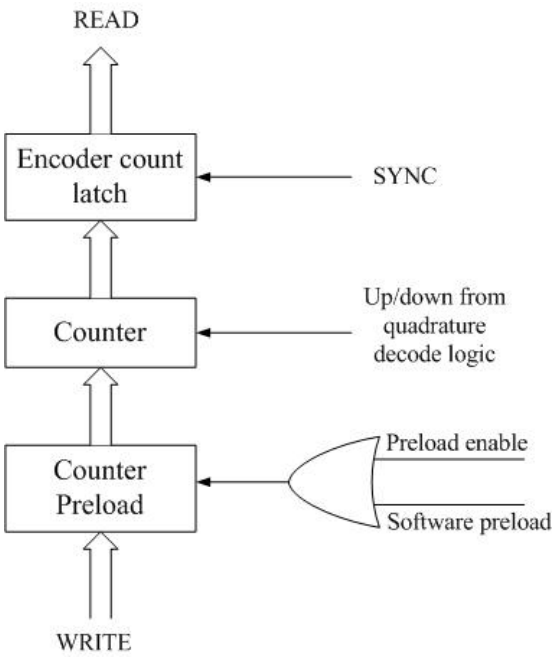

Figure 3.10: The block diagram of the encoder read and write interface

The next task of the Graphic Display thread is orientation recognition. It determines

whether the device is at the physical home configuration. The application software proceeds if a permission is issued by the orientation recognition task. For more detail regarding the orientation recognition system, please refer to section 3.4.1.

The third task of the Graphic Display thread is initial graphic rendering, which includes graphical representation of the haptic device, virtual environment and GUI as shown in figure 3.11.a, figure 3.11.b and figure 3.12 respectively.

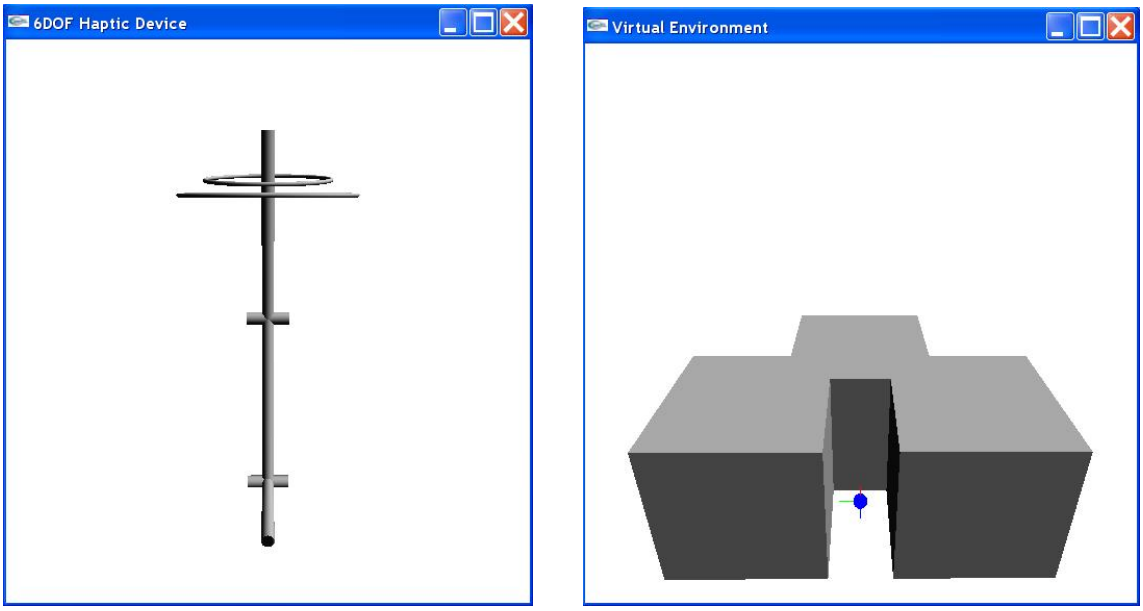

(a) (b)

Figure 3.11: The initial graphic rendering, (a): the graphical representation of the haptic device; (b): the virtual environment

The graphical representation of the haptic device reflects the starting configuration of the device. The GUI displays the key measurements and calculation results at the initial stage (e.g. the actuator joint angles, the orientation matrix of the mobile platform, the forward kinematic matrix, the actuator joint torques and the desired force at the stylus of the device). The blue cursor in the virtual environment represents the stylus of the device; the red, green and blue lines on the cursor represent the X, Y and Z axes of the end-effector; the three sides of the vertical notch which are located at the back, left side and right side of the stylus represent three virtual walls. Please note that the virtual environment shown in figure 3.11 is only one example. A number of different geometric shapes of the blue cursor and the virtual object are designed for different experiments. Please refer to section 3.7 for more

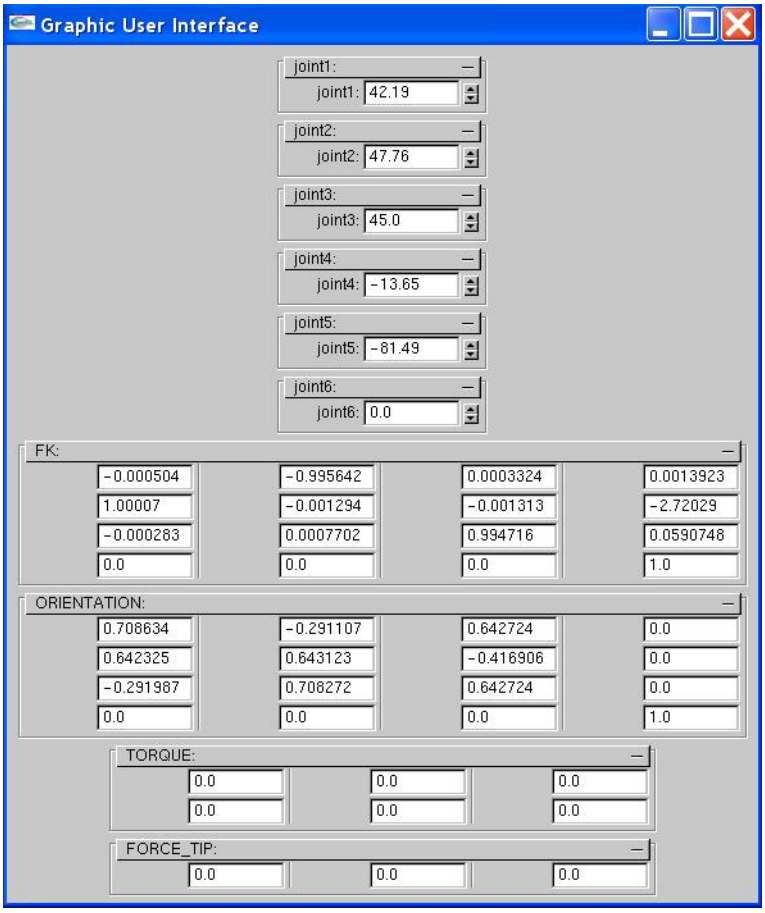

Figure 3.12: The initial graphic user interface

detail. These three graphic rendering units are updated once human operator manipulates the device. Specifically, the graphic representation of the haptic device is updated based on the encoder values and forward kinematic calculations. The blue cursor in the virtual environment is updated based on the forward kinematic calculations. For the GUI display, the actuator joint angles are updated based on encoder values; the orientation matrix of the mobile platform and the forward kinematic matrix are updated based on the forward kinematic calculations; the actuator joint torques are updated based on the force mapping calculations; the desired force at the stylus is updated based on the collision detection and simulation law.

3.3.3 Haptic Control Thread

With the permission from the orientation recognition task of the Graphic Display thread, the Haptic Control thread proceeds. It begins with the forward kinematic calculation task.

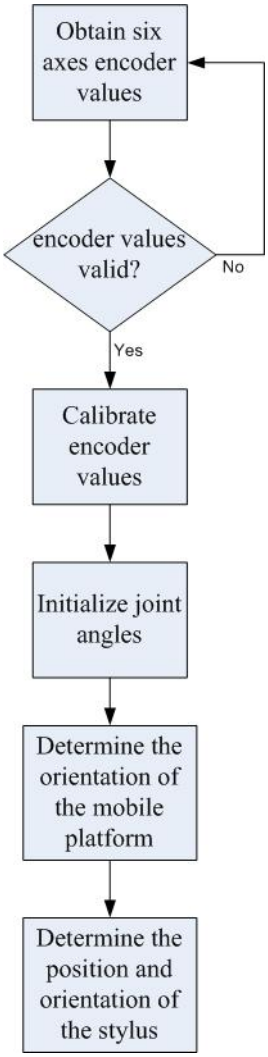

Figure 3.13: Forward kinematic calculation flowchart

Figure 3.13 depicts the process of forward kinematic calculation. At this stage, the six axes encoder registers are properly configured in Graphic Display thread as discussed in previous section. The encoder values can be obtained by calling the register function

($mcEncReadN()$) of both MC4000 boards. After the validation process, calibration process is executed to convert the encoder values to joint angles. The calibration process consists of two steps. Firstly, convert the decoder count value into degree of rotation of the motor shaft. As discussed in section 3.2.2, the quadrature decoder has 2000 CPR. Thus, one degree of rotation corresponds to 360/2000. Secondly, convert the degree of rotation of the motor shaft into actual joint angle. Due to the mechanical design of the haptic device, motor shaft is routed with the corresponding joint pulley by ultra high strength fiber wire. Therefore, the actual joint angle equals to the rotation of the motor shaft multiply by the ratio between the diameter of joint pulley and motor shaft. Equation 3.1 summaries the conversion.

$$Joint\_angle = \frac{360}{500 * 4} \frac{\varnothing motor\_shaft}{\varnothing joint\_pulley} \tag{3.1}$$

Having completed the conversion process, the six joint angles need to be initialized to accurately reflect the starting configuration of the haptic device. The initial values of the six joint angles are summarized in table 3.3. For the detail on the initial joint angle values, please refer to section 3.4.1. Next, the six joint angles are utilized to determine the orientation of the mobile platform, the position and orientation of stylus.

After the completion of the forward kinematic calculation, the data (e.g. joint angles, orientation matrix of the mobile platform, the forward kinematic matrix) is shared by the Graphic Display thread to update the graphical representation of the haptic device and the virtual environment.

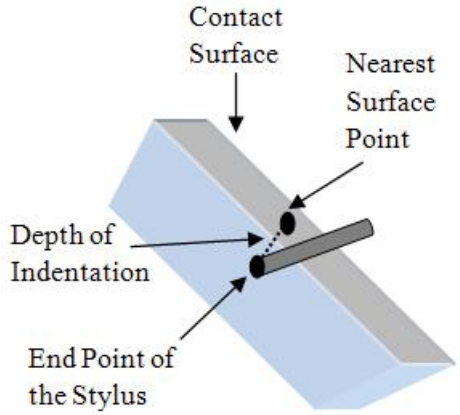

Figure 3.14: Point-based haptic interaction

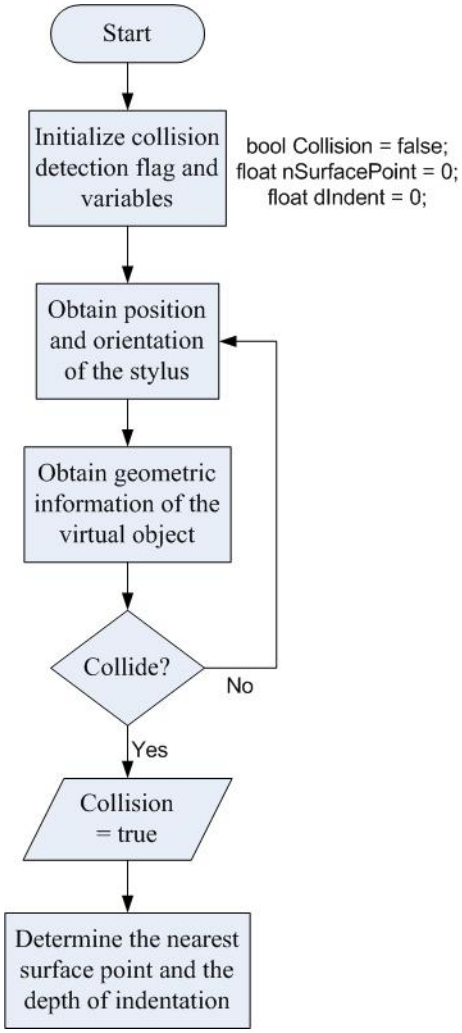

Figure 3.15: Collision detection algorithm

The next task of the Haptic Control thread is collision detection, which checks if the stylus of the device collides with the virtual object and returns collision information to the mechanics-based interaction task. Over the past decade, many researchers have studied different haptic rendering techniques to render 3D objects. The representation of 3D objects can be either surface-based [36] or volume-based [37] for the purposes of haptic rendering. The surface models are based on parametric or polygonal representations, while the volume models are based on voxels. The surface model is implemented in the proposed application software. An alternative way of distinguishing the existing haptic rendering techniques is

based on the type of haptic interaction: ray-based [38] or point-based [39]. In ray-based haptic interactions, the generic probe of the haptic device is modeled as a finite ray whose orientation is taken into account, and the collisions are checked between the ray and the objects. Point-based haptic interactions only consider the end point of the stylus interacts with objects. The stylus may penetrate into the virtual object after collision because the virtual surfaces have finite stiffness. The point-based collision detection algorithm checks if the stylus of the haptic device collides with the virtual object while the user moves the stylus. If the collision occurs, the depth of indentation is calculated as the distance between the current position of the stylus and a surface point, such as the nearest surface point. Figure 3.14 describes the concept of point-based haptic interaction. Figure 3.15 describes the point-based algorithm used in the application software. The algorithm begins with initializing the collision detection flag and two variables (the nearest surface point and the depth of indentation). Then, it obtains the position and orientation information of the stylus from the forward kinematic calculation task and latches the geometric information of the virtual object from Graphic Display thread. Comparison between the aforementioned information is performed to determine whether the stylus collides with the virtual object. If collision occurs, the collision detection flag is set true. The calculation of nearest surface point and the depth of indentation is then executed.

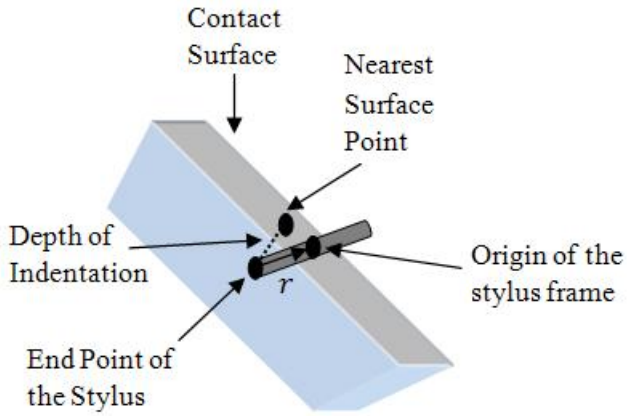

Figure 3.16: Torque calculation in point-base haptic interaction

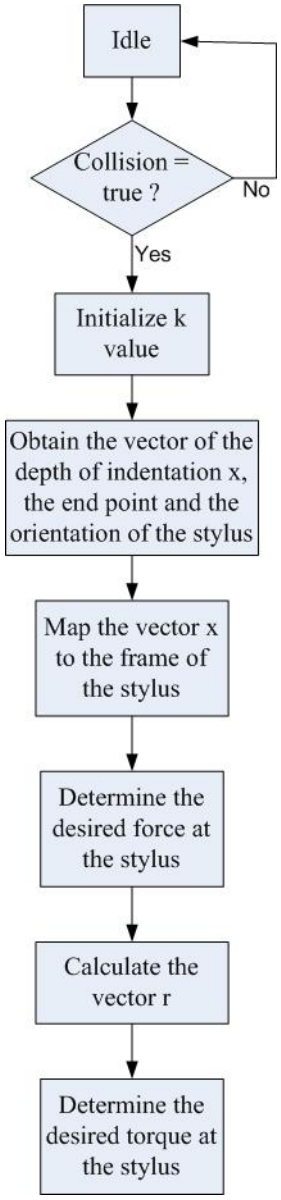

Figure 3.17: The flowchart of mechanics of interaction task

After the completion of the collision detection task, the mechanics of interaction task proceeds. This task determines the desired force/torque at the stylus of the haptic device based on the nearest surface point and the depth of indentation. The desired force at the stylus $\vec{F}_d$ is calculated using the spring model, $\vec{F}_d = k\vec{x}_d$, where k is the stiffness of

the virtual object, $\vec{x_d}$ is the depth of indentation mapped to stylus frame. The desired torque/moment at the stylus $\vec{M_d}$ is determined based on $\vec{F_d}$, $\vec{M_d} = \vec{r} \times \vec{F_d}$, where $\vec{r}$ is the position vector pointing from the end point of the stylus to the origin of the stylus (Figure 3.16). Over the past decade, extensive research has been conducted to render rigid object (high stiffness) [40], [41]. In the optimal case scenario, the haptic interface should be able to render absolute rigid object with infinite stiffness. However, it is not possible in real world because of mechanical and electrical limitations of the haptic interface (e.g. the mechanical structure of the haptic device, the maximum torque of the motor, the latency issue in the haptic loop, etc.) [35]. Methods to render higher stiffness object without sacrificing the stability has been studied in later chapter of this thesis work. The values of k various in different experiments. Please refer to the Section 3.7 and Chapter 4 for detail discussion. Figure 3.17 depicts the flowchart of the mechanics of interaction task. The task proceeds when the collision detection flag becomes true. The value of k is then initialized. After that, it obtains the depth of indentation $\vec{x}$ and the position of the end point of the stylus from the collision detection task, and the orientation matrix of stylus frame from the forward kinematic calculation task. The depth of indentation $\vec{x}$ is then mapped to the stylus frame and resulted in $\vec{x_d}$. Lastly, the desired force $\vec{F_d}$ at the stylus is determined based on the equation $\vec{F_d} = k\vec{x_d}$. The desired torque is then calculated based on the equation $\vec{M_d} = \vec{r} \times \vec{F_d}$.

The last task of the Haptic Control thread is force mapping. It determines the desired actuator joint torque based on the desired force/torque at the stylus using the force model established in Chapter 2.6. Figure 3.18 describes the flowchart of the force mapping task. It starts with obtaining desired force/torque vector at the stylus from mechanics of interaction task. The actuator joint torques of the serial mechanism (joint 6, 5 and 4) and the moment vector at the mobile platform are then determined based on the force model of the serial mechanism established in Chapter 2.7. Next, it calculates the Jacobian matrix of the spherical parallel mechanism according to Chapter 2.6. Then, the actuator joint torques of the spherical parallel mechanism (joint 1, 2 and 3) are determined giving the moment vector at the mobile platform and the Jacobian matrix of the spherical parallel mechanism. Next, the actuator torques are converted to reference voltages based on the motor characteristics. The detail of the conversion is discussed in Section 3.4.2. Lastly, it supplies the reference voltages to the corresponding servo amplifiers by calling the register function $mcDACwrite()$.

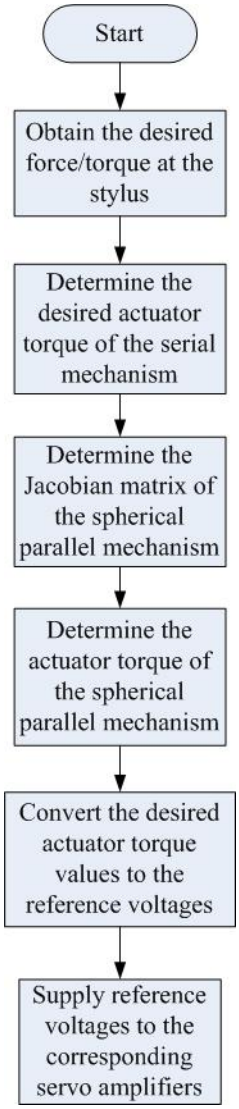

Figure 3.18: The flowchart of force mapping task

3.4 Calibrations

In this section, calibration work prior to the actual haptics experimentations is investigated. We first discuss the calibration of the physical home configuration. Then, we explain the relationship between the actuator torque and the voltage.

3.4.1 Calibration of the Physical Home Configuration

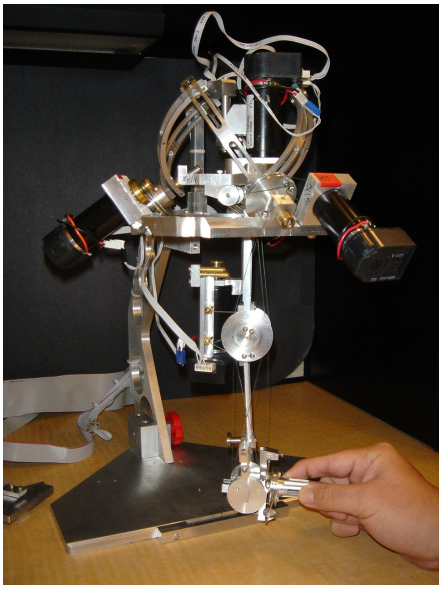

Figure 3.19: Kinematic home configuration

The physical home configuration is the starting configuration of manipulator and, in our case, is where the six quadrature decoders read zero from the encoders which are coupled with the joint actuators. If the physical home configuration and the kinematic home configuration are identical, the kinematic model can be directly used in the experimental study. However, assigning the physical home configuration to be the same as the the kinematic home configuration is not applicable due to the position of the end-effector based on the kinematic home configuration is away from the base of the haptic device as shown in Figure 3.19. Therefore, a physical home configuration of the haptic device needs to be defined.

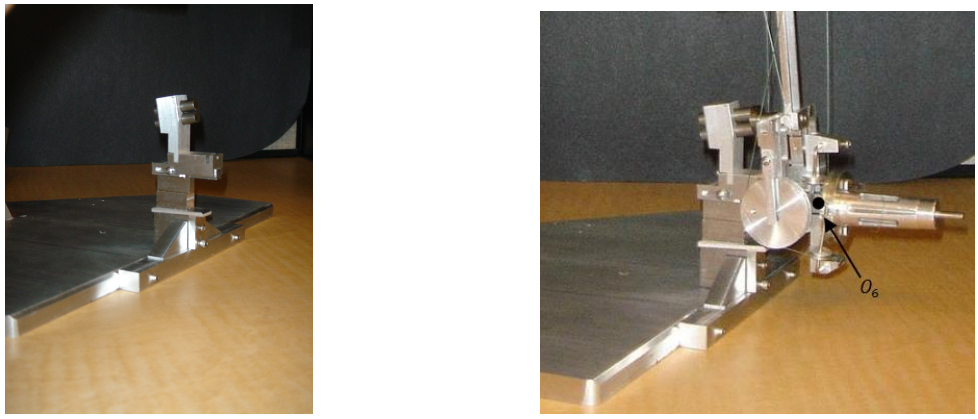

(a) (b)

Figure 3.20: The mechanical stand of the end-effector: (a): the structure of the stand; (b): the stand holding the end-effector and the location of the origin of the end-effector frame "O_6"

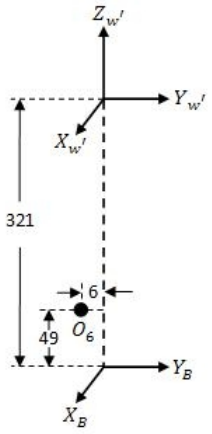

Figure 3.21: Calibration of the position of the end-effector of the physical home configuration (Unit is mm)

We propose two-step approach to define the physical home configuration. First, we define the position of the end-effector frame with respect to the hypothetical WCF $\{W'\}$. In order to define the position of the end-effector, an end-effector stand is designed and manufactured as shown in Figure 3.20.a. It can be mounted to the middle of the front edge of the base. The stand can be easily taken away when the end-effector is detached. Thus,

the stand will not interfere the workspace of the haptic device. Figure 3.20.b describes how the stand holds the end-effector of the haptic device and the position of the origin of the end-effector frame "O_6". Through the knowledge of the position of the origin of the end-effector frame in physical home configuration, the position vector of the end-effector frame with respect to the $\{W'\}$ frame, ${}^{W'}P_6$, can be measured. Referring the Figure 3.21, ${}^{W'}P_6$ is $\{0; -6; -272\}$.

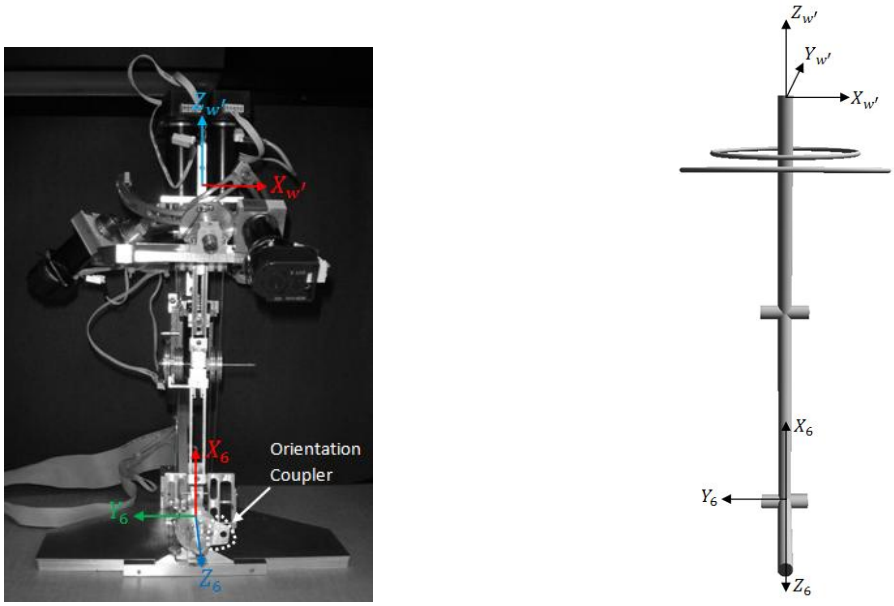

(a) (b)

Figure 3.22: Physical home configuration: (a): The front view of the actual device in physical home configuration; (b): The corresponding view in OpenGL

In addition to the position, the orientation of the end-effector at the physical home configuration needs to be defined. Figure 3.22.a shows the desired physical home configuration and the frame assignment of the end-effector while Figure 3.22.b exhibits the corresponding view from OpenGL. In order to determine whether the orientation of the end-effector aligns with the pre-defined orientation of the physical home configuration as depicted in Figure 3.22.a and 3.22.b. An orientation recognition system is designed and implemented which consists of an orientation coupler, a pair of infrared transmitter and receiver, voltage regulating and noise filtering circuitry, a housing for the infrared sensors and a digital interface. Specifically, a pair of infrared transmitter and receiver manufactured by Honeywell (SE5455

and SD5600) (see Appendix A) are selected to govern the orientation of the end-effector at the physical home configuration. In order to avoid the physical interference at the end-effector, we designed and manufactured a housing for the pair of infrared sensors as shown in Figure 3.23.b. It is to be clamped on the mechanical stand of the end-effector and the base on the haptic device and can be easily taken away as well.

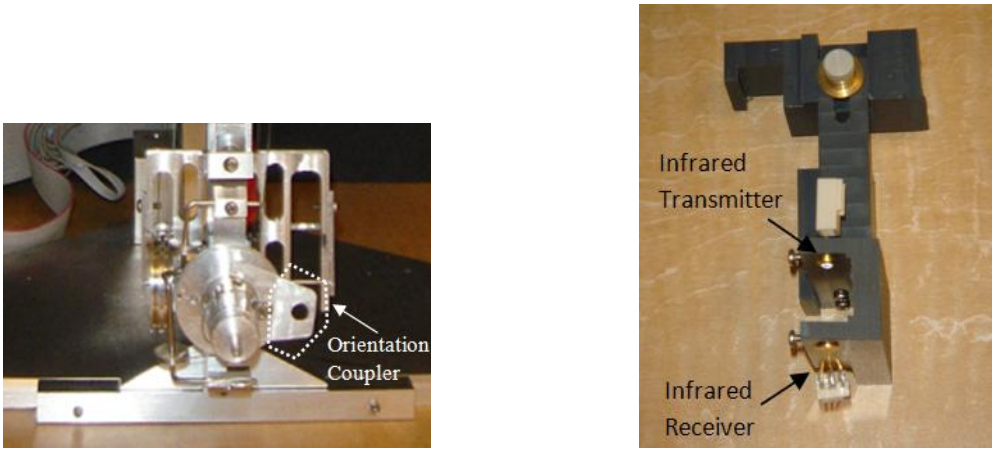

(a) (b)

Figure 3.23: Components of the orientation recognition system: (a): The orientation coupler; (b): The housing of the infrared transmitter and receiver

For the purpose of allowing the pair of infrared sensors to recognize the orientation of the end-effector at the physical home configuration, a mechanical orientation coupler is manufactured and mounted on the handle of the end-effector as shown in Figure 3.23.a. The orientation coupler ensures that the infrared light emitted by the infrared transmitter can be received by the infrared receiver if and only if the orientation of the end-effector aligns with the pre-defined orientation of the physical home configuration. Figure 3.24.a describes the concept of the orientation coupling while Figure 3.24.b shows a view when the housing of the infrared transmitter and receiver is clamped on the mechanical stand of the end-effector and the orientation of the end-effector aligns with the pre-defined orientation of the physical home configuration.

The voltage regulating and noise filtering circuitry of the orientation recognition system, as shown in Figure 3.25, is designed to have three functionalities. Firstly, it provides appropriate DC voltage to the infrared transmitter. In addition, it filters the noise of the

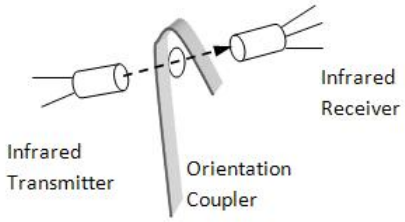

(a)

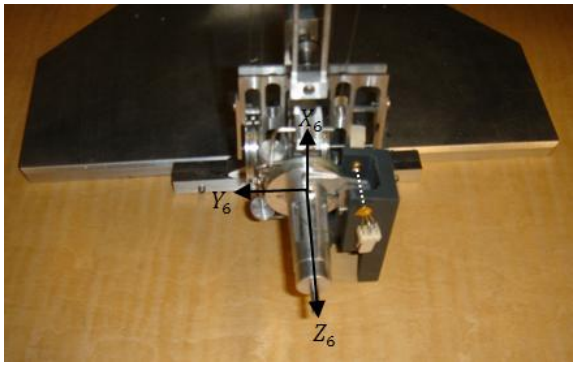

(b)

Figure 3.24: Orientation coupling: (a): Orientation coupling by using the mechanical orientation coupler and infrared sensors; (b): A view when the housing of the infrared transmitter and receiver is clamped on the mechanical stand of the end-effector

output signal from infrared receiver, which is to be supplied to the digital input of micro-controller. Lastly, it provides indication when the orientation of the end-effector aligns with the predefined orientation of the physical home configuration.

Components are selected to ensure that the voltage regulating and noise filtering circuitry is able to provide the aforementioned three functionalities. In particular, the infrared transmitter (SE-5455) has glass lensed cans providing a narrow beam angle which is particularly suitable for our application. The peak output wavelength of the infrared light emitted by the infrared emitter is 935nm. Since the maximum forward voltage of the infrared transmitter is 1.7V DC, a 3-terminal adjustable voltage regulator (LM317) is implemented to transfer the 5V DC voltage supplied by the micro-controller to 1.3V DC which is determined to maximize the power efficiency giving the fix distance between the infrared transmitter and receiver. The infrared receiver (SE-5600) is mechanically and spectrally matched with the infrared transmitter (SE-5455), in other words, the peak input wavelength is 935nm. The infrared receiver consists of a photodiode, amplifier, voltage regulator and Schmitt trigger. Thus, it is able to provide constant voltage output once the infrared light is received. The output of the infrared receiver has high signal to noise ratio and is TTL/CMOS compatible. It is connected in series with a light emitting diode (LED), a current limit resistor and one of the digital inputs of the micro-controller. Hence, as soon as the infrared light is received, the LED will on and the corresponding digital input bit of the micro-controller will be logic high. For the purpose of stabilizing the power supply line of the infrared receiver, a $0.1\mu V$

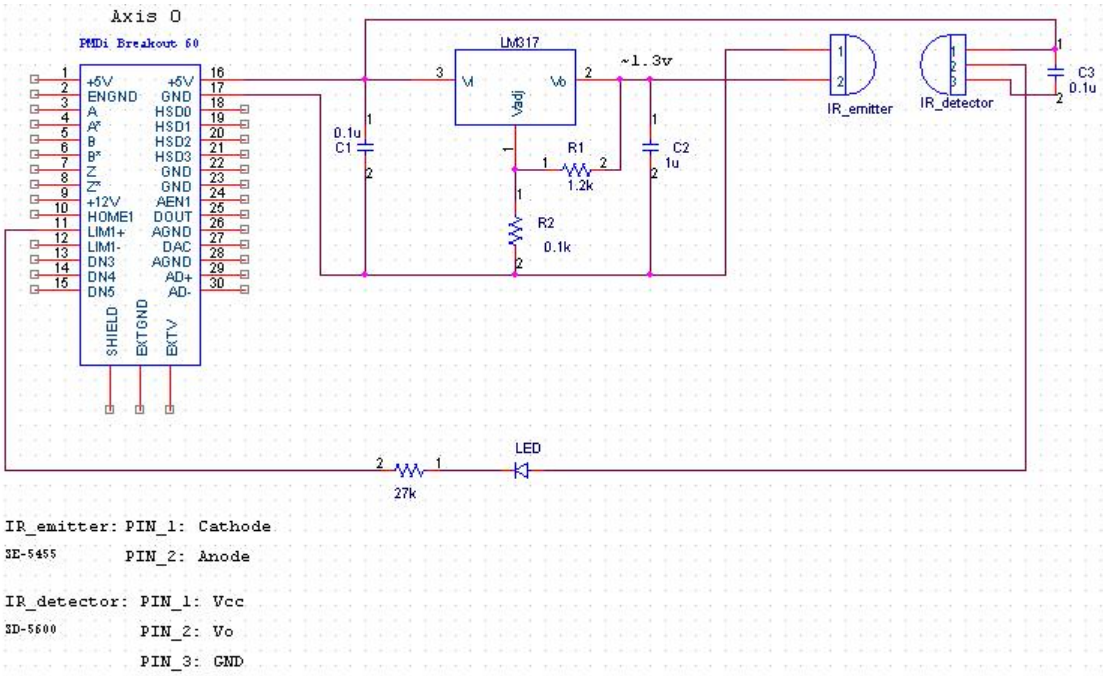

Figure 3.25: Orientation recognition system

capacitor is connected between Vcc and GND pins of the infrared receiver.

So far, the position of the end-effector at the physical home configuration have been determined and the desired orientation of the end-effector have been monitored. The analytical expression of the orientation of the end-effector at the physical home configuration can be determined by geometric mapping from $\{W^{'}\}$ frame to the frame of end-effector as shown in equation (3.2). The resulting transformation matrix is shown in equation (3.3).

$$ {}^{W'}_{6}R = \begin{bmatrix} X_6 \cdot X_{W'} & Y_6 \cdot X_{W'} & Z_6 \cdot X_{W'} \\ X_6 \cdot Y_{W'} & Y_6 \cdot Y_{W'} & Z_6 \cdot Y_{W'} \\ X_6 \cdot Z_{W'} & Y_6 \cdot Z_{W'} & Z_6 \cdot Z_{W'} \end{bmatrix} \tag{3.2} $$

$$ {}^{W'}_{6}T = \begin{bmatrix} 0 & -1 & 0 & 0 \\ 0 & 0 & -1 & -6 \\ 1 & 0 & 0 & -272 \\ 0 & 0 & 0 & 1 \end{bmatrix} \tag{3.3} $$

Having obtain the position and orientation of the end-effector of the physical home

configuration, we utilize the inverse kinematic model to determine corresponding six actuator joint angles. Table 3.3 summaries the six actuator joint angles of the physical home configuration.

Table 3.3: Summary of the six actuator joint angles of the physical home configuration

θ_1	θ_2	θ_3	θ_4	θ_5	θ_6
42.19°	47.76°	45°	-13.65°	-81.49°	0°

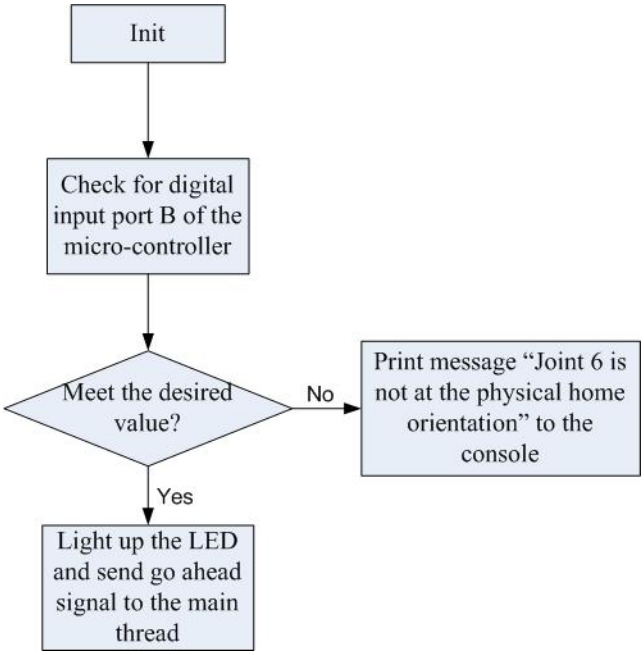

Figure 3.26: The flowchart of the interrupt service routine that checks for the orientation of the end-effector

Figure 3.26 describes the software process of checking the orientation of the end-effector at home configuration. This process serves as an interrupt service routine of the Graphic Display thread. This interrupt takes place the beginning stage of experimentations to ensure that the haptic device is at the physical home configuration.

3.4.2 Motor Characteristics

As discussed in Section 3.2.1, six Maxon RE 25mm DC motors are used in this thesis. The data sheet of the motor specification is attached in Appendix A. Table 3.4 summaries the key characteristics of the motor which are used in torque calibrations.

Table 3.4: Key specifications of Maxon RE 25 Brushed DC motor

Motor Data	Value
Assigned power rating	20 W
Nominal voltage	24 V
No load speed	9660 rpm
Stall torque	240 mNm
No load current	37 mA
Starting current	10300 mA
Terminal resistance	2.32 Ohm
Torque constant	23.2 mNm/A

For a DC permanent magnet motor, the torque is inverse proportional to the speed. In contrast, the torque is proportional to the current induced through the motor [43]. Figure 3.27 depicts the relationship between the motor torque and the speed at the nominal voltage while Figure 3.28 shows the relationship between the motor torque and the current at the nominal voltage. Note that the starting current can be regarded as stall current because neither start nor stall condition has back Electro-Magnetic Field (EMF) [43]. Using this linear relationship, no matter what load is applied to the motor, we can estimate the speed of the motor shaft and the current induced through the motor. For example, suppose we use this motor at a load of 100 mNm, using the above plot, we can see that the motor will run at approximately 5600 rpm and it will draw about 4.5 A from the power supply.

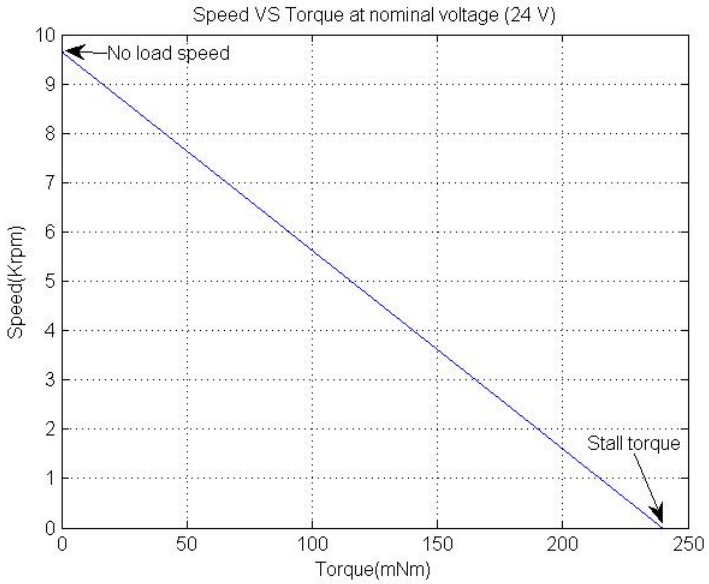

Figure 3.27: Speed VS Torque characteristic at nominal voltage

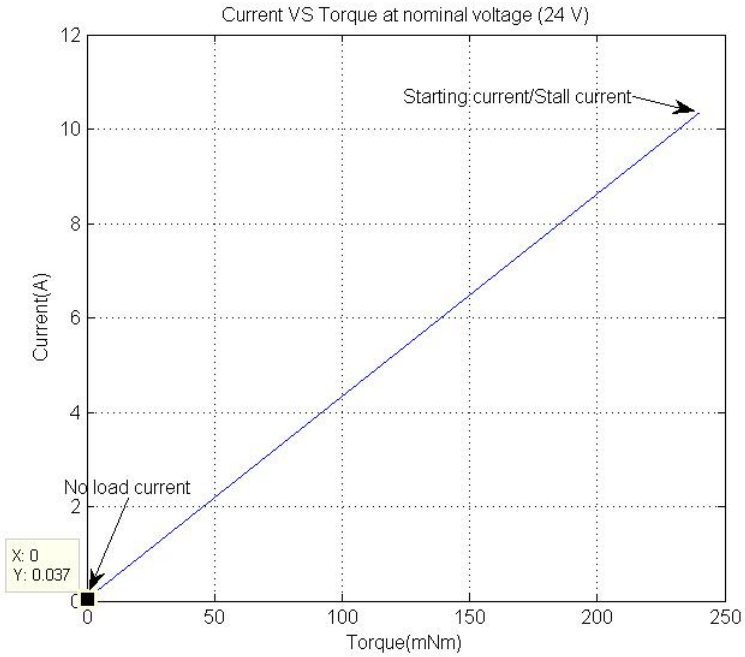

Figure 3.28: Current VS Torque characteristic at nominal voltage

In our application, for safety concern, the voltage supplied to the motor is limited to -10V to 10V. We can scale the plot accordingly to fit our operating range. We assume a permanent magnet motors such as Maxon RE 25 DC motor have the following characteristics: the no-load speed is directly proportional to the voltage, the slope of the speed/torque curve remains constant, and the current/torque curve does not change when the voltage varies [43]. For example, the no load speed at 5V can be determined by $9660rpm/24V * 5V$ which equals to 2013 rpm. Figure 3.29 exhibits the speed-torque characteristic of the motor at 1V, 2V, 3V, 4V and 5V. Figure 3.30 depicts the current-torque characteristic when torque range from 0 to 50mNm.

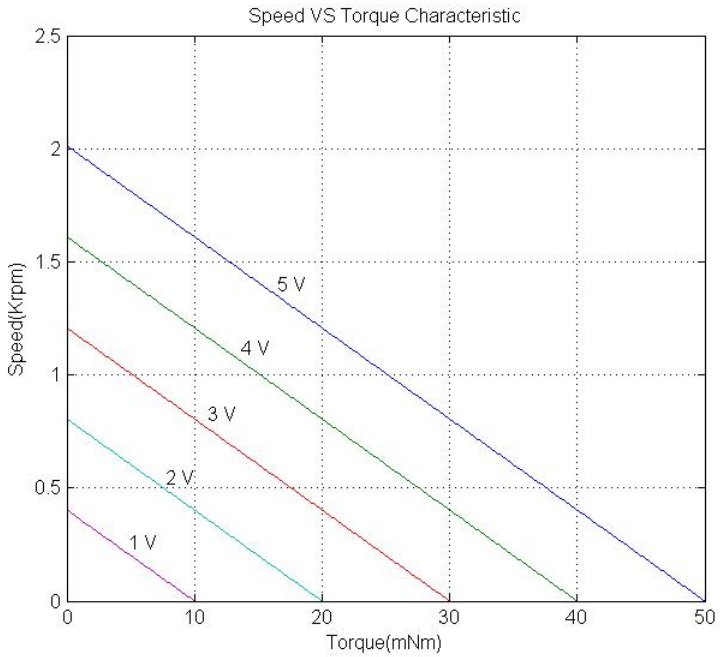

Figure 3.29: Speed VS Torque characteristic at 1V, 2V, 3V, 4V and 5V

The stall torque of the motor is the key characteristic for haptics application. Referring to Figure 3.29, one can observe that the stall torques at 1V, 2V, 3V, 4V and 5V are 10 mNm, 20 mNm, 30 mNm, 40 mNm and 50 mNm respectively. Referring to Figure 3.30, one can observe that the stall current at 1V, 2V, 3V, 4V and 5V are 0.43A, 0.86A, 1.29A, 1.72A, 2.15A. In stall condition, the armature of the motor appears in the circuit as a resistor. Therefore, the stall current and stall torque are directly proportional to the applied voltage.

Using the terminal resistance (2.32 Ohm) and torque constant (23.2 mNm/A), the conversion between the desired torque , the current and the terminal voltage can be determined. For example, if the desired torque is 40 mNm, the motor should draw approximately 1.72 A ($40mNm/23.2mNm/A = 1.72A$) from the power supply. The terminal voltage across the motor leads should be about 4V ($1.72A * 2.32Ohm = 4V$).

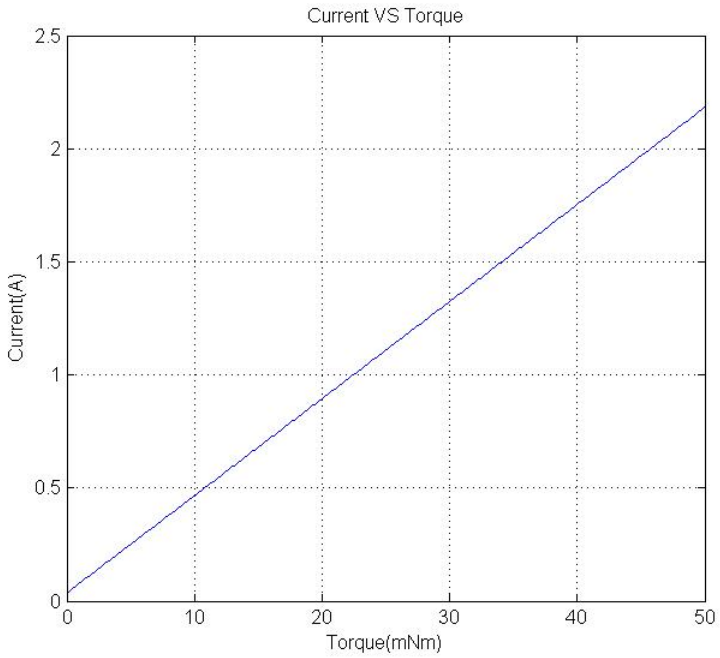

Figure 3.30: Current VS Torque characteristic when torque range from 0 to 50mNm

3.4.3 Precision

The ratio between the diameter of joint pulley ($\varnothing joint\_pulley$) and motor shaft ($\varnothing motor\_shaft$) is 0.23. According to equation 3.1, the resolution of joint angle is 0.04°. Substituting the 0.04° change of joint angles at physical home configuration into forward kinematic model, we notice that the minimum change of the position of the stylus occurs when there is 0.04° increase on θ_3. Table 3.6 illustrates the set of joint angles in this case. Equation (3.4) shows the transformation matrix. Comparing equation (3.3) with equation (3.4), we can see that the minimum change is along the Z axis of the stylus frame which is 0.02 mm. Overall, the rotational precision of the proposed haptic device is 0.04°; the linear precision of the

proposed haptic device is 0.02 mm.

Table 3.5: Summary of the six actuator joint angles

θ_1	θ_2	θ_3	θ_4	θ_5	θ_6
42.19°	47.76°	45.04°	−13.65°	−81.49°	0°

$$ {}^{W'}_{6}T = \begin{bmatrix} -0.14 & -0.99 & 0 & 0.35 \\ 0 & 0 & -1 & -5.91 \\ 0.99 & -0.14 & 0 & -272.02 \\ 0 & 0 & 0 & 1 \end{bmatrix} \tag{3.4} $$

3.5 Kinematic Correspondence

In this section, the forward and inverse kinematic models of the haptic device are examined through the kinematic correspondence system. In particular, the user moves the stylus of the haptic device along an arbitrary trajectory which starts from and terminates at the physical home position. While the user manipulates the stylus of the haptic device, the kinematic correspondence system collects the six individual joint angles, determines the position and orientation of the stylus based on the forward kinematic model, and renders the corresponding graphical representation of the haptic device in real time.

Comparing with the overall software sequence diagram (Figure 3.8), the software sequence diagram of the kinematic correspondence experiment (Figure 3.31) only has two threads (Haptic Control thread and Graphic Display thread) since there is no need for actual force/torque data collection. In addition, collision detection, mechanics of interaction and force mapping tasks of the Haptic Control thread are omitted because we only examine the kinematic correspondence characteristic of the haptic interface in this experiment.

Three sets of joint angles at 1^{st}, 1500^{th} and 2500^{th} sample are utilized to examine the forward kinematic model. After that, these forward kinematic solutions are utilized to examine the inverse kinematic model. Figure 3.32 records the six individual joint angles which are collected from the encoder in real time. Table 3.6 illustrates the six joint angles at the three selected samples (S_1 is recorded at the 1^{st} sample, S_2 is recorded at the 1500^{th} sample and S_3 is recorded at the 2500^{st} sample).

The three sets of joint angles are fed to the forward kinematic model to solve for the

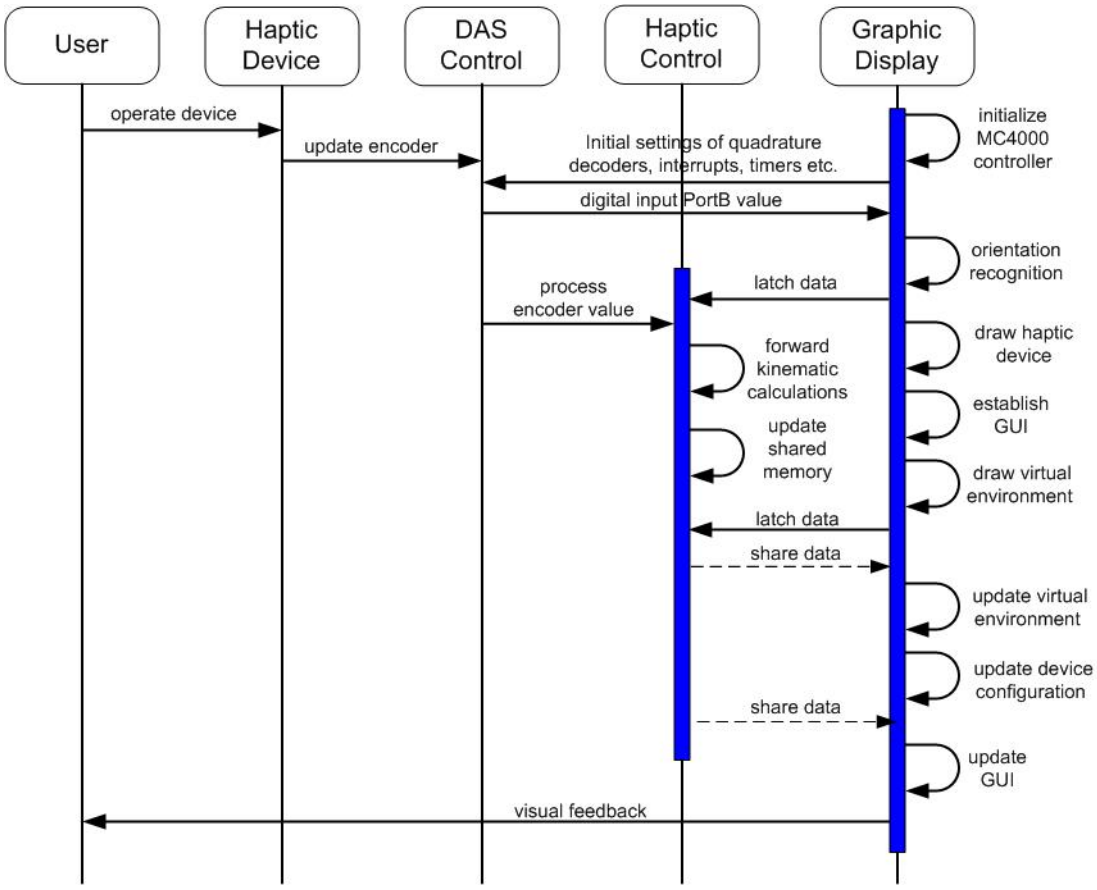

Figure 3.31: Software sequence diagram of kinematic correspondence experiment

position and orientation of the stylus at the corresponding selected sample. The resulting forward kinematic solutions are listed below. Please note that ${}^{W'}_{6}T_{S_i}(i = 1, 2, 3)$ represents the forward kinematic solution of the S_i sample.

$$ {}^{W'}_{6}T_{S_1} = \begin{bmatrix} 0 & -1 & 0 & 0.15 \\ -0.16 & 0 & -0.99 & -5.9 \\ 0.99 & 0 & -0.16 & -272.02 \\ 0 & 0 & 0 & 1 \end{bmatrix} $$

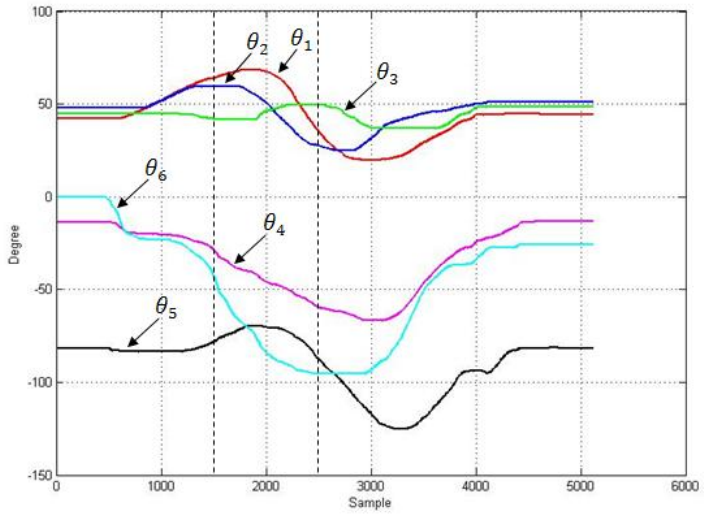

Figure 3.32: Six individual joint angles

Table 3.6: List of joint angles at the three selected samples (S_1 is recorded at the 1^{st} sample, S_2 is recorded at the 1500^{th} sample and S_3 is recorded at the 2500^{st} sample)

	θ_1	θ_2	θ_3	θ_4	θ_5	θ_6
S_1	42.19°	47.76°	45°	−13.65°	−81.49°	0°
S_2	64.14°	59.65°	42.03°	−28.74°	−78.23°	−42.37°
S_3	35.33°	27.64°	49.57°	−59.6°	−87.42°	−95.41°

$$ {}^{W'}_{6}T_{S_2} = \begin{bmatrix} 0.89 & -0.44 & -0.07 & -94.81 \\ 0.13 & 0.41 & -0.9 & -83.93 \\ 0.42 & 0.8 & 0.43 & -232.58 \\ 0 & 0 & 0 & 1 \end{bmatrix} $$

$$ {}^{W'}_{6}T_{S_3} = \begin{bmatrix} 0.96 & -0.17 & -0.2 & 75.62 \\ 0.08 & 0.9 & -0.41 & -136.44 \\ 0.25 & 0.38 & 0.89 & -178.28 \\ 0 & 0 & 0 & 1 \end{bmatrix} $$

Figure 3.33 records the position of the end-effector while Figure 3.34 records the trajectory of the end-effector in real time. These two figures are able to verify the position solution of

the forward kinematic model.

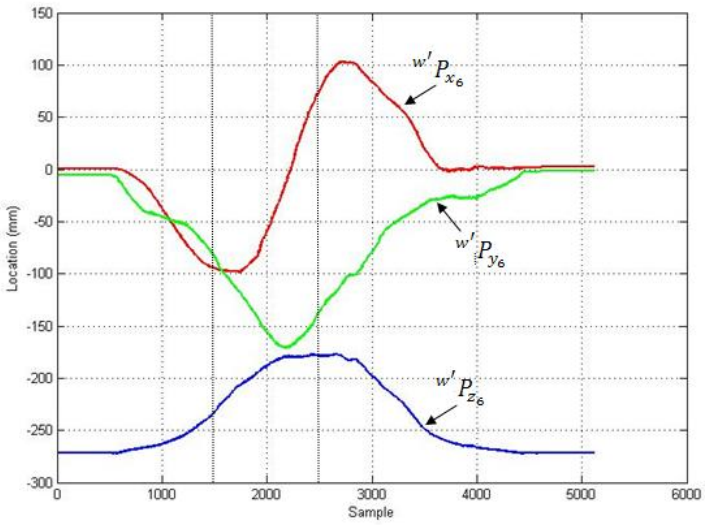

Figure 3.33: The position of the end-effector

In order to verify the orientation solution of the forward kinematic model and to visualize the physical change of the device along the trajectory, three graphic representations of the device are generated through OpenGL as depicted in Figure 3.35. These three graphic representations are overlapped by aligning the $\{W'\}$ frame. In addition, they are black, gray and light gray colored which correspond to device configuration at S_1, S_2 and S_3 respectively.

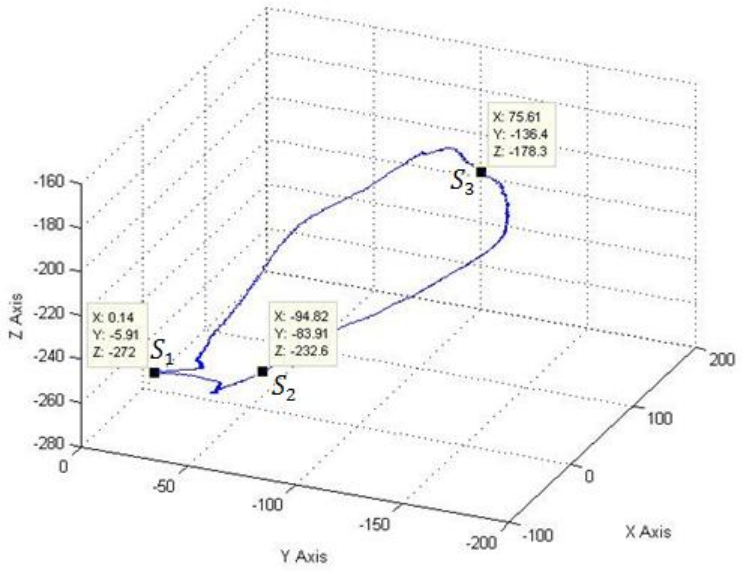

Figure 3.34: The trajectory of the stylus

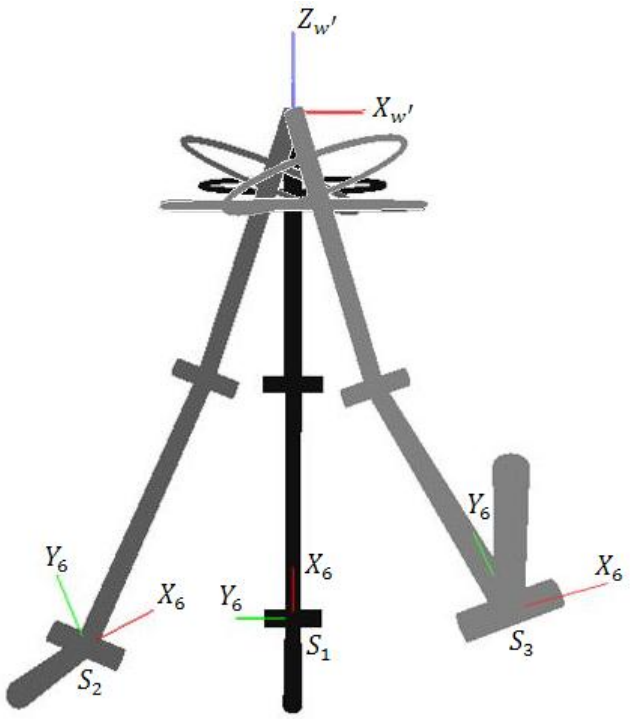

Figure 3.35: Device configurations generated by OpenGL

The above forward kinematic solutions are fed to the inverse kinematic model. Table 3.7 concludes the inverse kinematic solutions. Comparing the result with table 3.6, one is able to observe that the inverse kinematic result agrees with the forward kinematic result. Overall, the kinematic correspondence experiment results indicate that the proposed haptic interface has good kinematic correspondence given by the user and those applied to the virtual environment.

Table 3.7: The inverse kinematic solutions based on position and orientation of the end-effector at the selected samples

	θ_1	θ_2	θ_3	θ_4	θ_5	θ_6
S_1	42.19°	47.68°	45.09°	−13.88°	−81.43°	0°
S_2	64.13°	59.18°	42.13°	−29.81°	−77.82°	−42.37°
S_3	36.13°	27.34°	50.77°	−59.19°	−88.46°	−95.41°

3.6 Force Correspondence

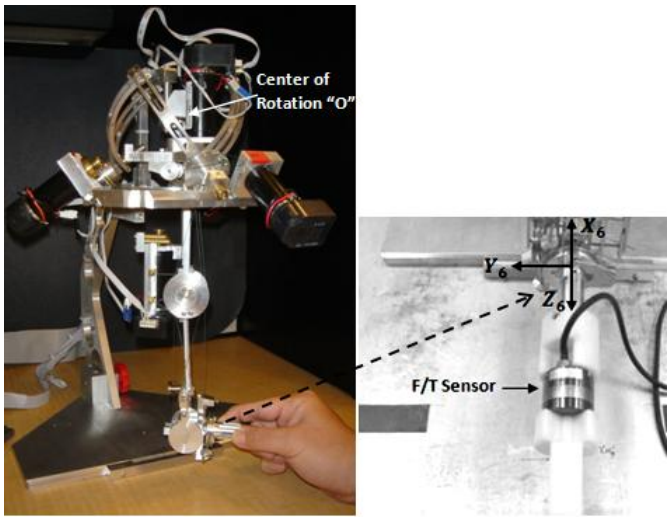

Figure 3.36: The haptic device with F/T sensor mounted at the stylus

The force correspondence experiment is aimed to verify the correspondence of the desired

force/torque at the stylus assigned by the virtual environment and the actual force/torque rendered at the stylus. Six experiments are designed, each of which takes the desired force or torque value at the stylus as input, determines the corresponding six actuator joint torques and renders the force feedback accordingly. Specifically, the first four experiments take the desired force magnitude of 1 N along $\pm Z_6$ axis and $\pm Y_6$ axis respectively. The last two experiments take the desired torque magnitude of 1 Nm along $\pm X_6$ axis restively. The actual force and torque results are measured by the F/T sensor which is mounted at the end-effector as shown in Figure 3.36.

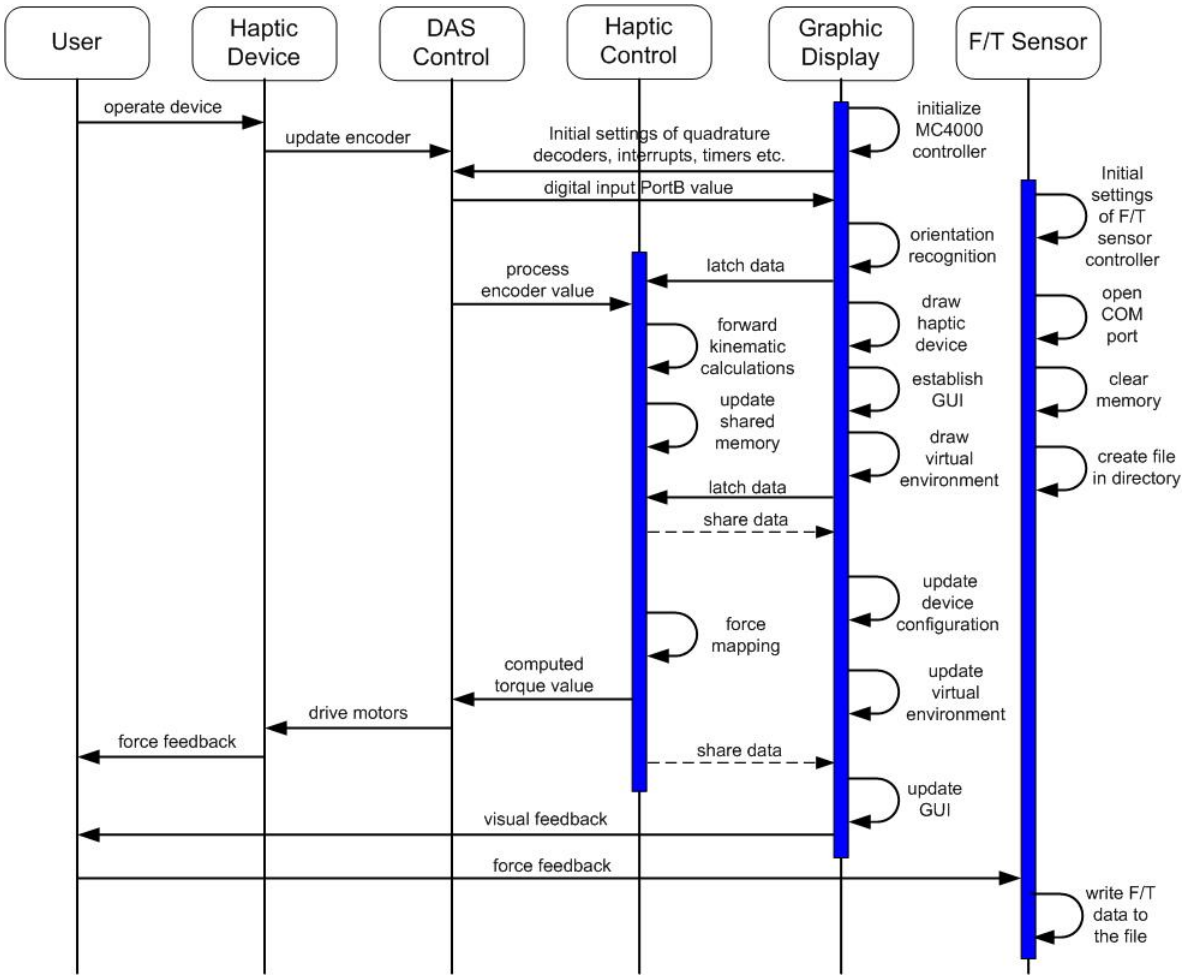

Figure 3.37: Software sequence diagram of force correspondence experiment

Comparing with the overall software sequence diagram (Figure 3.8), the Haptic Control thread of the software sequence diagram of the force correspondence experiment (Figure 3.37) does not require collision detection and mechanics of interaction tasks. The reason is that, for the case of force correspondence experiment, the desired force/torque values at the stylus are predefined as previously mentioned.

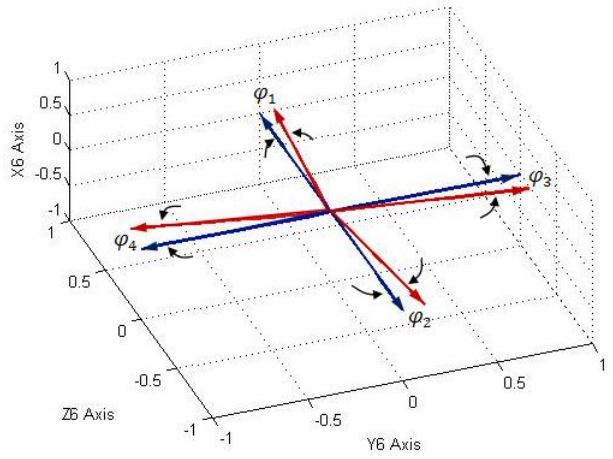

Figure 3.38: Directional errors of the actual force vectors (in red) with respect to the desired force vectors (in blue)

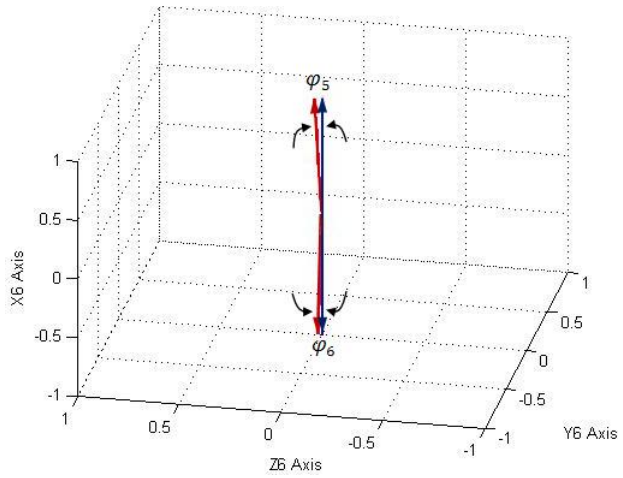

Figure 3.39: Directional errors of the actual torque vectors (in red) with respect to the desired torque vectors (in blue)

Figure 3.38 and Figure 3.39 show the desired force or torque vectors and the normalized actual force or torque vectors of the six experiments. The vectors of red color are the normalized actual force or torque vectors while the vectors of blue color are the desired force or torque vectors. The direction errors between the desired and actual force or torque vectors are denoted by $\varphi_1, \ldots, \varphi_6$. The values of these angles are $4.29°, 6.91°, 7.85°, 11.43°, 2.11°$ and $1.32°$ respectively. The relatively significant error occurs when the desired force vectors are along positive or negative Y_6 axis. This can be attributed to the posture of the user holding the force sensor.

3.7 Interaction with Virtual Environment

Having established the kinematic and force correspondence characteristics of the haptic interface, we present some preliminary results when the haptic device interacts with virtual environments. We firstly demonstrate the force feedback along the Y_6 and Z_6 axes. We then present the torque display along the X_6, Y_6 and Z_6 axes.

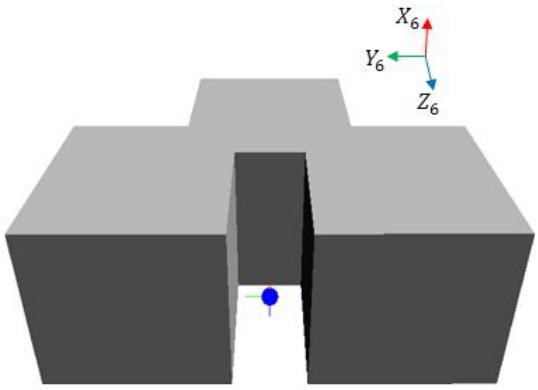

Figure 3.40: The virtual environment of the first experiment

Figure 3.40 exhibits the virtual environment of this experiment, the blue cursor represents the stylus; the red, green and blue lines on the cursor represent the X, Y and Z axes of the end-effector; the three sides of the vertical notch which are located at the back, left side and right side of the end-effector, represent three virtual walls. A spring model with the stiffness coefficient k of 20 N/m is applied to model the virtual wall. Since we have not yet included any stability enhancement methods into the haptic interface, the stiffness

coefficient is selected at relatively low level. The overall software sequence diagram (Figure 3.8) describes the general structure of the application software implemented in the experiments of this section. In this experiment, as depicted in Figure 3.41, the user moves the stylus of the haptic device starting from the physical home position and then makes contact with the virtual walls located at the left side, the right side and back side sequentially. The desired force is computed based on the collision detection and mechanics-base interaction. It is recorded at 1 KHz. The actual force exerted at the stylus is measured by the F/T force sensor. It is collected at 40 Hz. Figure 3.42 shows the desired force along the Y_6 axis (upper portion) and along the Z_6 axis (lower portion), while Figure 3.43 depicts the actual force along the Y_6 axis (upper portion) and along the Z_6 axis (lower portion).

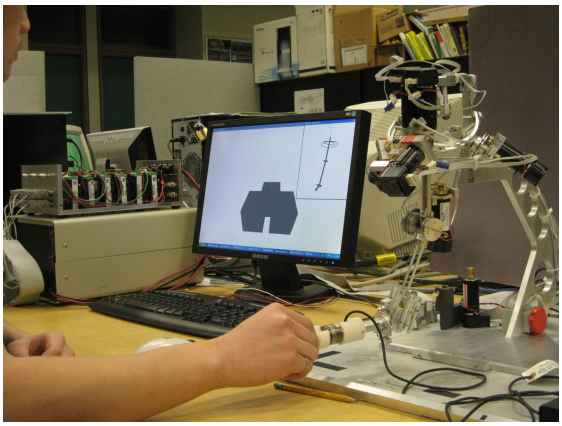

Figure 3.41: User interact with virtual environment

The results reflect the three contact events. For example, the first contact event takes place at the left side virtual wall at between 7.62 second and 8.98 second, and the expected reaction force is along the negative Y_6 direction. This can be observed between A (7626^{th} sample) and B (8985^{th} sample) of the desired force plot along Y_6 axis (sampling rate is 1 KHz) in Figure 3.42 and between $A^{'}$ (310^{th} sample) and $B^{'}$ (386^{th} sample) of the actual force plot along Y_6 axis (sampling rate is 40 Hz) in Figure 3.43. The 0.15 second time delay of the actual force display is noticed according to the time difference between A and $A^{'}$. This can be attributed to the delays from varies different components in the haptic control loop (i.e. quantization delay and amplifier delay) and the serial communication with F/T controller.

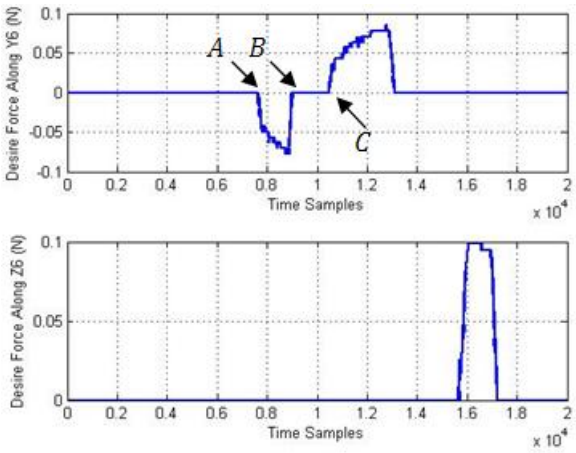

Figure 3.42: The desired force along Y_6 axis (upper portion) and Z_6 axis (lower portion)

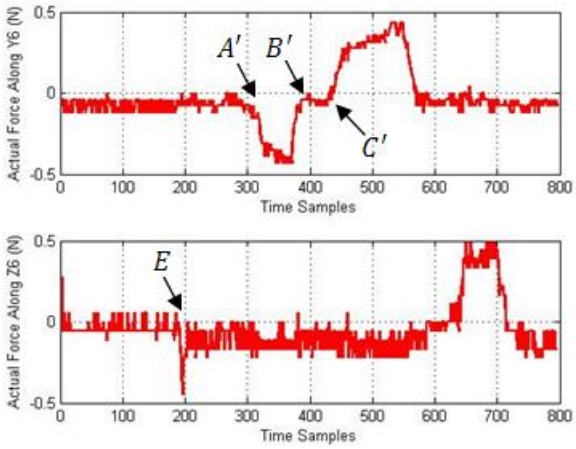

Figure 3.43: The actual force along Y_6 axis (upper portion) and Z_6 axis (lower portion)

The magnitude of the actual force display is proportional to the amplifier gain (which is assigned to be 5 in this experiment). This can be observed by comparing the Y axis scale of the desired and actual force plots in Figure 3.42 and Figure 3.43. The user can be active during the manipulation, which affects the results of the actual force. For example, a significant jitter of the force along Z_6 axis occurs at 5 second which corresponds to E (200^{th} sample) of the actual force plot along Z_6 axis in Figure 3.43. This is caused by the user dragging the stylus away from the rest position. In addition, depending on the way

user grasping the stylus, the response of the actual force exerted at the user's hand to the abrupt change of the desired force can be relatively slow. For example, at 10.5 second, the stylus makes initial contact with the right side virtual wall (the second contact event), which corresponds to C (1048^{th} sample) of the desired force plot along Y_6 axis in Figure 3.42 and C'(435^{th} sample) of the actual force plot along Y_6 axis in Figure 3.43, the slope of the actual force plot is less steep which indicates longer response time.

The next experiment is aim to demonstrate the torque display along X_6 axis. Figure 3.47.a depicts the start of the interaction where the stylus (the blue cylinder) is sitting at the rest position, while Figure 3.47.b describes the moment when the stylus makes contact with the virtual cube. The coordinate frame located at the upper right corner of Figure 3.47.a and 3.47.b represents the orientation of the stylus at the rest position and at the moment of initial contact respectively. During the entire process, the stylus is made contact twice with the virtual cube with the same fashion as shown in Figure 3.47.b. F_c represents the contact force when contact takes place. Based on the orientation of the stylus, the torque along the positive X_6 axis should be the dominant component of the overall force/torque feedback. In addition, there should be force along positive Z_6 axis and negative Y_6 axis.

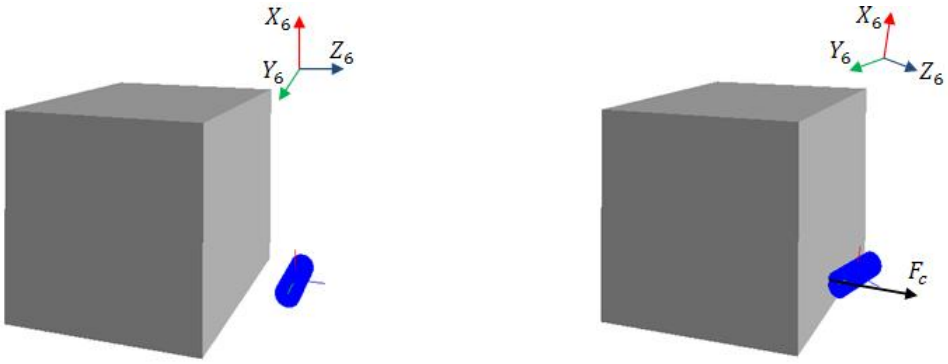

(a) (b)

Figure 3.44: The virtual environment of the second experiment, (a): initial condition; (b): stylus makes contact with the virtual cube

Figure 3.45 presents the desired torque (computed based on the collision detection and mechanics-base interaction) along X_6 axis, while Figure 3.46 exhibits the actual torque (measured by the F/T sensor) along X_6 axis (the upper plot), the actual force along Y_6 axis (the middle plot) and the actual force along Z_6 axis (the lower plot). The results reflect the two contact events. For example, the first contact event takes place at between 10.15

second and 15.65 second. It can be observed between G_1 (1015^{th} sample) and H_1(1565^{th} sample) in Figure 3.45, and between G_2 (465^{th} sample) and H_2(717^{th} sample) of the plot of actual torque along X_6 axis in Figure 3.46. In addition, this contact event can be observed between G_3 (465^{th} sample) and H_3 (717^{th} sample) of the plot of actual force along Y_6 axis and between G_4 (465^{th} sample) and H_4 (717^{th} sample) of the plot of actual force along Z_6 axis in Figure 3.46. As expected, the results indicate that there are forces along negative Y_6 axis and positive Z_6 axis.

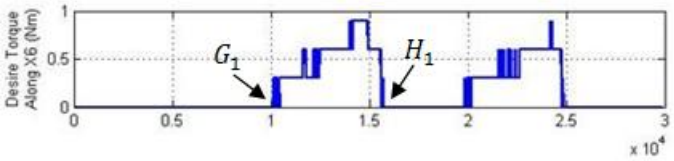

Figure 3.45: The desired torque along X_6 axis

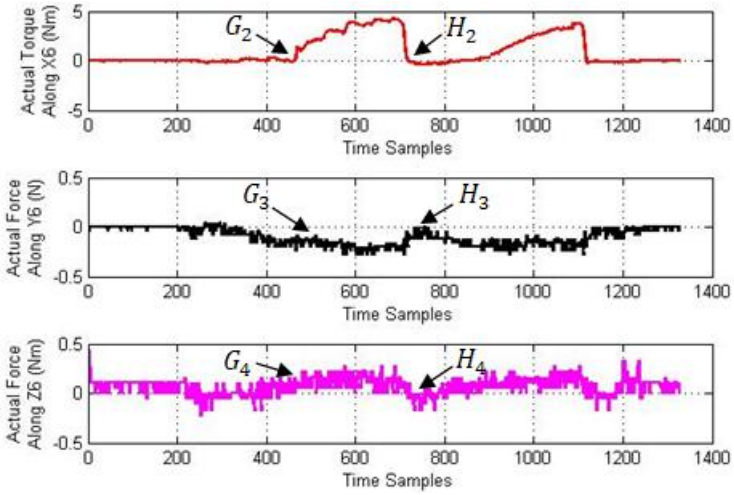

Figure 3.46: The actual torque along X_6 axis (in red), along Y_6 axis (in black) and along Z_6 axis (in magenta)

The third experiment is aim to demonstrate the torque display along Y_6 axis. Figure 3.47.a depicts the start of the interaction where the stylus (the blue cylinder) is sitting at the rest position, while Figure 3.47.b describes the moment when the stylus makes contact with the upper surface of the virtual cube. The coordinate frame located at the upper right corner of Figure 3.47.a and 3.47.b represents the orientation of the stylus at the rest

position and at the moment of initial contact respectively. During the entire process, the stylus is made contact with the upper surface twice with the same fashion as shown in Figure 3.47.b. F_c represents the contact force when contact takes place. Based on the orientation of the stylus, the torque along the positive Y_6 axis should be the dominant component of the overall force/torque feedback. In addition, there should be comparatively larger force along positive X_6 axis than negative Z_6 axis.

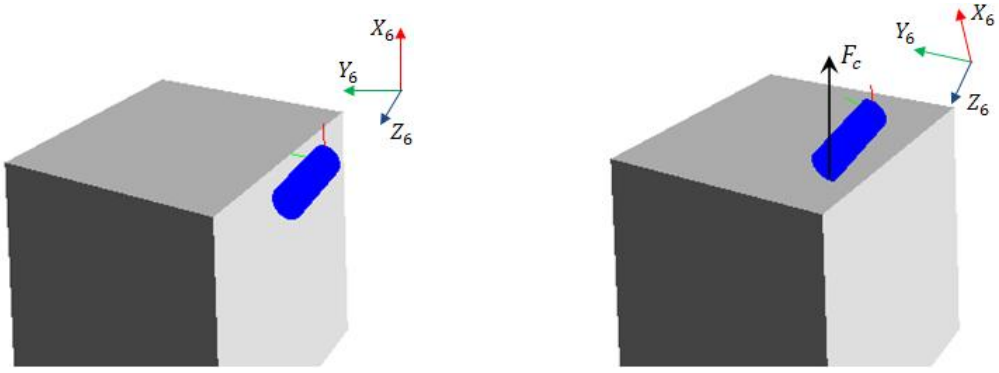

(a) (b)

Figure 3.47: The virtual environment of the third experiment, (a): initial condition; (b): stylus makes contact with the virtual cube

Figure 3.48 presents the desired torque along Y_6 axis, while Figure 3.49 exhibits the actual torque along Y_6 axis (the upper plot), the actual force along X_6 axis (the middle plot) and the actual force along Z_6 axis (the lower plot). The results reflect the two contact events. For example, the first contact event takes place at between 6.98 second and 9.35 second. It can be observed between A_1 (6980^{th} sample) and B_1(9350^{th} sample) in Figure 3.48, and between A_2 (287^{th} sample) and B_2(434^{th} sample) of the plot of actual torque along Y_6 axis in Figure 3.49. In addition, this contact event can be observed between A_3 (287^{th} sample) and B_3 (434^{th} sample) of the plot of actual force along X_6 axis and between A_4 (287^{th} sample) and B_4 (434^{th} sample) of the plot of actual force along Z_6 axis in Figure 3.49. The magnitude of the force along positive X_6 axis (the difference between A_3 and C_3) is larger than that of the force along negative Z_6 axis (the difference between A_4 and C_4) as shown in Figure 3.49, which also agree with the expectation. The negative value of the force along X_6 axis before first contact event (between D_3 and A_3) and after the second contact event (between E_3 and F_3) is resulted from the mass of the force sensor and the force sensor fixture which is acting along the negative X_6 axis.

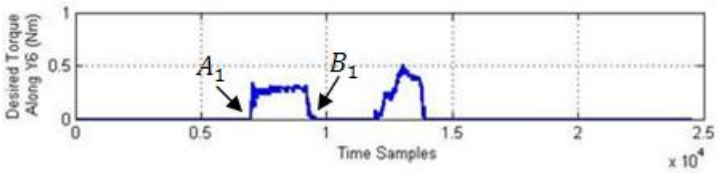

Figure 3.48: The desired torque along Y_6 axis

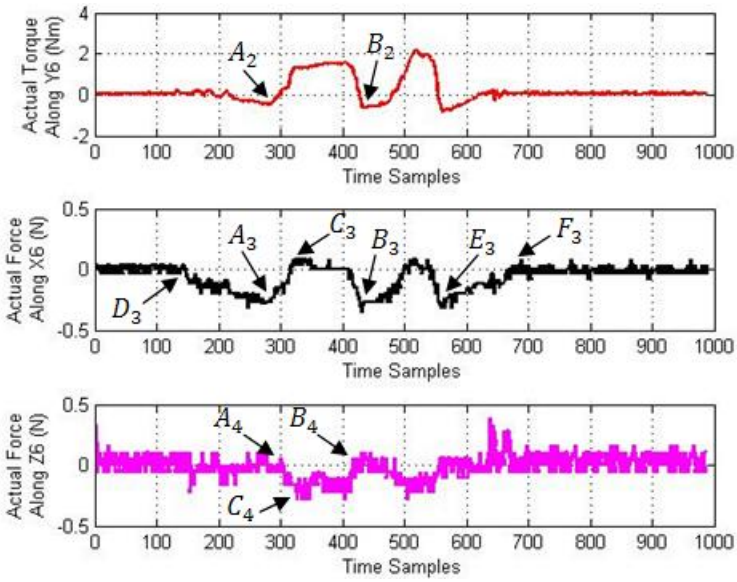

Figure 3.49: The actual torque along Y_6 axis (in red), along X_6 axis (in black) and along Z_6 axis (in magenta)

The fourth experiment is aim to demonstrate the torque display along Z_6 axis. Figure 3.50.a depicts the start condition of the interaction where the stylus (the blue cylinder) is sitting at the rest position, while Figure 3.50.b describes the moment when the stylus makes contact with the upper surface of the virtual cube. During the entire process, the stylus is made contact with the upper surface twice. The first collision even occurs when user rotates the stylus along counter clock wise direction of Z_6 until colliding with the upper surface of the virtual cube as depicted in Figure 3.50.b. In addition, there should be small positive force along X_6 axis and small negative force along Y_6 axis. The second collision event occurs when user rotates the stylus along clock wise direction of Z_6 until colliding with the upper surface of the virtual cube. F_c represents the contact force when collision takes place. Based on the orientation of the stylus, for the first collision event, the torque

along the negative Z_6 axis should be the dominant component of the overall force/torque feedback. In addition, there should be small amount of force rendered along the positive X_6 and the negative Y_6 axes. For the second collision event, the torque along the positive Z_6 axis should be the dominant component of the overall force/torque feedback. In addition, there should be small positive force along both X_6 and Y_6 axes.

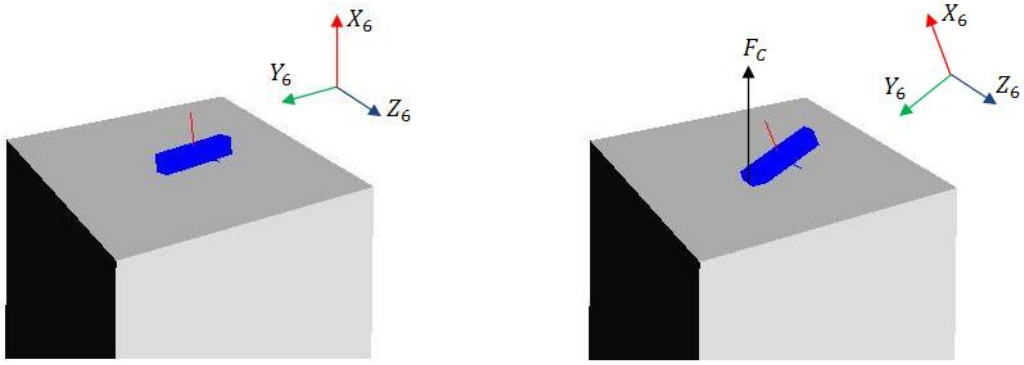

(a) (b)

Figure 3.50: The virtual environment of the fourth experiment, (a): initial condition; (b): stylus makes contact with the virtual cube

Figure 3.51 presents the desired torque (the upper plot) and the actual torque (the bottom plot) along Z_6 axis, while Figure 3.52 exhibits the actual force along X_6 axis (the upper plot), the actual force along Y_6 axis (the bottom plot). The results reflect the two contact events. For example, the first contact event takes place at between 5.60 second and 8.70 second. It can be observed between I_1 (5600^{th} sample) and J_1(8700^{th} sample) of the desired torque along Z_6 axis (upper plot of Figure 3.51), and between I_2 (240^{th} sample) and J_2 (370^{th} sample) of the actual torque along Z_6 axis (bottom plot of Figure 3.51). The second contact event occurs at between 11.50 second and 14.70 second. It can be observed between K_1 (1150^{th} sample) and L_1 (1470^{th} sample) of the desired torque along Z_6 axis, and between K_2 (490^{th} sample) and L_2 (615^{th} sample) of the actual torque along Z_6 axis. The positive torque along Z_6 axis between M_2 and K_2 (Figure 3.51) is generated by the user when rotating the stylus in clockwise direction before the second contact event. In addition, the two contact events can be observed from the actual force along X_6 and Y_6 axes (Figure 3.52). As expected, one can see small positive force along X_6 axis (between I_3 and J_3 of Figure 3.52) and small negative force along Y_6 axis (between I_4 and J_4 of Figure 3.52) during first contact event. One can also observe small positive force along both X_6

(between K_3 and L_3 of Figure 3.52) and Y_6 (between K_4 and L_4 of Figure 3.52) axes during the second contact event.

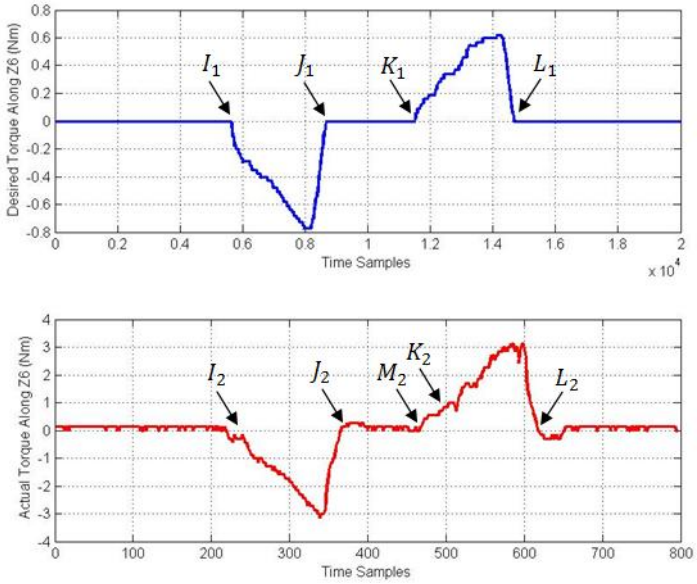

Figure 3.51: The desired torque along Z_6 axis (in blue); the actual torque along Z_6 axis (in red)

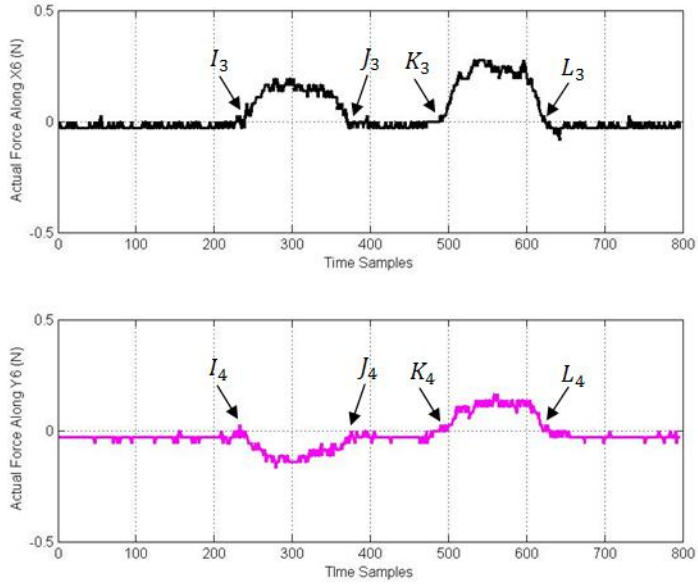

Figure 3.52: The actual force along X_6 axis (in black); the actual force along Y_6 (in magenta)

To sum up, this chapter presented the design and development of electronic interface and application software of the proposed haptic user interface. The electronic interface was able to perform desired functionalities and to provide 1 KHz update rates which satisfies the requirement of rendering realistic haptic feedback force. Multi-threaded programming approach was used to develop the application softwares for the haptic user interface. The application softwares were developed under one software framework and modified according to the objectives of haptic interaction experiments. Kinematic and force correspondence experiments were designed and performed to evaluate the displacements and forces/torques correspondence given by user and those applied to the virtual environment. The results indicated sufficient correspondences on these two critical factors of the haptic interface. Three preliminary experiments of virtual interaction with test-based environments were demonstrated to examine the performance of the haptic interface. The results suggested that the haptic user interface was able to provide 6 axes force/torque display. The results demonstrated that the actual force/torque exerted at the user well reflected the computed or desired force/torque provided that the magnitude of the force interaction is relatively small and the stiffness of the virtual object is relatively low. The results also indicated time delay of the actual force/torque measurements which can be attributed to the serial communication with F/T controller and the various different delays in the haptic control loop, such as quantization delay and amplifier delay.

Chapter 4

Performance Enhancement of the Haptic Interaction

4.1 Introduction

The proposed haptic interface can be used in virtual reality and remotely controlled robotic systems, such as surgical simulators and robotic surgery. The most important criteria of the haptic interface is the transparency. The transparency of a haptic interface means that it should transmit as faithfully as possible the desired forces to the user when there is interaction in the virtual environments and be otherwise not felt by the user. Transparency requires the haptic interface to be a light interface and is able to stably render high stiffness virtual object.

The light interface ensures that there is no or minimal resistance force felt by the user when he/she moves the stylus of the haptic device in free space. In order to achieve this goal, the gravity and friction effects of the haptic device are required to be eliminated. Researchers have proposed feed-forward gravity and friction compensation method in haptic interface to resolve this issue [44]-[47]. Due to the nonlinearity nature, the gravity and friction parameters are often estimated through system identification which requires the knowledge of dynamic model of the haptic device [48] and [49].

To create a stable control system that provides high fidelity under any operating conditions and any virtual environment parameters is another important aspect of the transparency of haptic interface. An unstable haptic control system exhibits vibration or divergent behavior which significantly degrade the fidelity of haptic force feedback. In the optimal case scenario, the haptic interface should be able to render absolute rigid object with infinite stiffness. However, it is not possible in real world because of mechanical and electrical limitations of the haptic interface (e.g. the mechanical structure of the haptic device, the maximum torque of the motor, the latency issue in the haptic loop, etc.)[35]. As a result, the realism of the haptic interface often be reduced in order to guarantee the overall stability of the system.

In pervious chapter, the electronic interface and the application software have been established. Kinematic and force correspondence characteristics of the haptic interface have been verified. The preliminary experiments of virtual interaction with test-based environments have been demonstrated to examine the performance of the haptic interface. In this chapter, we investigate the methods to enhance the performance of the haptic interface. The chapter is organized as follows. In Section 4.2, we investigate feed-forward gravity compensation method. In Section 2, we present the passivity control method.

4.2 Gravity Compensation

Gravity compensation is aimed to eliminate gravitational effect in haptic rendering and to enhance the transparency of the haptic interface. In this section, we first establish an analytical model of the gravity forces and the resulting torques of the haptic device. Then, we determine the corresponding six actuator joint torques which are used to cancel to gravitational effect on each actuator joint. Lastly, the gravity compensation method is verified through experiments.

4.2.1 Gravity Force Decomposition

According to the design of the hybrid manipulator, the weight of the mobile platform is supported by the passive links of the spherical parallel mechanism. Therefore, the gravity compensation is aimed to compensate the gravity force of the serial mechanism. The weight of serial mechanism consists of two parts G_1 and G_2.

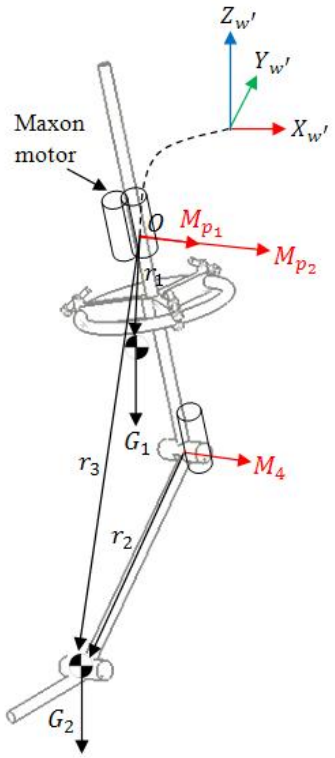

Figure 4.1: Gravity force decomposition plot

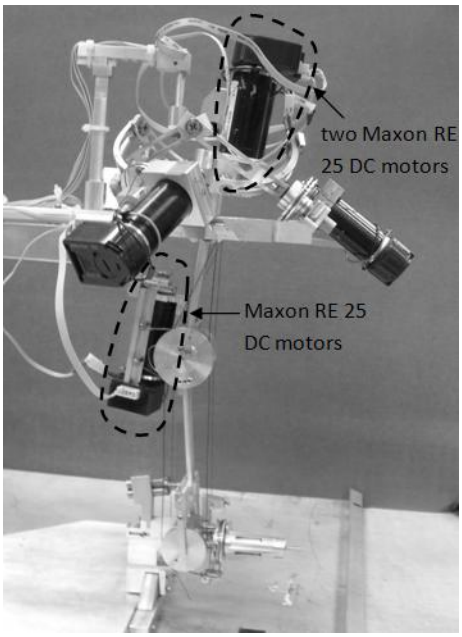

Figure 4.2: The view of the actual device

Figure 4.1 depicts the gravity force vectors (G_1, G_2) and the resulting torque vectors (M_{p_1}, M_{p_2} and M_4). Specifically, G_1 includes the weight of three Maxon RE 25 DC motors and the serial link l_1. Figure 4.2 depicts the location of the three Maxon motors on the actual device. G_2 includes the weight of the serial link l_2 and the stylus. r_1 and r_3 are the position vectors of the center of mass of G_1 and G_2 with respect to $\{W'\}$ frame which coincides with the center of rotation "O'', while r_2 is the position vector of G_2 with respect to joint 4 frame. M_{p_1} and M_{p_2} are the moment vectors acting at the center of rotation "O'' caused by G_1 and G_2 respectively. M_4, which is caused by G_2, is the moment vector acting at the origin of joint 4 frame.

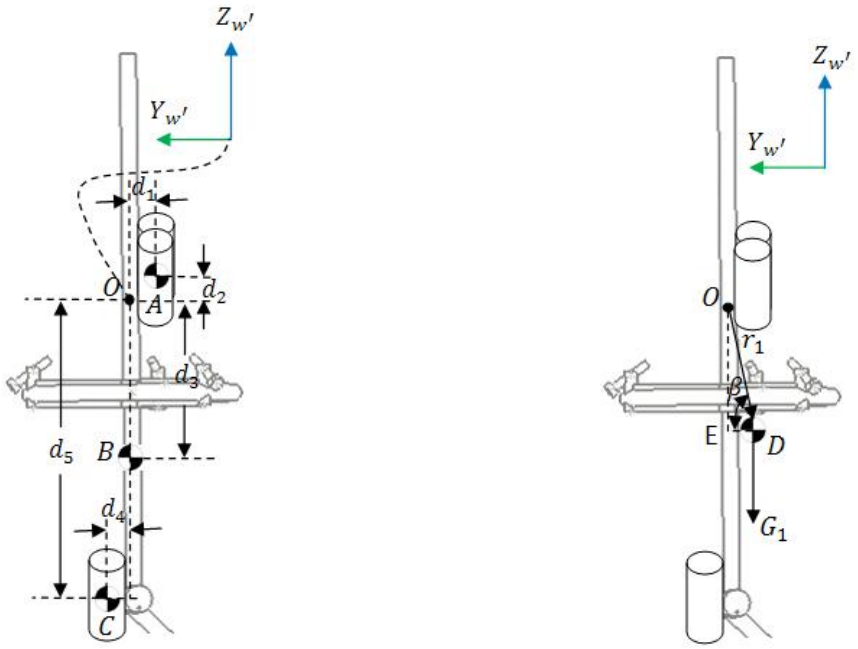

(a) (b)

Figure 4.3: Position of the center of mass G_1 at physical home configuration: (a) Position of the three weight components; (b) Position of the center of mass of G_1

In order to solve for the three moment vectors, we need to determine the position of the center of mass of G_1 and G_2. Due to the complexity of the geometrical shape and the uneven mass distribution of the mechanism, we regard G_1 as combination of three discrete weight components. Figure 4.3.a describes the position of three weight components at physical home configuration. The first weight component is the weight of two Maxon motors whose center of mass is located at point A. The second weight component is the weight of serial link l_1 whose center of mass is located at point B. The third weight component is the weight

of one Maxon motor whose center of mass is located at point C. Table 4.1 summarizes the weight of the three mass components and the corresponding position of centers of mass with respect to $\{W^{'}\}$ frame at physical home configuration. The position of the center of mass of G_1 is solved based on the three discrete weight components.

Table 4.1: The summary of the weight of three mass components of G_1 and the corresponding position of centers of mass

	Weight (N)	X (mm)	Y (mm)	Z (mm)
A	3.21	12.5	0	9.5
B	0.20	0	0	-73
C	1.61	-12.5	0	-146

Figure 4.3.b depicts the position of the center of mass of G_1 (point D) at the physical home configuration. r_1 is the position vector from the center of rotation "O'' to point D. OE is the projection of r_1 to the serial link in such condition. Equation (4.1) and (4.2) exhibit the analytical expression of the position of point D at home configuration. $Z_{D_{home}}$ stands for the position of point D along $\widehat{Z_{w'}}$ axis while m_A represents the weight of the weight component A. X_{D_home} is 0 at the physical home configuration.

$$Z_{D_{home}} = \frac{m_A Z_A + m_B Z_B + m_C Z_C}{m_A + m_B + m_C} = -43.53mm \tag{4.1}$$

$$Y_{D_{home}} = \frac{m_A X_A + m_B X_B + m_C X_C}{m_A + m_B + m_C} = -4.0mm \tag{4.2}$$

Equation (4.3) describes the position of point D if and only if there is a rotation along $\widehat{Z_{w'}}$ axis. $Y_{D_{Z_{w'}}}$ stands for the position of point D along $\widehat{Y_{w'}}$ axis in such condition while $\theta_{Z_{w'}}$ represents the angle of rotation along $\widehat{Z_{w'}}$ axis.

$$Y_{D_{Z_{w'}}} = -|Y_{D_{home}}|cos(\theta_{Z_{w'}}); \quad X_{D_{Z_{w'}}} = |Y_{D_{home}}|sin(\theta_{Z_{w'}}); \quad Z_{D_{Z_{w'}}} = 0 \tag{4.3}$$

Equation (4.4) describes the position of point D if and only if there is a rotation along $\widehat{X_{w'}}$ axis. $Z_{D_{X_{w'}}}$ stands for the position of point D along $\widehat{Z_{w'}}$ in such condition while $\theta_{X_{w'}}$ represents the angle of rotation along $\widehat{X_{w'}}$ axis. β is the angle between r_1 and ED as shown in Figure 4.3.b which can be determined by equation 4.5.

$$Z_{D_{X_{w'}}} = -|r_1|sin(\beta - \theta_{X_{w'}}); \quad Y_{D_{X_{w'}}} = -|r_1|cos(\beta - \theta_{X_{w'}}); \quad X_{D_{X_{w'}}} = 0 \tag{4.4}$$

$$\beta = atan2(|OE|, |ED|) = atan2(|Z_{D_{home}}|, |Y_{D_{home}}|) = 84.75^{\circ} \tag{4.5}$$

Equation (4.6) describes the position of point D if and only if there is a rotation along $\widehat{Y_{w'}}$ axis. $Y_{D_{Y_{w'}}}$ stands for the position of point D along $\widehat{Y_{w'}}$ in such condition while $\theta_{Y_{w'}}$ represents the angle of rotation along $\widehat{Y_{w'}}$ axis.

$$X_{D_{Y_{w'}}} = -|Z_{D_{home}}|sin(\theta_{Y_{w'}}); \quad Z_{D_{X_{w'}}} = -|Z_{D_{home}}|cos(\theta_{Y_{w'}}); \quad Y_{D_{Y_{w'}}} = 0 \tag{4.6}$$

Overall, the position of the center of mass of G_1 (point D) is the combination of above three conditions as formulated in equation (4.7). The position vector r_1 can be formulated as $[X_D, Y_D, Z_D]^T$.

$$X_D = X_{D_{Z_{w'}}} + X_{D_{Y_{w'}}}; \quad Y_D = Y_{D_{Z_{w'}}} + Y_{D_{X_{w'}}}; \quad Z_D = Z_{D_{Y_{w'}}} + Z_{D_{X_{w'}}} \tag{4.7}$$

Since the weight of stylus is significantly greater than that of the serial link l_2, we assign the center of mass of G_2 to coincide with the origin of the stylus frame. Therefore the position vector r_3 is the same as the position vector of the stylus frame with respect to frame $\{W'\}$, which can be obtained from the forward kinematic result.

Having solved for the position vectors of G_1 and G_2, the resulting moment vectors M_{p_1}, M_{p_2} and M_4 can be determined by equation (4.8).

$$\begin{aligned} M_{p_1} &= r_1 \times G_1 \\ M_{p_2} &= r_3 \times G_2 \\ M_4 &= r_2 \times G_2 \end{aligned} \tag{4.8}$$

where,

$$r_1 = [X_D, Y_D, Z_D]^T$$

$$r_2 = [^{w'}P_{6_x} - {}^{w'}P_{4_x}, {}^{w'}P_{6_y} - {}^{w'}P_{4_y}, {}^{w'}P_{6_z} - {}^{w'}P_{4_z}]^T$$

$$r_3 = [^{w'}P_{6_x}, {}^{w'}P_{6_y}, {}^{w'}P_{6_z}]^T$$

$$G_1 = [0, 0, -5.02]^T;\ G_2 = [0, 0, -0.76]^T$$

In order to determine actuator joint torques resulted from the gravity force of the serial mechanism, we need to map the moment vectors M_{p_1}, M_{p_2} and M_4 to the corresponding actuator joint torques. We denote the moment vector acting at the mobile platform as M_p, which is the sum of M_{p_1} and M_{p_2}. Equation (4.9) maps M_p to the three spherical parallel actuator joints torques (τ_1, τ_2 and τ_3). J is the Jacobian matrix of the spherical parallel mechanism determined in Chapter 2. Equation (4.9) maps M_4 to the torque of actuator joint 4, τ_4.

$$\tau = [\tau_1, \tau_2, \tau_3]^T = J^{-T} M_p \tag{4.9}$$

$$\tau_4 = M_4 \hat{X} \tag{4.10}$$

4.2.2 Implementation of Gravity Compensation

In this section, we implement the gravity compensation model. The gravity compensation experiment is aimed to demonstrate that the gravity effect of the haptic device is effectively eliminated. In other words, the haptic device should be able to maintain any given configuration if there is no external force applies to the device.

In the gravity compensation experiment, the user moves the stylus of the device to number of arbitrary positions and orientations at low speed. The haptic device should be able to maintain the position and orientation of the stylus if the user stop moving the stylus. Figure 4.4 describes the software sequence diagram of the gravity compensation experiment. Comparing with the overall software sequence diagram (Figure 3.8), the Haptic Control thread of the gravity compensation experiment does not require collision detection and mechanics of interaction tasks but the gravity compensation task. The gravity compensation task determines the moment vectors (M_{p_1}, M_{p_2} and M_4) based on the kinematic configuration of the device. The force mapping task maps the moment vectors to the actuator joint torques.

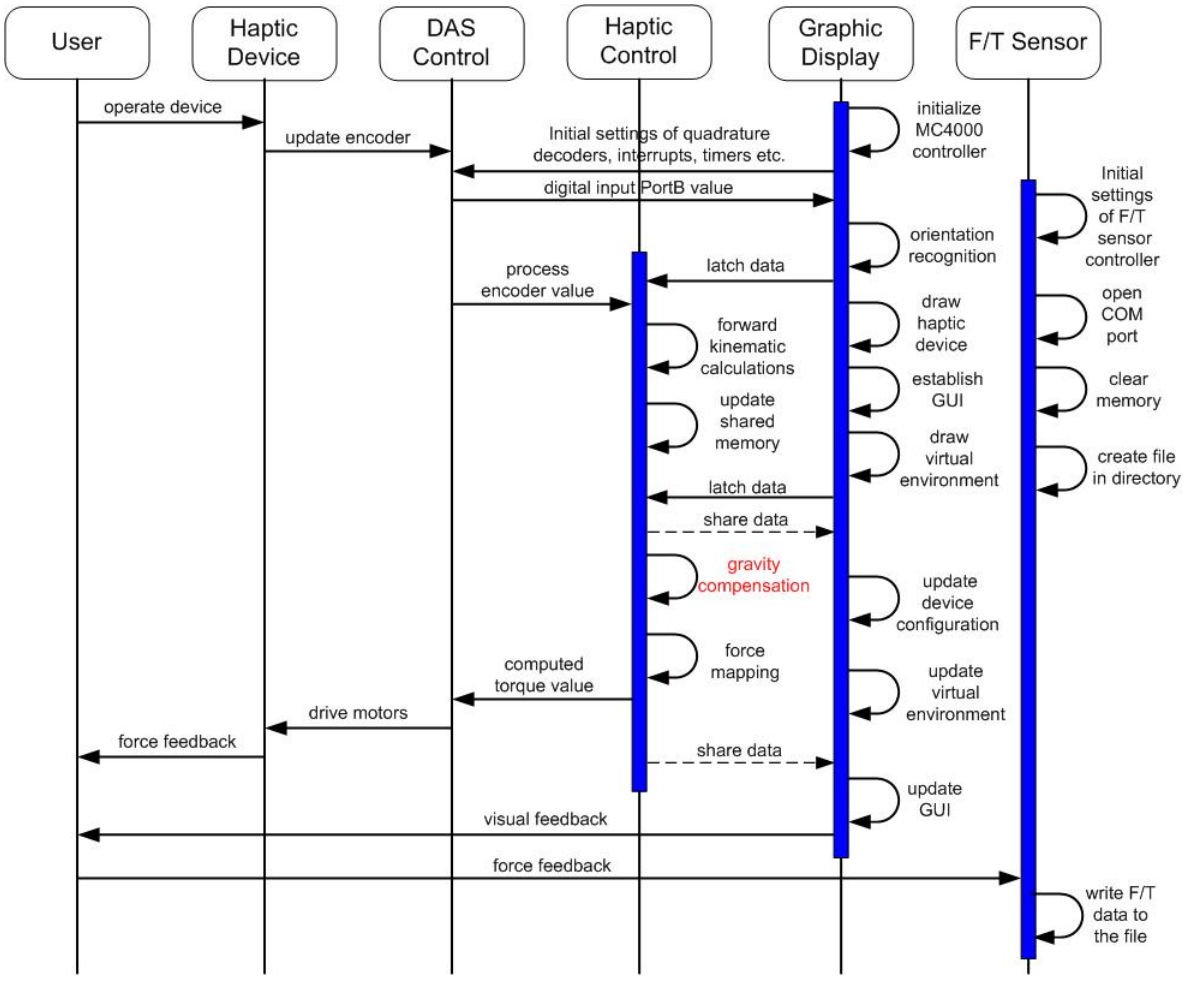

Figure 4.4: Software sequence diagram of gravity compensation experiment

Figure 4.5 and Figure 4.6 depict the six actuator joint angles and actuator joint torques which are collected in real time through the gravity compensation experiment. The user moves the stylus to four arbitrary positions and orientations at four sample times (S_1 - S_4). Figure 4.7 and 4.8 exhibits the actual device configuration at these four sample times.

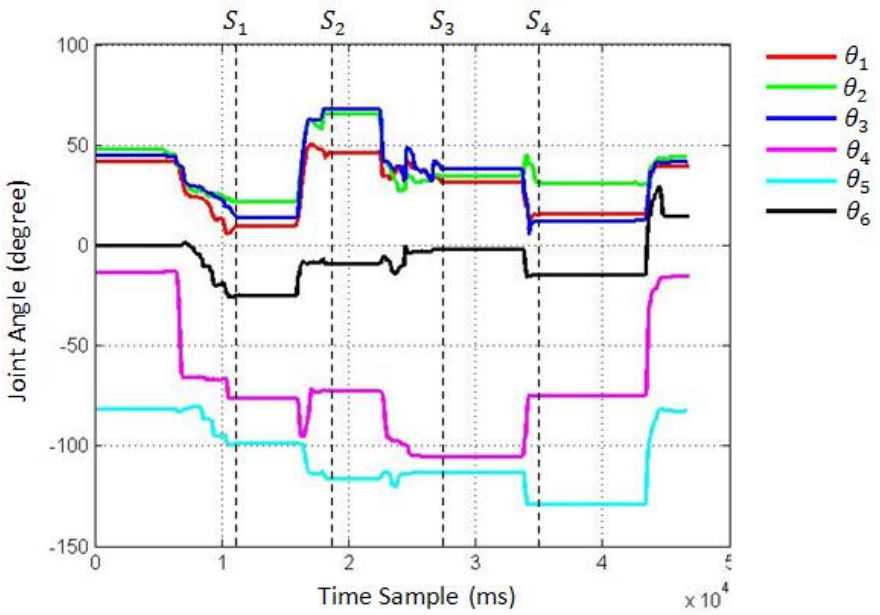

Figure 4.5: Actuator joint angles of the gravity compensation experiment

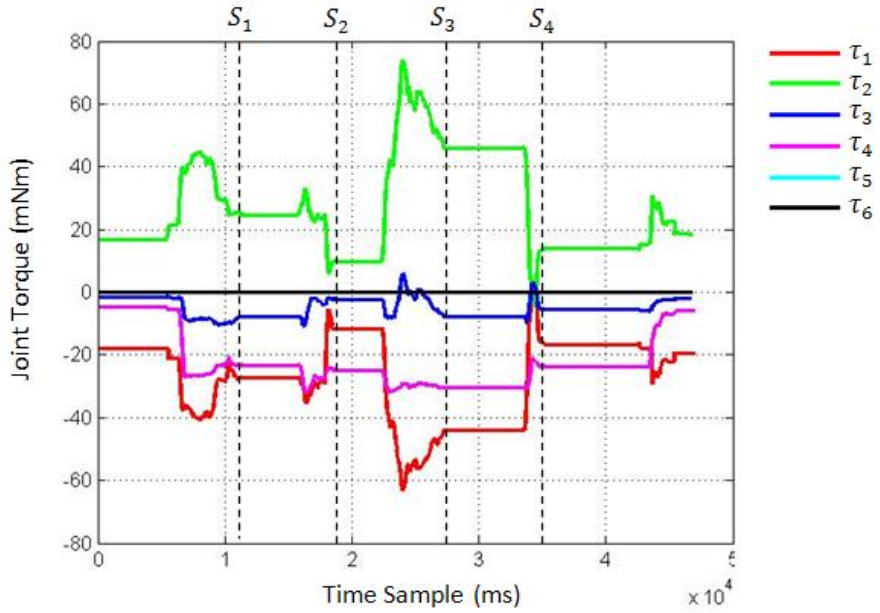

Figure 4.6: Actuator joint torques of the gravity compensation experiment

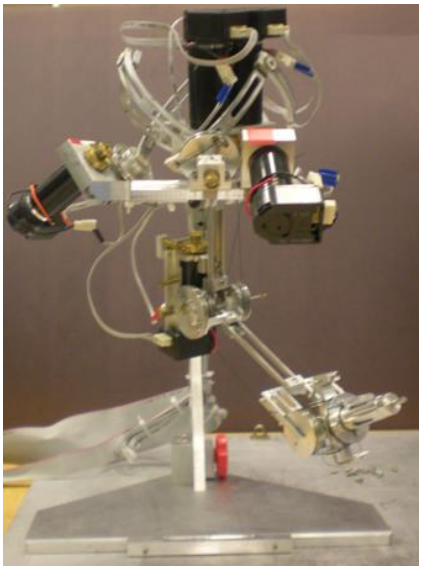

(a) S_1

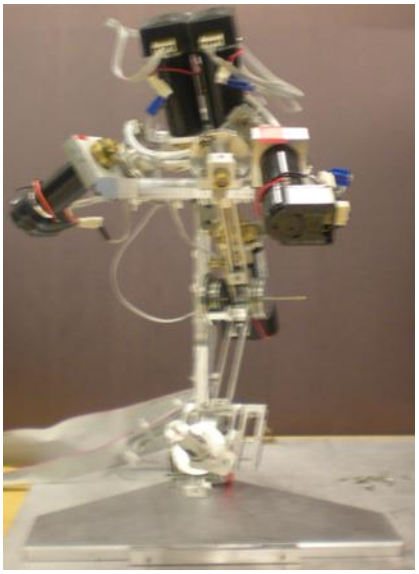

(b) S_2

Figure 4.7: The actual device configurations of the gravity compensation experiment, (a): the device configuration at S_1 ; (b): the device configuration at S_2

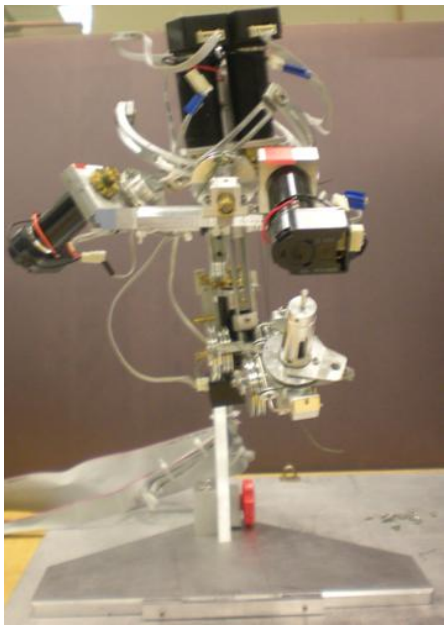

(a) S_3

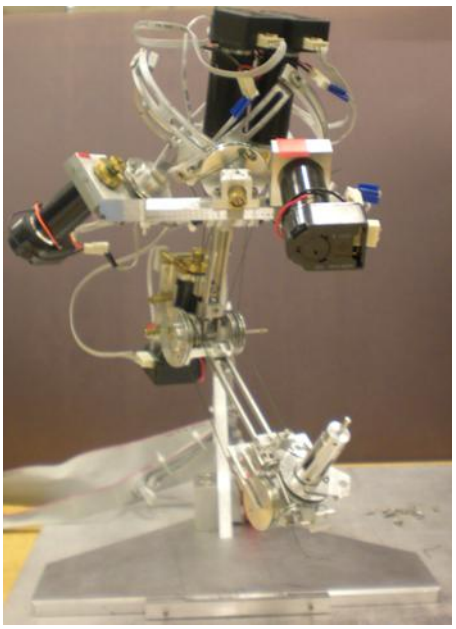

(b) S_4

Figure 4.8: The actual device configurations of the gravity compensation experiment, (a): the device configuration at S_3 ; (b): the device configuration at S_4

The gravity compensation model is able to maintain the device configurations at the four sample times. This can be observed from the values of joint angles and the corresponding joint torques at the four sample times. For examples, the values of six joint angles remains unchange from sample time S_1 until the user moves the stylus to the next position and orientation at S_2. Meanwhile, the values of six joint torques remains unchange from sample time S_1 until the user moves the stylus to the next position and orientation at S_2. Referring to Figure 4.6, the value of τ_5 is 0 for all time which represents that there is no gravitational compensation of the stylus. The reason is that the center of mass of G_2 is assigned at the origin of the stylus (Figure 4.1). Nevertheless, the stylus is still able to maintain its desired configuration. The reason is that the mechanical structural friction of the stylus plays the role of compensating the gravity of the stylus. Based on the experimental results, we can conclude that the gravity compensation model is able to largely eliminate the gravity effect of the haptic device.

4.3 Passivity Control

During the past decade, extensive research has been conducted in the design of haptic interface which is able to render more rigid object without sacrificing the stability. Virtual coupling between the virtual environment and the haptic device is one of the well-known method ([50], [51], [40]). The virtual coupling is a virtual mechanical system containing a combination of series and parallel elements interposed between the haptic device and the virtual environment to limit the maximum or minimum impedance presented by the virtual environment in such a way as to guarantee stability. Virtual coupling design depends on various parameters of the virtual environment as well as the haptic device. For example, the dynamic parameters of the haptic device; the position/velocity input and force output (for an impedance-based haptic interface) of the virtual environment. As matter of the fact, the dynamic parameters of the haptic device (especially the proposed hybrid structure haptic device) are very difficult to identify. Moreover, parameters of virtual environments are always nonlinear and the dynamic properties of a human operator are always involved. Therefore, the aforementioned factors indicates that the virtual coupling method is not the best approach for the proposed haptic interface.

Energy-based approaches ([52]-[54] and [35]) have been used to analyze the limitations and provide stability conditions of haptic interface. It has been proven that passivity is

sufficient for stability, if the human operator is described as unknown passive elements [55]. Comparing with virtual coupling method, passivity approach does not restricted by the dynamic parameters of the haptic device and allows a global stability conclusion to be drawn from considering system blocks individually.

The passivity concept has its roots in the analysis of passive circuit elements and circuit networks [56]. The electric power is defined as the time rate of change of energy. For passive circuit elements (e.g. resistor, inductor and capacitor), any gain in power must be due to the application of an external energy source (voltage and current sources). Active elements (e.g. transistors) can exhibits power gain because they can amplify an input signal to produce an output signal having greater power than input.

The passivity theory has been used in stability analysis of haptic interface system for the past two decades ([54], [57], [58], [41]). In general, the energy of a haptic interface system can be characterized by the integration of the product of force and velocity over time. The force and velocity are analogous to the voltage and current respectively in electric circuit perspective. There is another analogy which relates the force to current; the velocity to force [42]. For this thesis work, we use force to voltage and velocity to current analogy. Using intuitive energy concepts, we know that a system is passive if and only if the energy flowing in exceeds the energy flowing out for all time. The excess energy can be generated by the latency issues in the haptic control loop (e.g. computational delay, quantization delay, amplifier delay) and the interactions between the discrete time system and the continuous time device/human operator. The excess energy may cause instability if not dissipated by the haptic device's intrinsic friction or through system energy control. Ellis et al. [59] predict the position of the device at the next time step to reduce the generation of excess energy. Stramigioli et al. [57] implement a port-Hamiltonian approach to track and dissipate the excess energy.

In this section, we design and implement passivity observer combined with passivity controller to enhance the stability of the proposed haptic interface when interacting with virtual environment. Section 4.3.1 discusses passivity properties of different network configurations. Section 4.3.2 investigates processes of establishing passivity observer and passivity controller in proposed haptic interface system. Section 4.3.3 presents the experimental studies of implementing the passivity control in the proposed haptic interface system.

4.3.1 Passivity Properties of Network

One-port and Multi-port networks as shown in Figure 4.9 can be used to represent a haptic interface system. We define the sign convention for all forces and velocities so that their product is positive when power enters the system port.

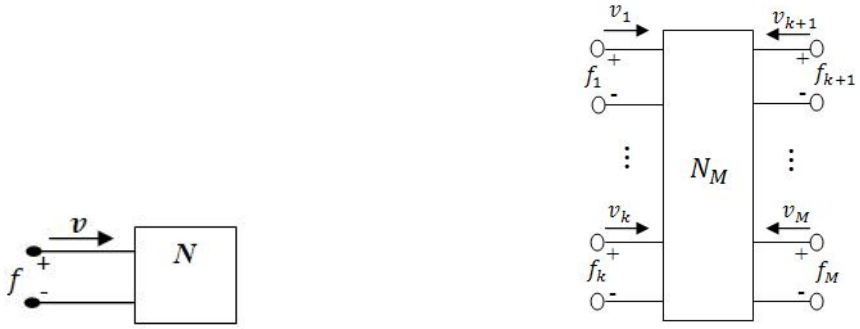

Figure 4.9: Network models: (a) One-port network; (b) Multi-port network

The definitions of the passivity of one-port network and multi-port network are shown in equation (4.11) and (4.12) respectively [41], where $E(0)$ is the system stored energy at $t = 0$. These two equations state that the energy supplied to a passive network must be greater than negative $E(0)$ for all time in order to maintain the passivity of the system [40].

$$\int_0^t f(\tau)v(\tau)d\tau + E(0) \geq 0, \qquad \forall t \geq 0 \tag{4.11}$$

$$\int_0^t (f_1(\tau)v_1(\tau) + \ldots + f_M(\tau)v_M(\tau))d\tau + E(0) \geq 0, \qquad \forall t \geq 0 \tag{4.12}$$

It is a common goal to make the haptic system appear passive to the user. The network is passive if and only if the overall energy in the system is greater than zero [61],[56].

4.3.2 Passivity Observer and Passivity Controller

In this thesis work, we focus on the energy supply to the virtual environment. Hence, we use the one-port network model to represent the haptic interface system as described in Figure 4.10, where v_1 is the velocity of the stylus of the device while f_1 is the desired force to be rendered at the stylus which is determined based on the simulation law in the virtual environment.

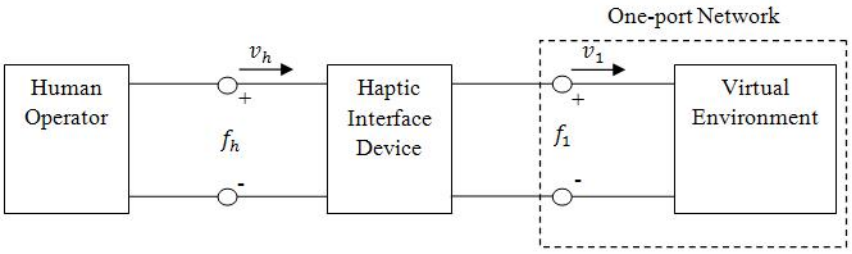

Figure 4.10: The network model of the haptic interface system

In order to maintain the passivity of the system, we need to monitor the system energy in real time. Hence, we design a passivity observer to monitor the energy flow of the system in real time. Equation 4.13 depicts the discrete time expression of passivity observer of a one-port network model, where k stands for the time index; n represents the current time index; ΔT represents the sampling time interval.

$$E_{obsv}(n) = \Delta T \sum_{k=0}^{n} f(k)v(k) \tag{4.13}$$

If $E_{obsv}(n) \geq 0$ for every n, the system is passive and dissipates energy. If there is an instance that $E_{obsv}(n) \leq 0$, the system is active and generates energy. The amount of the generated energy is $-E_{obsv}(n)$. Having established the passivity observer, the energy flow in the system is able to be monitored and the amount of generated energy at any time instance, if any, is able to be determined.

In order to keep the system passive at all time, we then design a passivity controller which is a time-varying dissipative element absorbing the exact amount of generated energy at each time sample [41]. There are two different configurations of the passivity controller, series and parallel. The series passivity controller is designated for impedance type of haptic interface system while the parallel passivity controller is designated for admittance type of haptic interface system.

We first examine the characteristic of a series passivity controller. Referring to Figure 4.11, f_1 is the desired force at the stylus of the haptic device determined based on the simulation law of the virtual environment and the passivity controller; f_2 is the desired force at the stylus determined based on the simulation law of the virtual environment; v_1 is the actual linear velocity of the stylus; v_2 is the linear velocity of the stylus interpreted

by the virtual environment (v_1 is identical with v_2 in series passivity controller model); α is the adaptive elements determined by the passivity controller. Comparing with the electric circuit system, f, v and α are analogous to voltage, current and impedance respectively. Therefore, we can describe the relationship of these three parameters as equation (4.14) - (4.16).

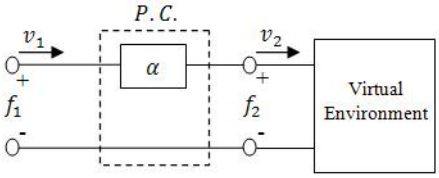

Figure 4.11: The series passivity controller

$$f = \alpha v \tag{4.14}$$

$$v_1 = v_2 \tag{4.15}$$

$$f_1 = f_2 + \alpha v \tag{4.16}$$

We compute α in real time as follow:

1) Determine the system energy at time n as shown in equation 4.17. $f_2(n)v_2(n)$ is the energy supply to the system at time n, while $\sum_{k=0}^{n-1}(f_2(k)v_2(k) + \alpha(k)v_2(k)^2)$ is the initial system energy at time n.

$$W(n) = \frac{1}{\Delta T}E_{obsv}(n) = f_2(n)v_2(n) + \sum_{k=0}^{n-1}(f_2(k)v_2(k) + \alpha(k)v_2(k)^2) \tag{4.17}$$

2) Determine α at time n based on $W(n)$ as shown in equation (4.18). One is able to observe that $\alpha(n)$ is activated when the system generates energy (i.e. $W(n) < 0$).

$$\alpha(n) = \begin{cases} -\frac{W(n)}{v_2(n)^2} & if W(n) < 0, \\ 0 & if W(n) \geq 0. \end{cases} \tag{4.18}$$

With the knowledge of $\alpha(n)$, the output of the passivity controller, f_1, at time n can be determined as equation (4.19). $\alpha(n)v_2(n)$ is regarded as passivity controlled force at time n.

$$f_1(n) = f_2(n) + \alpha(n)v_2(n) \tag{4.19}$$

As for the parallel passivity controller, the input is force while the output is velocity. Referring to Figure 4.12, f_1, which is identical with f_2, is the force exerted at the stylus of the haptic device; v_1 is the desired velocity of the stylus determined based on simulation law of the virtual environment; v_2 is the actual velocity determined based on the simulation law of the virtual environment and the parallel passivity controller. Equation (4.20) and (4.21)describe the relationship among these parameters.

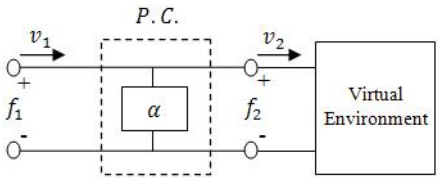

Figure 4.12: The parallel passivity controller

$$f_1 = f_2 \tag{4.20}$$

$$v_2 = v_1 - \frac{f_1}{\alpha} \tag{4.21}$$

We compute α in real time as follow:

1) Determine the system energy at time n as shown in equation (4.22). $f_2(n)v_2(n)$ is the energy supply to the system at time n, while $\sum_{k=0}^{n-1}(f_2(k)v_2(k) + \frac{1}{\alpha(k)}f_2(k)^2)$ is the initial system energy at time n.

$$W(n) = \frac{1}{\Delta T}E_{obsv}(n) = f_2(n)v_2(n) + \sum_{k=0}^{n-1}(f_2(k)v_2(k) + \frac{1}{\alpha(k)}f_2(k)^2) \tag{4.22}$$

2) Determine α at time n based on $W(n)$ as shown in equation (4.23).

$$\frac{1}{\alpha(n)} = \begin{cases} -\frac{W(n)}{f_2(n)^2} & if W(n) < 0, \\ 0 & if W(n) \geq 0. \end{cases} \tag{4.23}$$

With the knowledge of $\alpha(n)$, the output of the parallel passivity controller, v_1, at time n can be determined as equation (4.24). $\frac{f_2(n)}{\alpha(n)}$ is regarded as passivity controlled velocity at time n.

$$v_1(n) = v_2(n) - \frac{f_2(n)}{\alpha(n)} \tag{4.24}$$

4.3.3 Implementation of Passivity Control

In this section, we implement the passivity observer and passivity controller in the haptic control loop when interacting with the virtual environment. The series passivity controller is implemented since our haptic interface system is impedance type.

Before implementing the passivity control function, the velocity of the stylus needs to be determined in real time. The analytical model of determining the velocity of the stylus based on actuator joint velocities is established in section 2.6. The actuator joint velocity signals are usually very noisy. In order to obtain clean actuator joint velocities, we design an algorithm to serve as velocity signal filter.

Figure 4.13 describes the software sequence diagram of the gravity compensation experiment. Comparing with the overall software sequence diagram (Figure 3.8), the Haptic Control thread of the passivity control has passivity control task between the mechanics of interaction task and force mapping task.

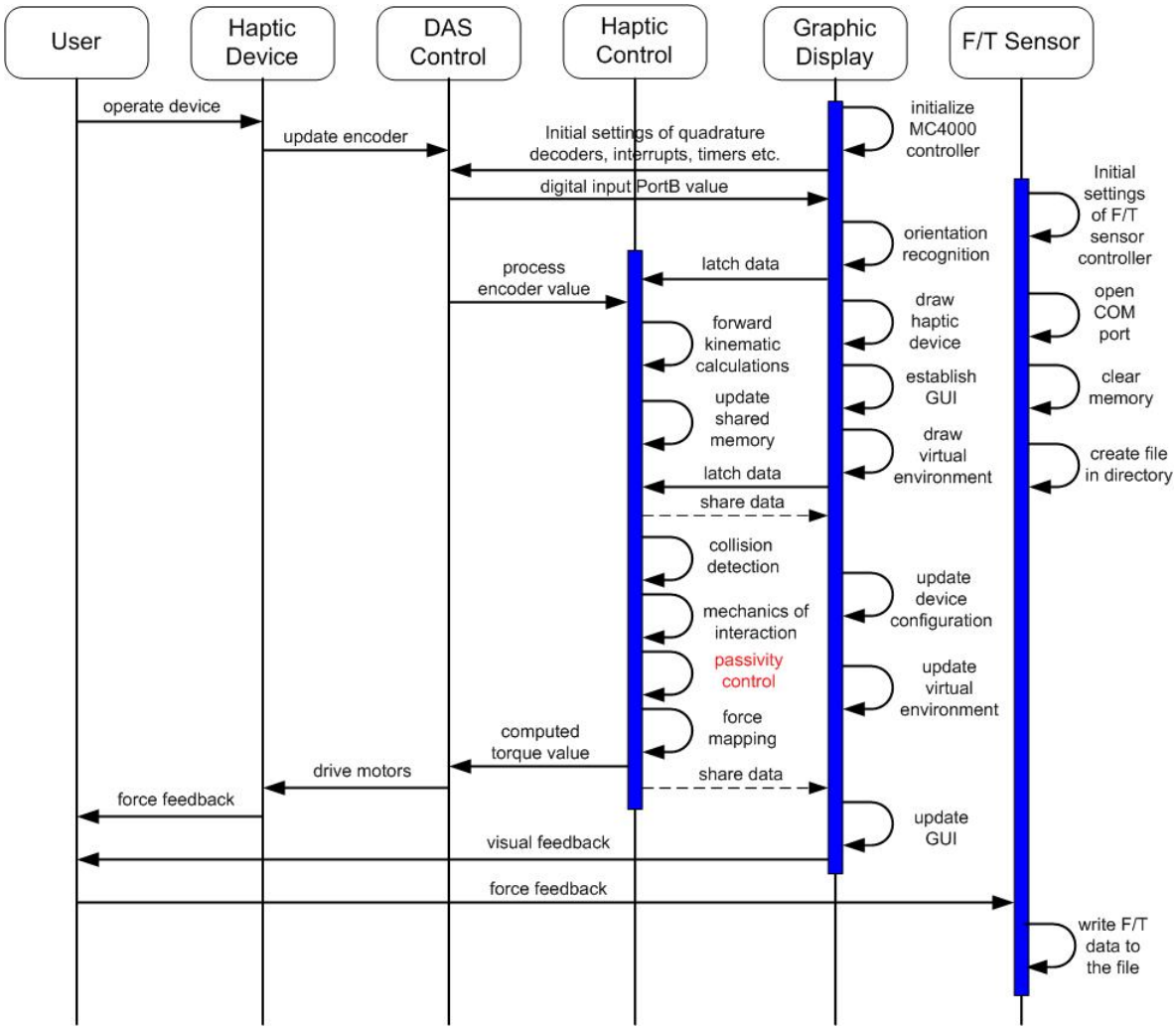

Figure 4.13: Software sequence diagram of passivity control experiment

The algorithm of implementation of the passivity control task is shown in Algorithm 2. The function firstly observers the system energy by computing $W(n)$. After that, it determines α based on the value of the system energy. At last, it computes f_1 which is to be used to determine the actuator joint torques. The passivity control function is running in the haptic control thread at 1KHz, which means that the function updates f_1 every 1 ms.

input : f_2,v_2
output: f_1

currentEnergy $\leftarrow f_2 \cdot v_2$;
acculCurrentEnergy $\leftarrow$ acculCurrentEnergy + currentEnergy ; // $\sum_{k=0}^{n} f_2(k)v_2(k)$
// $W(n) = \sum_{k=0}^{n} f_2(k)v_2(k) + \sum_{k=0}^{n-1} \alpha(k)v_2(k)^2$
netEnergy $\leftarrow$ acculCurrentEnergy + prePassConEnergy;
// determine α based on $W(n)$
if netEnergy < 0 **then**
  $\alpha \leftarrow -$netEnergy/pow$(v_2, 2)$;
else
  $\alpha \leftarrow 0$;
end
$f_1 \leftarrow f_2 + \alpha \cdot v_2$;
prePassConEnergy $\leftarrow$ prePassConEnergy + $\alpha \cdot$ pow$(v_2, 2)$; // $\sum_{k=0}^{n} \alpha(k)v_2(k)^2$

Algorithm 2: Passivity Control

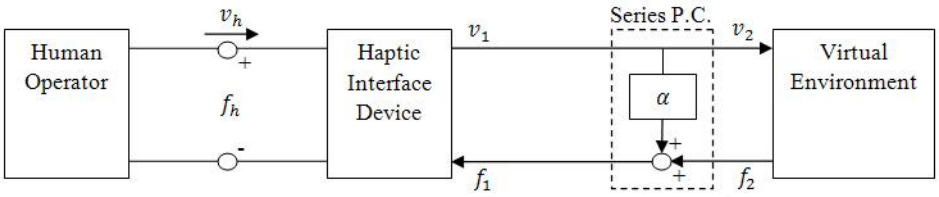

Figure 4.14: Block diagram of the haptic control loop with series passivity controller

Figure 4.14 depicts the block diagram of the haptic control loop with the series passivity controller. The system consists of human operator, haptic interface device, the passivity controller and the virtual environment as shown in Figure 3.40. The system is entirely synchronized at 1 KHz.

Having created the passivity control function, we use the same system set-up that is described in chapter 3 to conduct experiments of interaction with virtual environment. Comparison of the performance of haptic rendering will be made between the system with and without the passivity control function. The virtual environment which we use for these experiments is depicted in Figure 3.40.

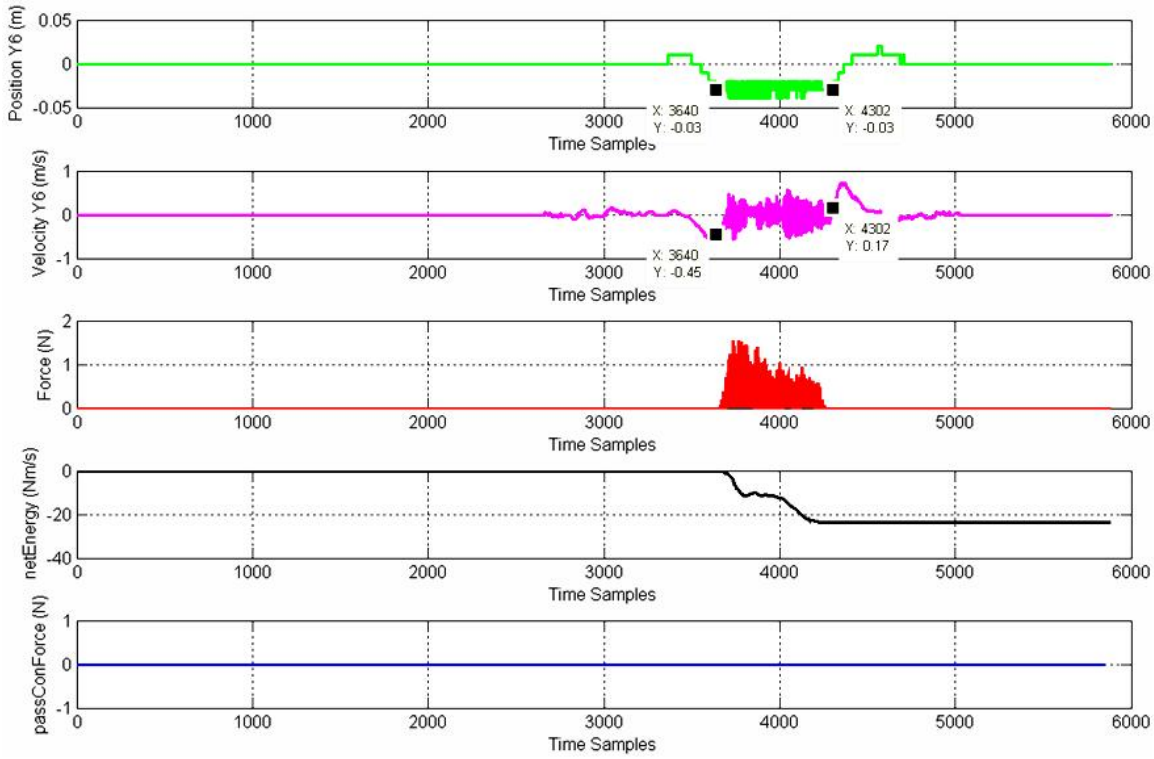

Figure 4.15: Experimental results when the passivity controller is turned off: position of the stylus along Y_6 axis (in green); the linear velocity of the stylus along Y_6 axis (in magenta); the force along Y_6 axis (in red); the system energy (in black); the passivity controlled force (in blue)

For the first experiment, the passivity control function is turned off. The user moves the stylus of the haptic device starting from the physical home position and then makes one-time contact with the right side virtual wall ($k = 150N/m$). Figure 4.15 depicts the experimental results of the position of the stylus along its Y axis (in green); the velocity of the stylus along its Y axis (in magenta); the force f_1 (in red); the net energy $W(n)$ (in black); the passivity controlled force αv_2 (in blue). The operator approaches the right side virtual wall which is located at 0.03 m along the negative Y axis of the stylus coordinate frame with the initial contact velocity of 0.45 m/s. The initial contact event takes place at 3.64 second (3640^{th} sample). The significant oscillation of the position, velocity and force indicates that the system becomes unstable after the initial contact. Meanwhile, the system

net energy $W(n)$ is accumulated to a large negative value, which represents that the system is constantly generating energy and doesn't have ability to dissipate the generated energy. The system becomes, however, stable at 4.3 second (4302^{th} sample), which indicates that the operator plays an active role in stabilizing the system.

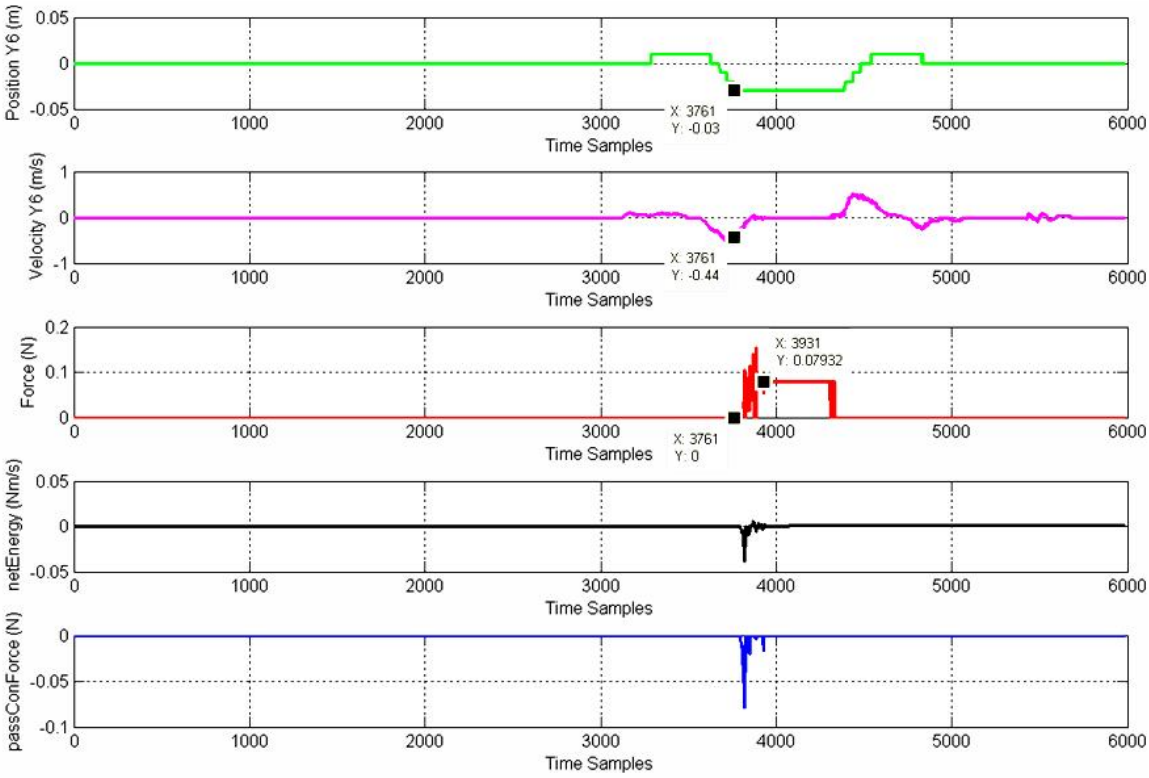

Figure 4.16: Experimental results when the passivity controller is turned on: position of the stylus along Y_6 axis (in green); the linear velocity of the stylus along Y_6 axis (in magenta); the force along Y_6 axis (in red); the system energy (in black); the passivity controlled force (in blue)

For the second experiment, the passivity control function is turned on. The user interacts with the virtual environment with the same fashion as the first experiment. The stiffness of the virtual object remains at $k = 150N/m$. Referring to Figure 4.16, the operator approaches the right side virtual wall with the initial contact velocity of 0.44 m/s. The initial contact event takes place at 3.76 second (3761^{th} sample). Unlike the first experiment,

the passivity controller is turned on immediately after the initial contact because the system net energy $W(n)$ becomes negative when the initial contact occurs. The value of passivity controlled force αv_2 is relatively large at the time of initial contact because it tries to help the system to effectively dissipate the generated energy. The system becomes stable 0.17 second after the initial contact with the assistance of the passivity controller as shown in the force plot of Figure 4.16.

Figure 4.17 depicts the haptic control loop with passivity controller and gravity compensator. Comparison of the performance of haptic rendering will be made between the system with and without the gravity compensator.

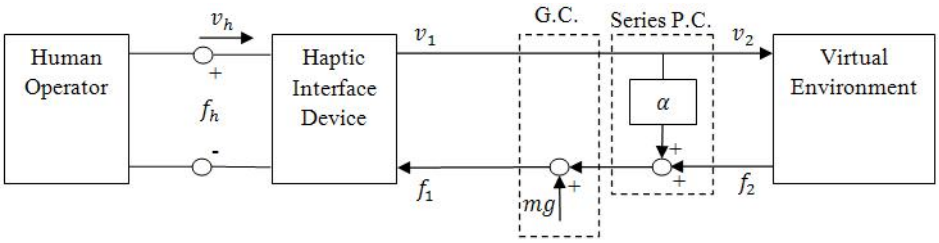

Figure 4.17: Block diagram of the haptic control loop with series passivity controller and gravity compensator

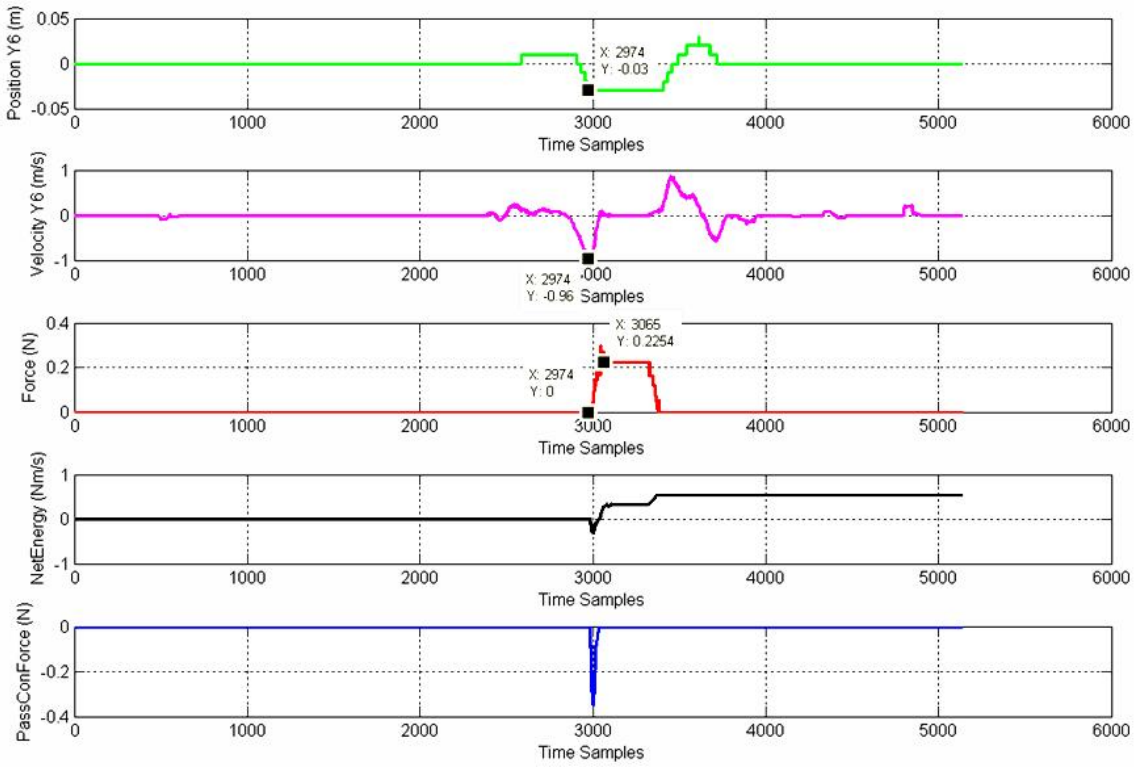

Figure 4.18: Experimental results with passivity controller and gravity compensation: position of the stylus along Y_6 axis (in green); the linear velocity of the stylus along Y_6 axis (in magenta); the force along Y_6 axis (in red); the system energy (in black); the passivity controlled force (in blue)

This experiment utilize the same virtual object as the previous two experiments. The user interacts with the virtual environment with the same fashion as those two experiments. Referring to Figure 4.18, the operator approaches the right side virtual wall with the initial contact velocity of 0.96 m/s. The initial contact event takes place at 2.97 second (2974^{th} sample). The system becomes stable 0.08 second after the initial contact with the assistance of the passivity controller and gravity compensator as shown in the force plot of Figure 4.18. Comparing to Figure 4.16 (the experimental result when the haptic control loop has passivity control function but no gravity compensation function), the system has shorter settling time and less overshot even through the initial contact velocity is significantly larger.

Chapter 5

Conclusion and Future Works

5.1 Discussion and Conclusion

In this thesis, we designed, integrated, evaluated and enhanced the proposed haptic user interface towards surgical training simulator. We derived the mathematical models of the forward and inverse kinematics, Jacobians and static force of the novel 6-DOF hybrid structure haptic device. Numerical examples of the forward and inverse kinematic models were presented to further clarify the derivation. These mathematical models can be used as a general example of the class of hybrid spherical parallel/serial manipulators. In addition, we designed and developed the electronic interface and application softwares for the haptic user interface. The electronic interface was able to perform the desired functionalities and to provide 1 KHz update rates (chapter 3.7) which satisfies the requirement of rendering realistic haptic feed-back force. Multi-threaded programming approach was used to develop the application softwares for the haptic user interface. The application softwares were developed under one software framework and modified according to the objectives of haptic interaction experiments.

We designed and performed kinematic and force correspondence experiments to evaluate the displacements and forces/torques correspondence given by user and those applied to the virtual environment. The results indicated sufficient correspondences on these two critical factors of the haptic interface. Three preliminary experiments of virtual interaction with test-based environments were demonstrated to examine the performance of the haptic interface. The results suggested that the haptic user interface was able to provide 6 axes force/torque display. The results demonstrated that the actual force/torque exerted at the

user well reflected the computed or desired force/torque provided that the magnitude of the force interaction is relatively small and the stiffness of the virtual object is relatively low. The results also indicated time delay of the actual force/torque measurements which can be attributed to the serial communication with F/T controller and the various different delays in the haptic control loop, such as quantization delay and amplifier delay.

To enhance the performance of the proposed haptic interface, we developed and implemented feed-forward gravity compensation and passivity control methods to largely eliminate the gravitational effect of the haptic device and to increase the stability of the haptic user interface. The results of the gravity compensation experiment suggested that the proposed feed-forward gravity compensation method was able to largely eliminate the gravity effect of the haptic device. The results of the passivity control experiment indicated that with the passivity control algorithm built-in, the haptic user interface is able to maintain stability when interacting with more demanding virtual environments (e.g. higher stiffness and contact velocity).

5.2 Future Works

In this thesis, feed-forward gravity compensation method was applied in order to largely eliminate the gravitational effect of the haptic device during the haptic interaction. Due to the complexity of the mechanical structure of the device, various assumptions were made in order to develop the gravity model. Firstly, the gravitational effect of the mobile platform and the active and passive links of the spherical parallel mechanism was considered negligible given that the mobile platform is supported by the passive links. In addition, the center of mass of G_2 (Figure 4.1) was assumed to be located at the origin of the end-effector given that the weight of the stylus is significantly greater than that of the serial link l_2. The experimental results were satisfactory given that the user moves the device with low speed (the inertial effect was minimized). The result indicated that there was no gravitational compensation of the stylus because the center of mass of G_2 was assigned at the origin of the stylus. It is the mechanical structural friction of the stylus plays the role of compensating the gravity of the stylus. The system identification method can be implemented in the future to systematically estimate the gravitational parameter as well as other dynamic parameters of the haptic device such as inertial, coulomb and viscous friction [48], [49]. With the knowledge of these dynamic parameters, feed-forward gravity and friction compensation

models can be developed [44], [46]. These two compensation models will be able to further minimize the resistance force felt by the user when he/she moves the stylus of the haptic device in free space. Hence, the transparency of the haptic user interface can be further increased.

At current stage, the stylus of the haptic device has one rotational DOF about the Z_6 axis as shown in Figure 5.1. To make the device better suited for the application of surgical training, the pinching sensing become critical because it conveys the realistic sensation of the tissue or organ. The pinching mechanism can be designed to create a prismatic motion along the axis that is perpendicular to the revolute joint axis of the stylus. In order to provide the force feedback to the pinch, these two axes of motion can be cooperated. To be specific, the prismatic motion of the pinch can be linked to the prismatic motion along with revolute joint axis by coupling two gears along with these two perpendicular axes. The pinching force feedback can be applied by generating the inverse prismatic motion along the revolute joint axis. An alternative approach for prototyping the pinching force feedback can be implemented by utilizing the potentiometer. Specifically, the prismatic pinching motion can be converted to the change of resistance of the potentiometer. By combining potentiometer with the driver circuit of the servo motor, the resistance change will result in the change of supply voltage to the motor. Hence, the force feedback to the pinch can be provided through.

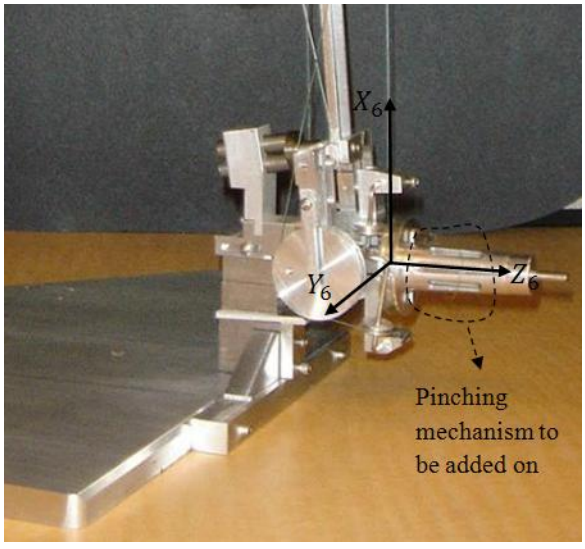

Figure 5.1: The stylus of the haptic device

Since the main focus of this thesis work was to develop a reliable haptic user interface, the virtual environments used in this thesis are simple test-base environments. A surgical training simulator requires not only a reliable haptic user interface but also a comprehensive virtual reality simulation environment which is able to simulate the patient's organs. Researchers from the Experimental Robotics Laboratory at Simon Fraser University have been developing the Virtual Training Environment (VTE) [62] which is aimed to incorporate various important surgical tasks on realistically simulated human tissues and organs. The proposed haptic user interface can be integrated with VTE so that the surgeons can be trained on various important surgical tasks in an advanced virtual reality simulation environment having realistic haptic sensation.

Appendix A

Data Specification Sheets of Hardware Components

maxon DC motor

RE 25 ∅25 mm, Graphite Brushes, 20 Watt

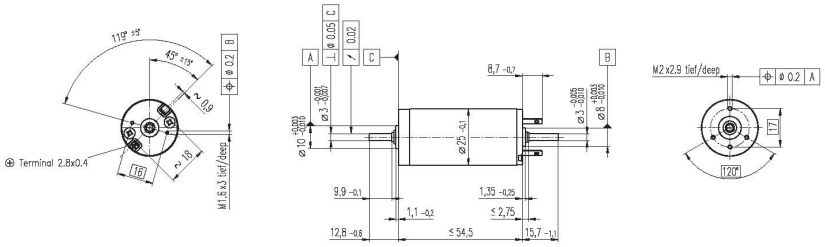

Stock program
Standard program
Special program (on request!)

Order Number	118749	118750	118751	118752	118753	118754	118755	118756	118757
Motor Data									
1 Assigned power rating W	20	20	20	20	20	20	20	20	20
2 Nominal voltage Volt	9.0	15.0	18.0	24.0	30.0	42.0	48.0	48.0	48.0
3 No load speed rpm	10100	9760	10300	9660	9970	11200	10500	8320	5100
4 Stall torque mNm	229	222	218	240	246	280	261	207	127
5 Speed / torque gradient rpm / mNm	47.6	45.7	49.0	41.2	41.3	40.6	40.5	40.6	40.6
6 No load current mA	111	62	55	37	31	26	20	15	9
7 Starting current mA	29100	15700	13500	10300	8720	7940	6030	3810	1440
8 Terminal resistance Ohm	0.309	0.953	1.33	2.32	3.44	5.29	7.96	12.6	33.4
9 Max. permissible speed rpm	11000	11000	11000	11000	11000	11000	11000	11000	11000
10 Max. continuous current mA	1500	1500	1500	1230	1030	841	695	560	350
11 Max. continuous torque mNm	11.8	21.2	24.2	28.4	29.0	29.7	30.1	30.5	31.0
12 Max. power output at nominal voltage mW	52800	52900	55600	58400	62200	80400	70200	44400	16800
13 Max. efficiency %	77	82	83	85	86	87	87	87	84
14 Torque constant mNm / A	7.88	14.1	16.1	23.2	28.2	35.3	43.3	54.4	88.7
15 Speed constant rpm / V	1210	677	592	412	338	271	220	175	108
16 Mechanical time constant ms	6	5	5	5	4	4	4	4	4
17 Rotor inertia gcm²	11.3	10.00	9.11	10.3	10.1	10.1	10.00	9.96	9.91
18 Terminal inductance mH	0.03	0.09	0.12	0.24	0.35	0.55	0.83	1.31	3.48
19 Thermal resistance housing-ambient K / W	14	14	14	14	14	14	14	14	14
20 Thermal resistance rotor-housing K / W	3.1	3.1	3.1	3.1	3.1	3.1	3.1	3.1	3.1
21 Thermal time constant winding s	13	11	10	12	12	12	12	11	11

Specifications

- Axial play 0.05 - 0.15 mm
- Max. **ball bearing** loads
  axial (dynamic)
  not preloaded 3.2 N
  preloaded 3.2 N
  radial (5 mm from flange) 16 N
  Press-fit force (static) 64 N
  (static, shaft supported) 270 N
- Radial play **ball bearing** 0.025 mm
- Ambient temperature range -20 / +100°C
- Max. rotor temperature +125°C
- Number of commutator segments 11
- Weight of motor 130 g
- Values listed in the table are nominal.
  For applicable tolerances (see page 43).
  For additional details please use the maxon selection program on the enclosed CD-Rom.

Operating Range

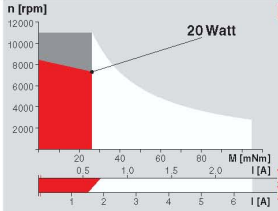

Comments Details on page 49

Recommended operating range

Continuous operation
In observation of above listed thermal resistances (lines 19 and 20) the maximum permissible rotor temperature will be reached during continuous operation at 25°C ambient.
= Thermal limit.

Short term operation
The motor may be briefly overloaded (recurring).

118755 Motor with high resistance winding
118751 Motor with low resistance winding

maxon Modular System

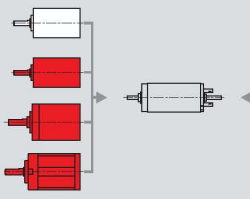

Planetary Gearhead
∅26 mm
0.2 - 1.8 Nm
Details page 180

Planetary Gearhead
∅26 mm
0.5 - 2.0 Nm
Details page 181

Planetary Gearhead
∅32 mm
0.75 - 6.0 Nm
Details page 183 / 186

Planetary Gearhead
∅32 mm
0.4 - 2.0 Nm
Details page 189

Digital MR Encoder
128 - 1000 CPT,
3 channels
Details page 201

Digital Encoder
22 mm
100 CPT, 2 channels
Details page 203

Digital Encoder
HP HED_ 55__
500 CPT, 3 channels
Details page 205 / 207

DC-Tacho
∅22 mm
0.52 V
Details page 213

Brake
∅40 mm
24 VDC, 0.4 Nm
Details page 236

ADVANCED MOTION CONTROLS

Analog Servo Drive **12A8**

Description

The 12A8 PWM servo drive is designed to drive brush type DC motors at a high switching frequency. A single red/green LED indicates operating status. The drive is fully protected against over-voltage, under voltage, over-current, over-heating and short-circuits across motor, ground and power leads. Furthermore, the drive can interface with digital controllers or be used stand-alone and requires only a single unregulated DC power supply. Loop gain, current limit, input gain and offset can be adjusted using 14-turn potentiometers. The offset adjusting potentiometer can also be used as an on-board input signal for testing purposes.

Power Range

Peak Current	12 A
Continuous Current	6 A
Supply Voltage	20 - 80 VDC

Features

- Four Quadrant Regenerative Operation
- DIP Switch Selectable Modes
- Adjustable Current Limits
- High Switching Frequency
- Differential Input Command
- Digital Fault Output Monitor
- On-Board Test Potentiometer
- Offset Adjustment Potentiometer
- Adjustable Input Gain
- Drive Status LED
- Current Monitor Output
- Directional Inhibit Inputs for Limit Switches

MODES OF OPERATION
- Current
- Tachometer Velocity
- Voltage
- IR Compensation

COMMAND SOURCE
- ±10 V Analog

FEEDBACK SUPPORTED
- Tachometer

COMPLIANCES & AGENCY APPROVALS
- UL
- cUL
- CE Class A (LVD)
- CE Class A (EMC)
- RoHS

BLOCK DIAGRAM

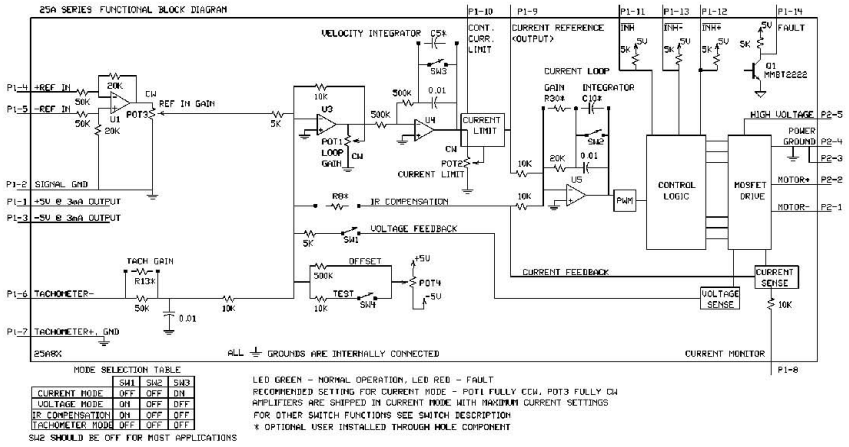

Information on Approvals and Compliances*	
c UL us	US and Canadian safety compliance with UL 508c, the industrial standard for power conversion electronics. UL registered under file number E140173. Note that machine components compliant with UL are considered UL registered as opposed to UL listed as would be the case for commercial products.
CE	Compliant with European CE for both the Class A EMC Directive 89/336/EEC on Electromagnetic Compatibility (specifically EN 61000-6-4:2001, EN 61000-6-2:2001, EN 61000-3-2:2000, and EN 61000-3-3:1995/A1:2001) and LVD requirements of directive 73/23/EEC (specifically EN 60204-1), a low voltage directive to protect users from electrical shock.
RoHS COMPLIANCE	RoHS (Reduction of Hazardous Substances) is intended to prevent hazardous substances such as lead from being manufactured in electrical and electronic equipment.

*Approvals may be pending. See "Compliances & Agency Approvals" on page 1 of datasheet for currently held approvals.

SPECIFICATIONS

Power Specifications		
Description	Units	Value
DC Supply Voltage Range	VDC	20 - 80
DC Bus Over Voltage Limit	VDC	86
Maximum Peak Output Current[1]	A	12
Maximum Continuous Output Current	A	6
Maximum Power Dissipation at Continuous Current	W	24
Minimum Load Inductance (Line-To-Line)[2]	µH	200
Switching Frequency	kHz	36
Control Specifications		
Description	Units	Value
Command Sources	-	±10 V Analog
Feedback Supported	-	Tachometer
Commutation Methods	-	External
Modes of Operation	-	Current, IR Compensation, Tachometer Velocity, Voltage
Motors Supported	-	Brushed, Voice Coil
Hardware Protection	-	Over Current, Over Temperature, Over Voltage, Short Circuit (Phase-Phase & Phase-Ground)
Mechanical Specifications		
Description	Units	Value
Agency Approvals	-	CE Class A (EMC), CE Class A (LVD), cUL, RoHS, UL
Size (H x W x D)	mm (in)	129.3 x 75.8 x 25.1 (5.1 x 3 x 1)
Weight	g (oz)	280 (9.9)
Heatsink (Base) Temperature Range[3]	°C (°F)	0 - 65 (32 - 149)
Storage Temperature Range	°C (°F)	-40 - 85 (-40 - 185)
Form Factor	-	Stand Alone
P1 Connector	-	16-pin, 2.54 mm spaced, friction lock header
P2 Connector	-	5-port, 5.08 mm spaced, screw terminal

Notes

1. Maximum duration of peak current is ~2 seconds.
2. Lower inductance is acceptable for bus voltages well below maximum. Use external inductance to meet requirements.
3. Additional cooling and/or heatsink may be required to achieve rated performance.

PIN FUNCTIONS

P1 - Signal Connector			
Pin	Name	Description / Notes	I/O
1	+5V 3mA OUT	±5 V @ 3 mA low power supply for customer use. Short circuit protected. Reference ground common with signal ground.	O
2	SIGNAL GND		GND
3	-5V 3mA OUT		O
4	+REF IN	Differential Reference Input (±10 V Operating Range, ±15 V Maximum Input)	I
5	-REF IN		I
6	-TACH IN	Negative Tachometer Input (Maximum ±60 V). Use signal ground for positive input.	I
7	+TACH / GND	Positive Tachometer Input and Signal Ground	GND
8	CURRENT MONITOR	Current Monitor. Analog output signal proportional to the actual current output. Scaling is 2.2 A/V. Measure relative to signal ground.	O
9	CURR REF OUT	Measures the command signal to the internal current-loop. This pin has a maximum output of ±7.25 V when the drive outputs maximum peak current. Measure relative to signal ground.	O
10	CONT CURRENT LIMIT	Can be used to reduce the factory-preset maximum continuous current limit without affecting the peak current limit by attaching an external current limiting resistor between this pin and signal ground. See pin details for resistor values.	I
11	$\overline{\text{INHIBIT IN}}$	TTL level (+5 V) inhibit/enable input. Leave open to enable drive. Pull to ground to inhibit drive. Inhibit turns off all power devices.	I
12	+INHIBIT IN	Positive Direction Inhibit (Does Not Cause A Fault Condition)	I
13	-INHIBIT IN	Negative Direction Inhibit (Does Not Cause A Fault Condition)	I
14	FAULT OUT	TTL level (+5 V) output becomes high when power devices are disabled due to at least one of the following conditions: inhibit, output short circuit, over voltage, over temperature, power-up reset.	O
15	NC	Not Connected (Reserved)	-
16	NC	Not Connected (Reserved)	-

P2 - Power Connector			
Pin	Name	Description / Notes	I/O
1	-MOT	Negative Motor Output	O
2	+MOT	Positive Motor Output	O
3	POWER GND	Power Ground (Common With Signal Ground)	GND
4	POWER GND		GND
5	HIGH VOLTAGE	DC Power Input	I

Pin Details

CONT CURRENT LIMIT (P1-10)

This pin can be used to reduce the continuous current limit without affecting the peak current limit by connecting an external current limiting resistor between this pin and signal ground. See table below.

Current Limit Resistor	15 kΩ	6.6 kΩ	3.4 kΩ	2.1 kΩ	1.2 kΩ	810Ω	500 Ω	250 Ω	0 kΩ
Continuous Current Limit	90%	80%	70%	60%	50%	40%	30%	20%	10%

Note: These values are secondary to the continuous/peak ratio set by the DIP switches.

HARDWARE SETTINGS

Switch Functions

Switch	Description	Setting	
		On	Off
1	Voltage feedback. Mode dependent (see mode selection table below).	On	Off
2	Current loop integral gain. Activates or deactivates integration. OFF by default.	Inactive	Active
3	Outer loop integration. Activates or deactivates integration. ON, by default, for current mode and OFF for other modes.	Inactive	Active
4	Test/Offset. Switches the function of the Test/Offset pot between an on-board command input for testing or a command offset adjustment. OFF by default.	Test	Offset

Mode Selection Table

	SW1	SW3
CURRENT	OFF	ON
VOLTAGE	ON	OFF
IR COMPENSATION	ON	OFF
TACHOMETER VELOCITY	OFF	OFF

Potentiometer Functions

Potentiometer	Description	Turning CW
1	Loop gain adjustment for voltage/velocity modes. Turn this pot fully CCW in current mode.	Increases gain
2	Current limit. It adjusts both continuous and peak current limit while maintaining their ratio.	Increases limit
3	Reference gain. Adjusts the ratio between input signal and output variables (voltage, current, or velocity).	Increases gain
4	Offset / Test. Used to adjust any imbalance in the input signal or in the amplifier. Can also be used as an on-board signal source for testing purposes.	Adjusts offset in negative direction

Note: Potentiometers are approximately linear and have 12 active turns with 1 inactive turn on each end.

Through-hole Components†

Location	Description
C10*	Current Loop Integrator. Through-hole capacitor that can be added for more precise current loop tuning. See section below on Tuning with Through-hole components for more details.
C5*	Velocity Loop Integrator. Through-hole capacitor that can be added for more precise velocity loop tuning. See section below on Tuning with Through-hole components for more details.
R13*	Tachometer Input Scaling. Through-hole resistor that can be added to change the gain of the tachometer input. See section below on Tachometer Gain for more details.
R30*	Current Loop Proportional Gain. Through-hole resistor that can be added for more precise current loop tuning. See section below on Tuning with Through-hole components for more details.
R8*	IR Compensation Scaling. Through-hole resistor that must be added to configure the amplifier for IR Compensation mode. See section below on IR Compensation Notes for more details.

Tachometer Gain

Some applications may require an increase in the gain of the tachometer input signal. This occurrence will be most common in designs where the tachometer input has a low voltage to RPM scaling ratio. The drive offers a through-hole location listed in the above table where a resistor can be added to increase the tachometer gain. Use the drive's block diagram to determine an appropriate resistor value.

Tuning With Through-hole Components

In general, the drive will not need to be further tuned with through-hole components. However, for applications requiring more precise tuning than what is offered by the potentiometers and dipswitches, the drive can be manually modified with through-hole resistors and capacitors as denoted in the above table. By default, the through-hole locations are not populated when the drive is shipped. Before attempting to add through-hole components to the board, consult the section on loop tuning in the installation notes on the manufacturer's website. Some general rules of thumb to follow when adding through-hole components are:

- A larger resistor value will increase the proportional gain, and therefore create a faster response time.
- A larger capacitor value will increase the integration time, and therefore create a slower response time.

Proper tuning using the through-hole components will require careful observation of the loop response on a digital oscilloscope to find the optimal through-hole component values for the specific application.

IR Compensation Notes

For applications that will use IR Compensation mode, a resistor must be added to the location named in the table above. The combination of the added resistor and correct dipswitch settings will configure the amplifier for IR Compensation mode. While in IR Compensation mode, the amplifier will adjust the duty cycle to compensate for changes in the output current. Consult the amplifier's functional block diagram and the manufacturer's website for more information.

[†]**Note: Damage done to the drive while performing these modifications will void the warranty.**

MECHANICAL INFORMATION

P1 - Signal Connector		
Connector Information		16-pin, 2.54 mm spaced, friction lock header
Mating Connector	Details	Molex: P/N 22-01-3167 (connector) and P/N 08-50-0114 (insert terminals)
	Included with Drive	Yes

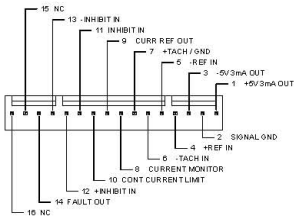

P2 - Power Connector		
Connector Information		5-port, 5.08 mm spaced, screw terminal
Mating Connector	Details	Not applicable
	Included with Drive	Not applicable

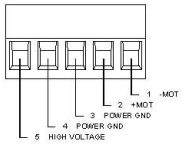

MOUNTING DIMENSIONS

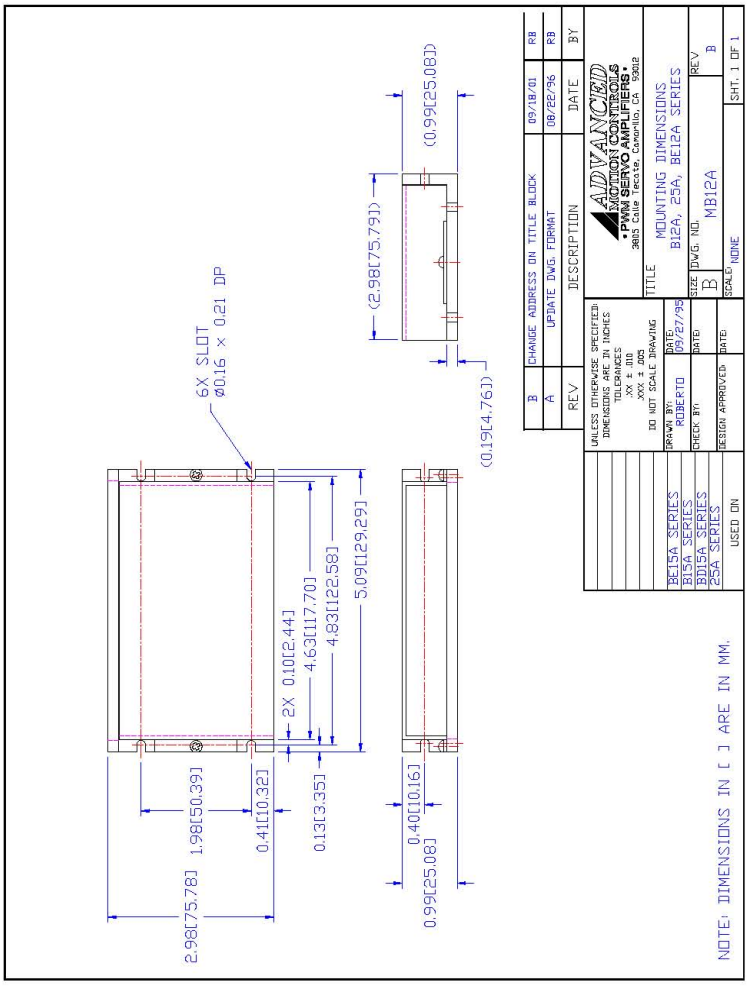

ADVANCED MOTION CONTROLS Analog Servo Drive **12A8**

PART NUMBERING INFORMATION

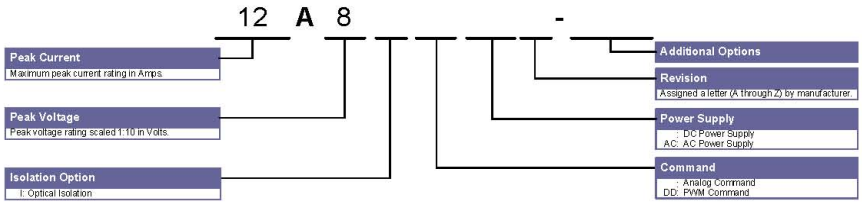

All analog servo drive models listed in the selection tables of the website are readily available, standard product offerings. However, additional features and/or options are available for select drives and other possibilities can be made available for OEMs with sufficient volume requests. Feel free to contact Applications Engineering for further information and details.

Sold by Servo Systems Co.
115 Main Road, P.O. Box 97
Montville, NJ 07045-0097
Toll Free: (800) 922-1103
Phone: (973) 335-1007
Fax: (973) 335-1661
www.servosystems.com

PS2X300W and PS4X300W SERIES POWER SUPPLIES

FEATURES:

- Multiple primary windings: either 120 VAC or 240 VAC, 50/60 Hz operation
- 24 VDC secondary output winding taps
- Low cost
- Agency approvals:

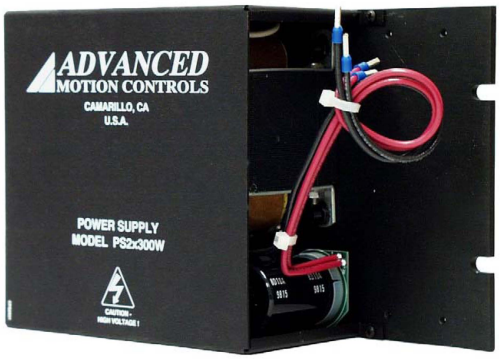

BLOCK DIAGRAM:

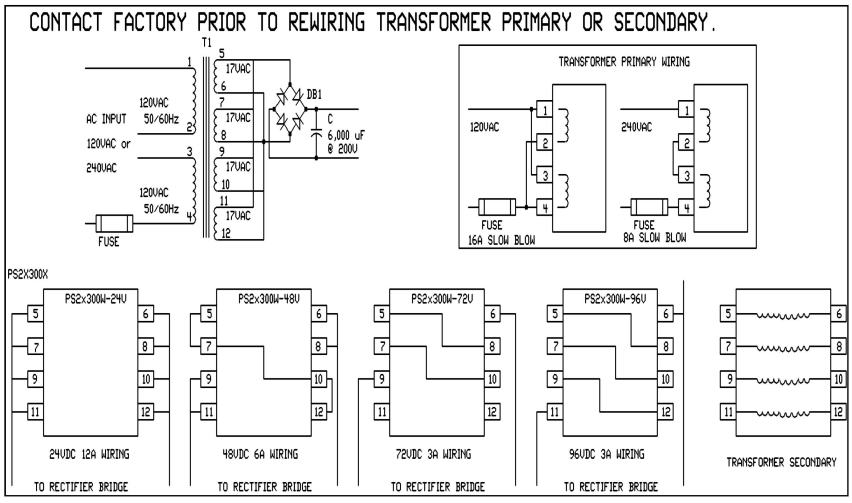

Power Supplies, Filter Cards & Shunt Regulators

DESCRIPTION: The PS2X300W and PS4X300W series unregulated power supplies have been designed to complement *ADVANCED* **MOTION CONTROLS'** servo amplifiers and to provide the user with a complete solution to single and multi-axes DC drive applications. These unregulated DC power sources are an acceptable solution for most applications as *ADVANCED* **MOTION CONTROLS'** servo amplifiers compensate for power supply output variations and AC ripple components. Series PS2X300W power supplies are designed to provide the best cost-per-watt value while mechanically hosting two of B15A, BE15A or 25A Series servo amplifiers. The PS4X300W power supplies are identical to the PS2X300W power supplies except they have an extended mounting plate to accommodate two additional drives. Both series have multiple primary windings for 120VAC and 240 VAC 50/60 Hz operation. These power supplies feature four identical secondary windings that can be connected in series or in parallel for different output voltages and currents.

	MODEL
MECHANICAL SPECIFICATIONS	**PS2X300W and PS4X300W**
AC INPUT CONNECTOR (female three prong plug)	AC cord (not supplied)
DC OUTPUT CONNECTOR	Flying Leads
SIZE	9.00 x 5.75 x 3.47 inches 228.6 x 146.1 x 88.1 mm
WEIGHT	9 lb. 4.1 Kg.

ORDERING INFORMATION:

AMC PART NUMBER			
Input Voltage (240VAC)	**Input voltage (120VAC)**	**Output Voltage (VDC)**	**Nominal Output Current (Amps)**
PS2X3H24	PS2X3W24	24	12
PS2X3H48	PS2X3W48	48	6
PS2X3H72	PS2X3W72	72	3
PS2X3H96	PS2X3W96	96	3

Designate PS4X... instead of PS2X... to order the PS4X300W series. Electrical ratings are identical.

MOUNTING DIMENSIONS:

PS2X300W

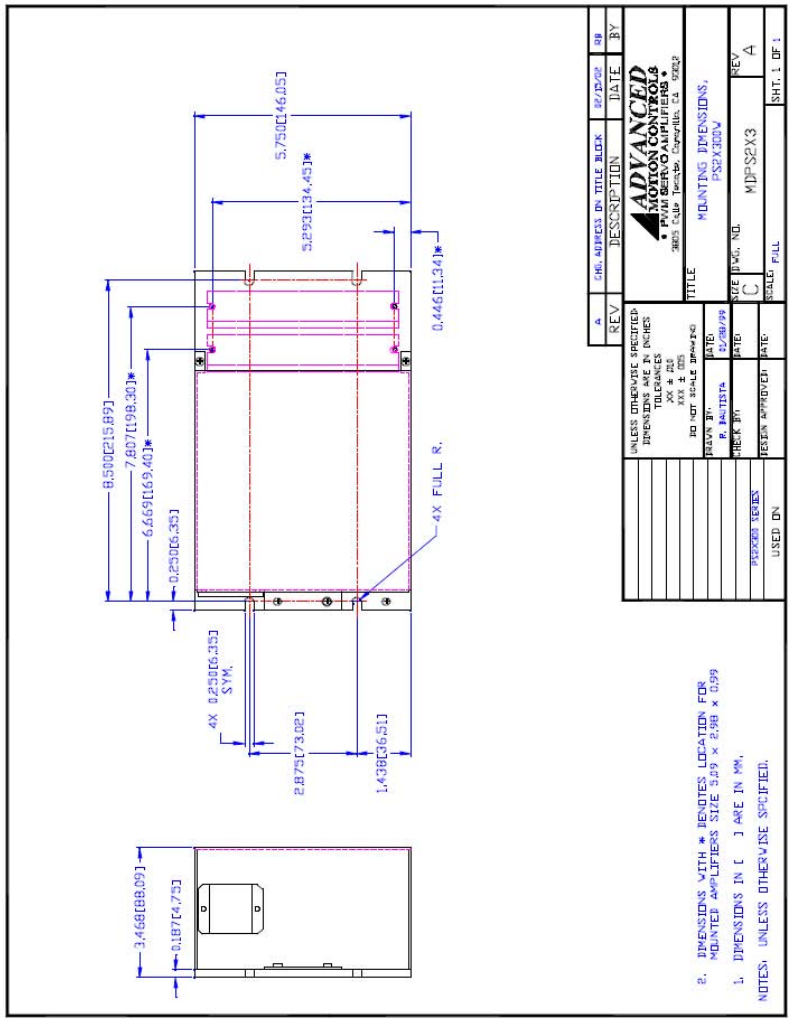

Power Supplies, Filter Cards & Shunt Regulators

MOUNTING DIMENSIONS:

PS4X300W

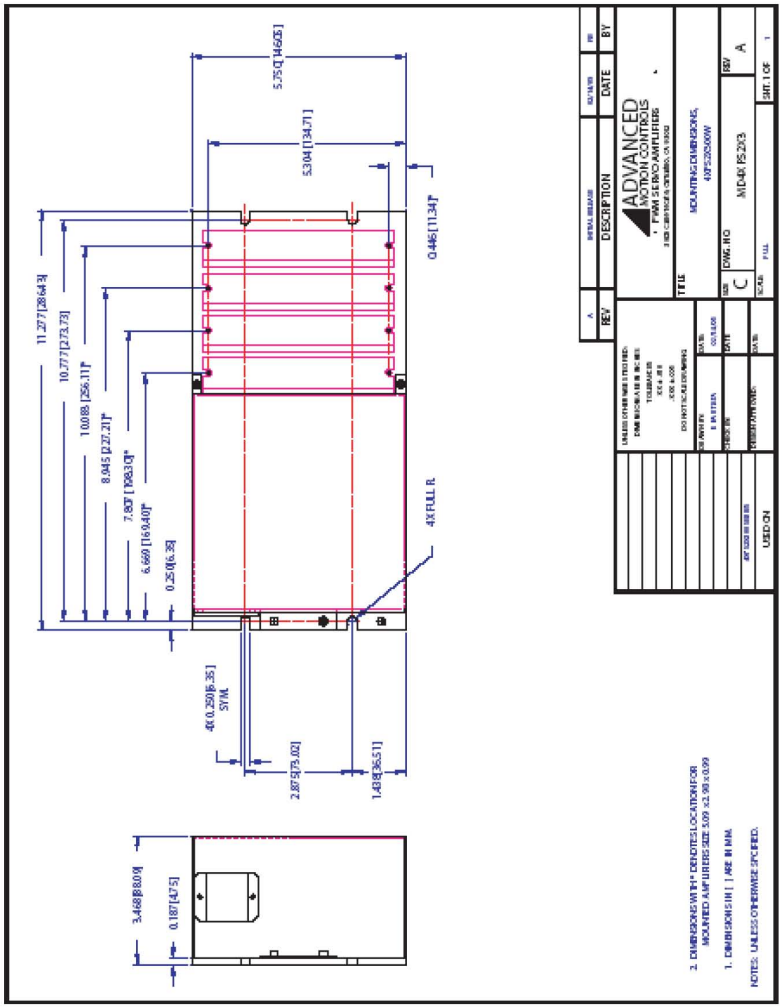

Encoder HEDS 5540, 500 Counts per turn, 3 Channels

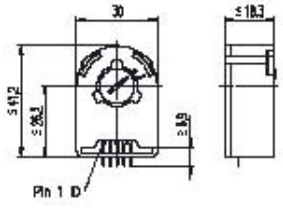

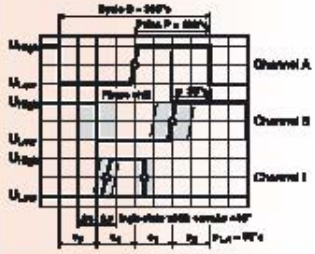

Stock program
Standard program
Special program (on request)

Order Number	110511	110513	110515
Type			
Counts per turn	500	500	500
Number of channels	3	3	3
Max. operating frequency (kHz)	100	100	100
Shaft diameter (mm)	3	4	6

Combination

+ Motor	Page	+ Gearhead	Page	+ Brake	Page	Overall length [mm] / ● acc: + Gearhead		
F 2260, 40 W	95						111.9	
F 2260, 40 W	95	GP 62, 30 - 50 Nm	229				↓	
F 2260, 80 W	96						147.4	
F 2260, 80 W	96	GP 62, 30 - 50 Nm	229				↓	
A-max 26	114-120					63.5		
A-max 26	114-120	GP 26, 05 - 2.0 Nm	216			↓		
A-max 26	114-120	GS 30, 007 - 0.2 Nm	217			↓		
A-max 26	114-120	GP 32, 075 - 6.0 Nm	218/221			↓		
A-max 26	114-120	GP 32, 04 - 2.0 Nm	222			↓		
A-max 26	114-120	GS 38, 01 - 0.6 Nm	223			↓		
A-max 32	122/124						82.3	
A-max 32	122/124	GP 32, 075 - 6.0 Nm	218/221				↓	
A-max 32	122/124	GS 38, 01 - 0.6 Nm	223				↓	
EC 32, 80 W	159						78.4	
EC 32, 80 W	159	GP 32, 075 - 6.0 Nm	218/221				↓	
EC 40, 120 W	160							88.4
EC 40, 120 W	160	GP 42, 30 - 15 Nm	224					↓
EC 40, 120 W	160	GP 52, 40 - 30 Nm	227					↓

Technical Data

Supply voltage	5 V ± 10 %
Output signal	TTL compatible
Phase shift Φ (nominal)	90°
Logic state width s	min. 45°
Signal rise time (typical at C_L = 25 pF, R_L = 2.7 kΩ, 25°C)	180 ns
Signal fall time (typical at C_L = 25 pF, R_L = 2.7 kΩ, 25°C)	40 ns
Index pulse width (nominal)	90°
Operating temperature range	-40 ... +100°C
Moment of inertia of code wheel	≈ 0.6 gcm²
Max. angular acceleration	250 000 rad s⁻²
Output current per channel	min. -1 mA, max. 5 mA

Pin Allocation

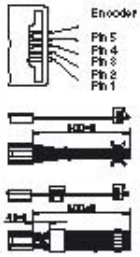

Encoder	Designation	Pin no. from 9409.506
Pin 5	Channel B	1
Pin 4	V_{cc}	2
Pin 3	Channel A	3
Pin 2	Channel I	4
Pin 1	GND	5

Cable with plug:
maxon Art. No. 9409.506
The plug (Harting 09 18 006 03 03) can be fixed in the required position.

Cable with plug: (compatible with Encoder HEDS 5700)
maxon Art. No. 9409.504
The plug (SM 09 11 00 10 01) can be fixed in the required position.

Connection example

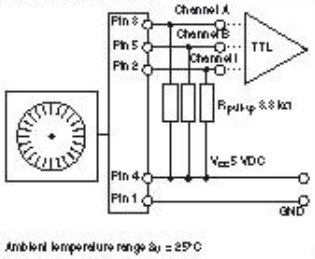

Ambient temperature range ϑ_U = 25°C

SE3455/5455

GaAs Infrared Emitting Diode

FEATURES

- TO-46 metal can package
- Choice of flat window or lensed package
- 90° or 20° (nominal) beam angle option
- 935 nm wavelength
- Wide operating temperature range (- 55°C to +125°C)
- Ideal for high pulsed current applications
- Mechanically and spectrally matched to SD3421/5421 photodiode, SD3443/5443/5491phototransistor, SD3410/5410 photodarlington and SD5600 series Schmitt trigger

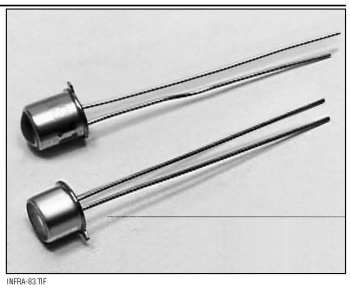

INFRA-83.TIF

DESCRIPTION

The SE3455/5455 series consists of a gallium arsenide infrared emitting diode mounted in a TO-46 metal can package. The SE3455 series has flat window cans providing a wide beam angle, while the SE5455 series has glass lensed cans providing a narrow beam angle. These devices are constructed with dual bond wires suitable for pulsed current applications. The TO-46 packages offer high power dissipation capability and are ideally suited for operation in hostile environments.

OUTLINE DIMENSIONS in inches (mm)

Tolerance	3 plc decimals	±0.005(0.12)
	2 plc decimals	±0.020(0.51)

SE3455

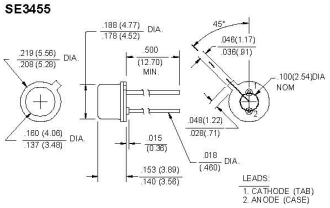

DIM_005a.ds4

SE5455

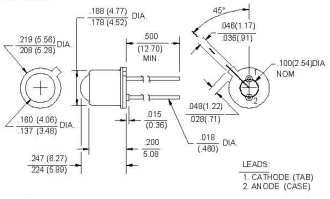

DIM_005b.ds4

Honeywell

SE3455/5455

GaAs Infrared Emitting Diode

ELECTRICAL CHARACTERISTICS (25°C unless otherwise noted)

PARAMETER	SYMBOL	MIN	TYP	MAX	UNITS	TEST CONDITIONS
Total Power Output	P_O				mW	I_F=100 mA
SE3455-001, SE5455-001		2.0				
SE3455-002, SE5455-002		3.5				
SE3455-003, SE5455-003		4.8				
SE3455-004, SE5455-004		5.4				
Forward Voltage	V_F			1.7	V	I_F=100 mA
Reverse Breakdown Voltage	V_{BR}	3.0			V	I_R=10 µA
Peak Output Wavelength	λ_P		935		nm	
Spectral Bandwidth	$\Delta\lambda$		50		nm	
Spectral Shift With Temperature	$\Delta\lambda_P/\Delta_T$		0.3		nm/°C	
Beam Angle (1)	Ø				degr.	I_F=Constant
SE3455			90			
SE5455			20			
Radiation Rise And Fall Time	t_r, t_f		0.7		µs	

Notes
1. Beam angle is defined as the total included angle between the half intensity points.

ABSOLUTE MAXIMUM RATINGS

(25°C Free-Air Temperature unless otherwise noted)

Continuous Forward Current	100 mA
Peak Forward Current (1µs pulse width, 300 pps)	3 A
Power Dissipation	150 mW (1)
Operating Temperature Range	-55°C to 125°C
Storage Temperature Range	-65°C to 150°C
Soldering Temperature (10 sec)	260°C

Notes
1. Derate linearly from 25°C free-air temperature at the rate of 1.43 mW/°C.

SCHEMATIC

Honeywell

SE3455/5455

GaAs Infrared Emitting Diode

Fig. 1 Radiant Intensity vs Angular Displacement (SE3455)

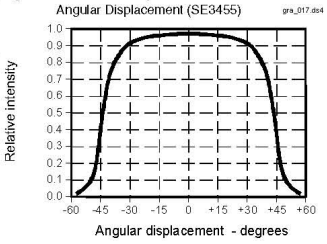

Fig. 2 Radiant Intensity vs Angular Displacement (SE5455)

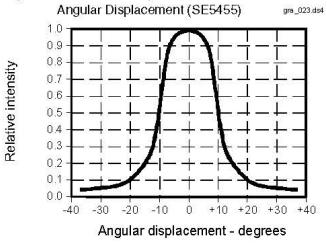

Fig. 3 Radiant Intensity vs Forward Current

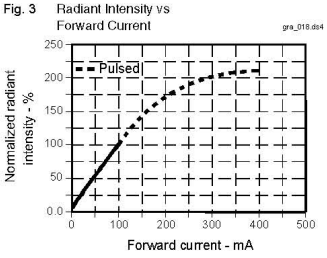

Fig. 4 Forward Voltage vs Forward Current

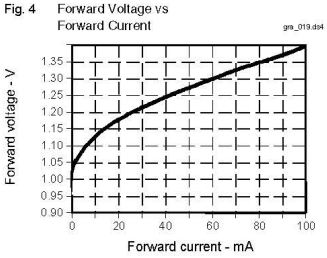

Fig. 5 Forward Voltage vs Temperature

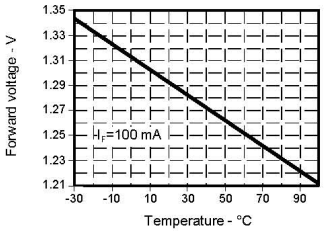

Fig. 6 Spectral Bandwidth

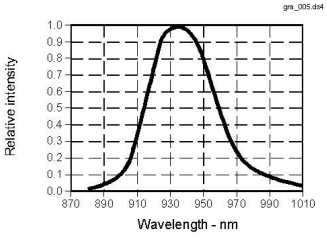

Honeywell

SE3455/5455

GaAs Infrared Emitting Diode

Fig. 7 Coupling Characteristics
SE3455 with SD3443

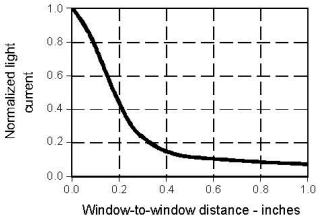

Fig. 8 Coupling Characteristics
SE5455 with SD5443

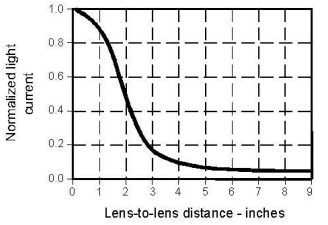

Fig. 9 Radiant Intensity vs
Case Temperature

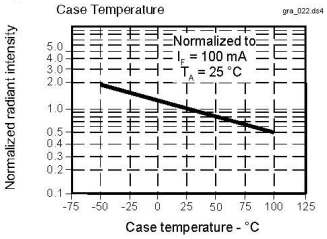

All Performance Curves Show Typical Values

Datasheet -- SD5600-001

⚠ WARNING

MISUSE OF DOCUMENTATION

- The information presented in this product sheet (or catalog) is for reference only. DO NOT USE this document as product installation information.
- Complete installation, operation and maintenance information is provided in the instructions supplied with each product.

Failure to comply with these instructions could result in death or serious injury.

Honeywell

Representative photograph, actual product appearance may vary.

Due to regional agency approval requirements, some products may not be available in your area. Please contact your regional Honeywell office regarding your product of choice.

SD5600-001

SD Series Optoschmitt Detector, TO-46 Metal Can Package

Features

- TO-46 metal can package
- 6 ° (nominal) acceptance angle
- High noise immunity output
- TTL/LSTTL/CMOS compatible
- Buffer (SD5600) or inverting (SD5610) logic available
- Mechanically and spectrally matched to SE3450/5450, SE3455/5455 and SE3470/5470 infrared emitting diodes

Description

The SD5600/5610 series is a family of single chip Optoschmitt IC detectors mounted in a TO-46 metal can package. The photodetector consists of a photodiode, amplifier, voltage regulator, Schmitt trigger and an NPN output transistor with 10 kOhm (nominal) pull-up resistor. Output rise and fall times are independent of the rate of change of incident light. Detector sensitivity has been internally temperature compensated. The TO-46 package is ideally suited for operating in hostile environments.

Device Polarity:

Buffer - Output is HI when incident light intensity is above the turn-on threshold level.

Inverter - Output is LO when incident light intensity is above the turn-on threshold level.

Honeywell

SD5600-001

SD Series Optoschmitt Detector, TO-46 Metal Can Package

Product Specifications	
Product Type	IR Component
Angular Response (Degree)	12
Turn-on Threshold Irradiance	2.5 mW/cm² maximum
Output	10 kOhm Pull-up
Output Logic	Buffer
Package Style	T0-46, Dome Lensed
Package Components	Metal
Operating Temperature Range	-40 °C to 100 °C [-40 °F to 212 °F]
Dark Current	250 nA
Hysteresis (H)	5% to 30%
Operating Supply Voltage	4.5 V to 16.0 V
Supply Voltage	16.0 Vdc
High Level Output Voltage	2.4 V minimum
Low Level Output Voltage	0.4 V maximum
Operating Point Temperature Coeffient	-0.76 %/°C
Internal Pull-up Resistor	5.0 kOhm min., 10.0 kOhm typ., 20.0 kOhm max.
Output Rise Time	60 ns
Output Fall Time	15 ns
Clock Frequency	100 kHz
Duration of Output Short Vcc or Ground	1.0 second
Comment	Output is HI when incident light intensity is above the turn-on threshold level.
Availability	Global
Product Name	Optoschmitt Detector
Supply Current max.	12.0 - 15.0 mA @ 25 °C
Output Current max.	18 mA

Honeywell

SD5600-001

SD Series Optoschmitt Detector, TO-46 Metal Can Package

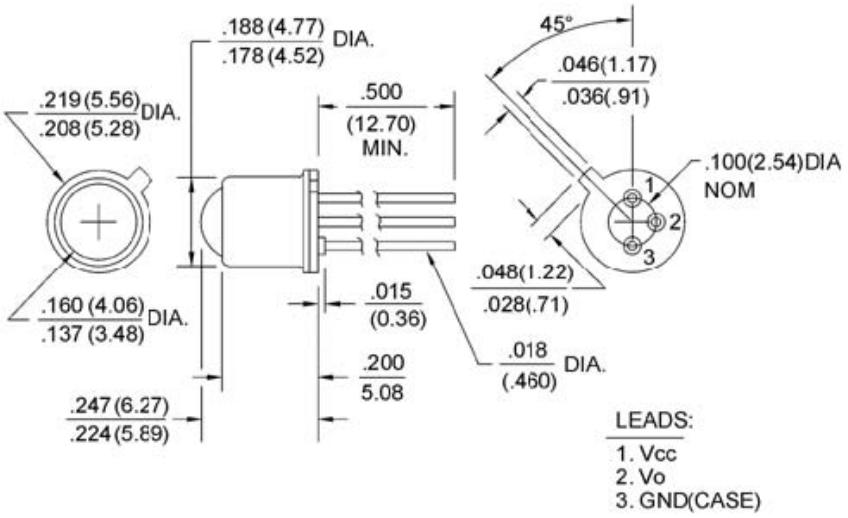

Honeywell

SD5600-001

SD Series Optoschmitt Detector, TO-46 Metal Can Package

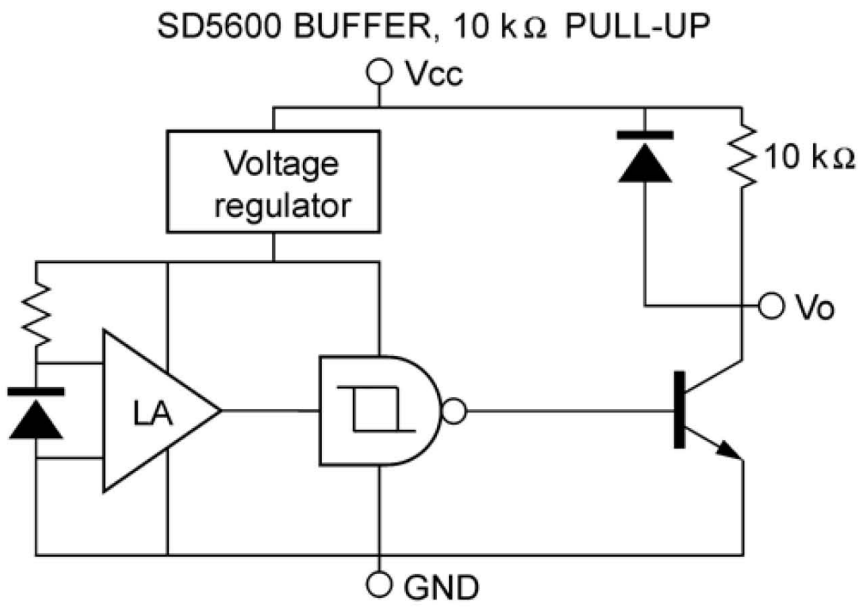

Honeywell

SD5600-001

SD Series Optoschmitt Detector, TO-46 Metal Can Package

⚠ WARNING
PERSONAL INJURY
DO NOT USE these products as safety or emergency stop devices, or in any other application where failure of the product could result in personal injury.

Failure to comply with these instructions could result in death or serious injury.

Bibliography

[1] Blumenthal Clinic, [Online] Available: http://www.blumenthalclinic.com.au/ [Accessed: July 9, 2010]

[2] World Wide Information Center for Minimally Invasive Robotic Surgery, [Online] Available: http://avrasurgical.com/surgicalrobots.html [Accessed: July 10, 2010]

[3] Curexo Technology Corporation, [Online] Available: http://www.robodoc.com/, [Accessed: July 10, 2010]

[4] Intuitive Surgerical Inc., [Online] Available: http://www.intuitivesurgical.com/index.aspx, [Accessed: July 10, 2010]

[5] MAKO Surgical Corp., [Online] Available: http://www.makosurgical.com/, [Accessed: July 10, 2010]

[6] Virtual surgical training environment, [Online] Available: http://www.cuhk.edu.hk/ipro/pressrelease/040209e.htm, [Accessed: July 15, 2010]

[7] SensAble Technologies Inc, "Specifications for PHANTOM Premium 3.0/6 DOF Haptic Interface," Jan. 6, 2006. [Online] Available: http://www.sensable.com/haptic-phantom-premium-6dof.htm [Accessed: Jan. 26, 2010]

[8] MPB Technologies Inc, [Online] Available: http://www.mpb-technologies.ca/ [Accessed: Jan. 26, 2010]

[9] Haption, [Online] Available: http://www.haption.com/site/eng/html/materiel.php [Accessed: Feburary.7, 2010]

[10] Force Dimension, [Online] Available: http://www.forcedimension.com/products [Accessed: Jan. 26, 2010]

[11] S. S. Lee, J. M. Lee, "Design of a general purpose 6-DOF haptic interface," Mechatronics, vol. 13, pp: 697-722, 2003

[12] G. Carbone, M. Ceccarelli, "A serial-parallel robotic architecture for surgical tasks," Robotica, vol. 23, pp: 345-354, 2005

[13] T. Li, "The Design and Development of Robotic Mechanisms for Laparoscopic Surgery," Ph.D. thesis, Experimental Robotics Laboratory, School of Engineering Science, Simon Fraser University, Burnaby, BC, Dec. 2005

[14] T. Li and S. Payandeh, "Toward New Designs of Haptic Devices for Minimally Invasive Surgery," Computer Assisted Radiology and Surgery, pp. 775-781, 2003

[15] T. Li, and S. Payandeh, "Design of Spherical Parallel Mechanisms for Application to Laparoscopic Surgery," Robotica, pp. 133-138, 2002

[16] J. Hsu, "Toward Integration of a Surgical Robotic System with Automatic Tracking, Tool Gesture and Motion Recognition," M.A.Sc. thesis, Experimental Robotics Laboratory, School of Engineering Science, Simon Fraser University, Burnaby, BC, Dec. 2006

[17] A. Ma, "Toward Integration of a Surgical Robotic Simulator with a 4-DOF Haptic Device," M.A.Sc. thesis, Experimental Robotics Laboratory, School of Engineering Science, Simon Fraser University, Burnaby, BC, 2008

[18] S. Payandeh, J. Dill, J. Zhang, "On Application of Haptic Feedback as an Aid in the Design of Passive Mechanisms," International Journal of Computer Aided Design, Vol. 39, No. 6, pp. 528 - 538, 2007

[19] J. Zhang, S. Payandeh, J. Dill, "Haptic Aided Design: a Case Study," Proceedings of the 11th Symposium on Haptic Interfaces for Virtual Environment and Teleoperator Systems, March 2003, pp. 254 - 261

[20] P. Rizun, D. Gunn, B. Cox, G. Sutherland, "Mechatronic design of haptic forceps for robotic surgery," The International Journal of Medical Robotics and Computer Assisted Surgery Volume 2, Issue 4, December 2006, pp. 341-349

[21] T.K. Tanev, "Kinematics of a hybrid (parallel-serial) robot manipulator", Mechanism and Machine Theory 35(2000): 1183-1196

[22] L. Romdhane, "Design and analysis of a hybrid seria-parallel manipulator", Mechanism and Machine Theory 34(1999): 1037-1055

[23] X.Z. Zheng, H.Z. Bin, Y.G. Luo, "Kinematic analysis of a hybrid serial-parallel manipulator," International Journal on Advanced Manufacturing Technology 23(2004): 925-930

[24] G. Yang, I. Chen, S.H. Yeo, W. L, "Design and Analysis of a Modular Hybrid Parallel-Serial Manipulator for Robotised Deburring Applications", Smart Devices and Machines for Advanced Manufacturing, London: Springer, 2008

[25] M. Ceccarelli, E. Ottaviano, G. Carbone, "A Study of Feasibility for a Novel Parallel-serial Manipulator", Journal of Robotics and Mechatronics 14(2002): 304-312

[26] C.M. Gosselin and M. Gagne, "A Closed-Form Solution for the Direct Kinematics of a Special Class of Spherical Three-Degree-Of-Freedom Parallel Manipulators." Computational Kinematics, 1995, pages 231 - 240

[27] W. M. Craver, "structural analysis and design of three-degree-of-freedom robotic should module," master thesis, the University of Texas at Austin, 1989

[28] Shaoping Bai, Michael R. Hansen and Torben O. Andersen, "Modeling of a special class of spherical parallel manipulators with Euler parameters," Robotica, pages 1-10

[29] X. Kong, C. Gosselin, "Forward Displacement Analysis of a Quadratic Spherical Parallel Manipulator: The Agile Eye," Proceedings of the ASME 2009 International Design Engineering Technical Conferences & Computers and Information in Engineering Conference, Paper DETC2009-87467, August 30-September 2, 2009, San Diego, California, USA

[30] John J. Craig, Introduction to robotics mechanics and control, 3rd ed. Upper Saddle River, NJ: Pearson Prentice Hall, 2005

[31] A. Ma, S. Payandeh "Analysis and Experimentation of a 4-DOF Haptic Device." Proceedings of IEEE Haptics Symposium, Reno, Nevada, USA, pp. 351 - 356, March 2008

[32] I.A. Bonev, D. Chablat, P. Wenger, "Working and assembly modes of the agile eye," IEEE International Conference on Robotics and Automation, 2006, pp. 2317 - 2322

[33] L. Birglen and C.M. Gosselin, "SHaDe, A New 3-DOF Haptic Device," IEEE Transactions on Robotics and Automation, vol. 18, no. 2, 2002

[34] I.A. Bonev, D. Chablat, P. Wenger, "Working and assembly modes of the agile eye," IEEE International Conference on Robotics and Automation, 2006, pp. 23172322

[35] N. Diolaiti, G. Niemeyer, F. Barbagli, J. Kenneth Salisbury, Jr, "Stability of Haptic Rendering: Discretization, Quantization, Time Delay, and Coulomb Effects," IEEE Transactions on Robotics, vol. 22, no. 2, 2006

[36] H.F. Shi, S. Payandeh, "On Suturing Simulation with Haptic Feedback," EuroHaptics 2008, pp. 599 - 608, Madrid, Spain, 2008

[37] P. Lacroute, M. Levoy, "Fast Volume Rendering Using a Shear-Warp Factorization of the Viewing Transformation," Computer Graphics Proceedings, Annual Conference Series, Orlando, Florida, Jul. 24 - 29, 1994

[38] C. Basdogan, C. Ho, M.A. Srinivasan, "A Ray-Based Haptic Rendering Technique for Displaying Shape and Texture of 3D Objects in Virtual Environments," Vol. 61, Proceedings of the ASME Dynamic Systems and Control Division, 1997

[39] M. Pauly, L.P. Kobbelt, M. Gross, "Point-Based Multiscale Surface Representation," ACM Transactions on Graphics, Vol. 25, No. 2, April 2006, pp. 177 - 193

[40] R. J. Adams, B. Hannaford, "Stable Haptic Interaction with Virtual Environments," IEEE Transactions on Robotics and Automation, vol. 15, no. 3, 1999

[41] B. Hannaford, J. Ryu, "Time-Domain Passivity Control of Haptic Interfaces," IEEE Transactions on Robotics and Automation, vol. 18, no. 1, 2002

[42] P.E. Wellstead, Introduction to Physical System Modeling, UK: Control Systems Principles, 2000

[43] P.C. Sen, Principles of Electric Machines and Power Electronics, 2nd edition. New York: John-Wiley & Sons, Inc., 1997.

[44] N.L. Bernstein, D.A. Lawrence, L.Y. Pao, "Friction Modeling and Compensation for Haptic Interfaces," Proceedings of the First Joint Eurohaptics Conference and Symposium on Haptic Interfaces for Virtual Environment and Teleoperator Systems, Pisa, Italy, pp. 290 - 295, March 2005

[45] V. Hayward, B. Armstrong, "A New Computational Model of Friction Applied to Haptic Rendering," Experimental Robotics VI, Springer: New-York, LNCS 250, 2000, pp. 404 - 412

[46] M. Mahvash, A.M. Okamura, "Friction Compensation for a Force-Feedback Telerobotic System," Proceedings of the 2006 IEEE International Conference on Robotics and Automation, Orlando, Florida, pp. 3268 - 3273, May 2006

[47] C. Richard, M.R. Cutkosky, "Friction modeling and display in haptic applications involving user performance," Proceedings of the 2002 IEEE International Conference on Robotics and Automation, Washington,DC, pp. 605 - 611, May 2002

[48] B. Taati, A.M. Tahmasebi, K. Hashtrudi-Zaad, "Experimental Identification and Analysis of the Dynamics of a PHANToM Premimum 1.5A Haptic Device," Presence, Vol. 17, No. 4, August 2008, pp. 327 - 343

[49] W. Shang, S. Cong, F. Kong, "Identification of dynamic and friction parameters of a parallel manipulator with actuation redundancy," Mechatronics, vol. 20, 2010, pp. 192 - 200

[50] J.E. Colgate, M.C. Stanley, and J.M. Brown, "Issues in the haptic display of tool use," in Proc. IEEE/RSJ Int. Conf. on Intelligent Robotics and Systems, Pittsburgh, PA, 1995, pp. 140 - 145

[51] C.B. Zilles and J.K. Salisbury, "A constraint-based god-object method for haptic display," in Proc. IEEE/RSJ Int. Conf. on Intelligent Robotics and Systems, Pittsburgh, PA, 1995, pp.146 -151

[52] J.E. Colgate, P. Grafing, M. Stanley, and G. Schenkel, "Implementation of stiff virtual walls in force-reflecting interfaces," in IEEE Virtual Reality Symposium, 1993, pp. 202 - 208

[53] J.E. Colgate and G. Schenkel, "Passivity of a class of sampled-data systems: Application to haptic interfaces," in American Control Conference, Baltimore, Maryland, June 1994, pp. 3236 - 3240

[54] B. Gillespie and M. Cutkosky, "Stable user-specific rendering of the virtual wall," in ASME IMECE, vol. DSC-Vol. 58, Atlanta, GA, November 1996, pp. 397 - 406

[55] N. Hogan, "Controlling impedance at the man/machine interface," in Proceedings IEEE International Conference on Robotics and Automation, 1989, pp. 1626 - 1631

[56] J. Willems, "Dissipative dynamical systems, part i: General theory," Arch. Rat. Mech. An., vol. 45, 1972.

[57] S. Stramigioli, C. Secchi, A. van der Schaft, and C. Fantuzzi, "A novel theory for sample data system passivity," in Proceedings of the IEEE/RSJ International Conference on Intelligent Robots and Systems, Lausanne, Switzerland, October 2002

[58] B.E. Miller, J.E. Colgate, R.A. Freeman, "Passive Implementation for a Class of Static Nonlinear Environments in Haptic Display," Proceedings of the IEEE International Conference on Robotics & Automation, Detroit, Michigan, USA, May 1999

[59] R. Ellis, N. Sarkar, and M. Jenkins, "Numerical methods for the force reflection of contact," ASME Journal of Dynamic Systems, Measurement and Control, vol. 119, pp. 768 - 774, 1997

[60] William J. Terrell, Stability and stablization: an introduction, Princeton, NJ. : Princeton University Press, 2009

[61] A. van der Schaft, L2-Gain and Passivity Techniques in Nonlinear Control, ser. Communication and Control Engineering. Springer Verlag, 2000

[62] Virtual Training Environment, [Online] Available http://www2.ensc.sfu.ca/research/erl/ViTEn1/index.php [Accessed: August 10, 2010]